CENTRO DE INVESTIGACIONES EN ÓPTICA, A.C.

Design, Fabrication and Investigation of Special Microstructured Fibers

Doctorado en Ciencias (Óptica)

Asesor: Dr. Uladzímir Petróvich Minkovich

Estudiante: Marcelo Vaca Pereira Ghirghi

Versión definitiva. Incluye cambios requeridos por revisores

Agosto de 2016

León, Guanajuato, México

Design, Fabrication and Investigation of Special Microstructured Fibers

By

Marcelo Vaca Pereira Ghirghi

Approved by:

Dr. Yuri Barmenkov
Examiner

Dr. Evgeny Myslivets
Examiner

Dr. Uladzímir Petróvich Minkóvich
Examiner

Centro de Investigaciones en Óptica, A.C.
August, 2016

"The ideals that have lighted my way, and time after time have given me new courage to face life cheerfully, have been Kindness, Beauty, and Truth. Without the sense of kinship with men of like mind, without the occupation with the objective world, the eternally unattainable in the field of art and scientific endeavors, life would have seemed empty to me. The trite objects of human efforts possessions, outward success, luxury have always seemed to me contemptible.".

Albert Einstein

Introduction

Optical fibers, which are used basically in telecommunication systems [1], are fabricated from a thin glass thread that is slightly thicker than a human hair; they are used for the transmission of light from one place to another, similar to a copper conductor conducting electrical signals or power [2]. Optical fibers also play an important role in systems of industrial lasers, medical devices and in different sensory equipment.

Conventional optical fibers for telecommunications are typically made of two layers of glass or silica: an inner core, doped with small amounts of other material (generally germanium), and an outer cladding, made of pure silica. The refractive index difference between the core and the cladding makes that the light entering at one end of the fiber be reflected at the core-cladding interface along the fiber, through a mechanism known as total internal reflection (TIR), and this effect makes the fiber transmit signals over longer distances at higher data rates than other forms of communication; additionally, fibers offer lower attenuation and immunity to electromagnetic interference [2, 3].

Due to the exponential growth in the demand for transmission capacity, it is already evident that the next generation of telecommunication networks will be radically different from the existing one.

Besides their applications in telecommunications, optical fibers are also widely used for remote sensing, medical imaging, illumination, machining and welding applications because of their smaller size, lighter weight, chemical inertness, larger bandwidth, longer repeat span, electromagnetic immunity, and many other intriguing properties [3, 4].

The importance of optical fibers increased in the last decade. Coherent detection, with powerful digital signal processing, is used to maximize the available capacity of each optical fiber within a network; however, without a radical innovation in the growth of the basic infrastructure of the Internet, the application of these techniques will only delay the inevitable crisis of capacity for a few years.

The internet of the future will be severely restricted. Research on new fiber transmission of information is something that is urgently needed. In recent years, two new kinds of optical fibers have revolutionized this dynamic field,

bringing a wide range of new optical properties. These new fibers, known as photonic crystal fibers or microstructured fibers, can be manufactured entirely from a single type of glass (or polymer), since it is not based on a dopant for the transmission of light. In these fibers, unlike in conventional ones, the cladding is made up of small air holes, traveling along the fiber.

Goals

Through my Ph.D. work, "Design, Fabrication and Investigation of Special Microstructured Fibers", we expected to obtain the following results:

In the first stage, we expected to obtain more regular structures of air-holes in the PCF and less attenuation in these fibers, and we intended to get a finer and more precise control of the geometrical parameters of the fabricated fiber, such as the core diameter, the diameter of the holes (d) and the d/Λ ratio.

As the second and more important goal, we tried to obtain different kinds of High Nonlinearity (HNL) PCF. First, we tried to obtain some HNL PCF similar to the already fabricated and commercially available fibers. Then, we tried to optimize these fibers using the empirical method of HNL PCF design to calculate a flattened HNL PCF, which is a PCF that has a large bandwidth with values very close to zero dispersion. We also tried to fabricate the designed PCF with flattened dispersion for different numbers of air-hole rings around the core.

As the next step, we measured the obtained geometrical parameters of those special fibers, measured the attenuation in all the fabricated fiber, and we analyzed dispersions of each one.

Also, we tried to demonstrate that when we have a lower number of air-hole rings around the core in a PCF, it is possible to obtain single-mode fiber transmission, even at the d/Λ ratio of 0.6.

As the last goal, we tried to achieve supercontinuum generation in the fabricated fibers for different wavelengths, in order to analyze in which bandwidth this effect appears. We compared our results for different fabricated fibers.

There are some theories and calculations of flattened HNL PCF, especially with different air-hole diameters on each layer around the core, but nobody has already fabricated these fibers, and we tried to do so as part of this work.

We also planned to analyze the different micro-structured fibers (Large Mode Area (LMA) and HNL) to know their polarimetric behavior.

It is important to analyze their optical parameters as much as it is possible, just to know more about our fabricated (home-made) fibers.

As specific results, we expected to obtain the following:

- Optimized LMA PCFs with regular structure and low attenuation.
- HNL PCFs with regular structure and with one wavelength of zero dispersion (for the 800 nm and 1040 nm wavelength range).
- An HNL PCF for near flattened supercontinuum generation (this one may have an irregular structure; it means with different air-hole diameters on each layer).
- At least 3 scientific publications in international optical journals, with an impact factor sum of at least 4.
- At least 3 participations in national and international conferences.
- One international pre-doctoral practice stay.
- One national pre-doctoral stay in the industry.

Acknowledgments

First of all, I want to thank Dr. Uladzimir P. Minkovich for all of his advice and support over the last 4 years, and also for being a great person and a great professional.

I thank Dr. Sergio Calixto for all the time he spent with me in the lab, doing the measurement of the fiber structures with an atomic force microscope, and for reading this thesis.

I profoundly thank Dr. Yuri Barmenkov for all his help and orientation in the process of writing my research papers.

I would like to thank Dr. David Monzon Hernandez and Dr. Rafael Espinosa Luna for their helpful discussions.

I want to thank Mario Ruiz Berganza for his help in improving my English, and for the revision of my research papers and of this thesis.

Also, I want to thank Dr. Joel Villatoro for his support and orientation in the field of optical sensors and devices.

Finally, I want to thank my parents for being so understanding with my decisions, and of course, I want to thank CONACYT for all the financial support through these years.

List of acronyms

AFM	Atomic force microscopy
BF	Bragg fiber
ESM	Endlessly single mode
FEM	Finite element method
GVD	Group velocity dispersion
HC	Hollow core
HNL	High nonlinearity
LIC	Low index core
LMA	Large mode area
mPOF	Microstructured polymer optical fiber
MTIR	Modified total internal reflexion
NA	Numerical aperture
PCF	Photonic crystal fiber
PMMA	Poly(methyl methacrylate)
POF	Polymer optical fiber
SMF	Single-mode fiber
TIR	Total internal reflexion
UV	Ultraviolet
ZDM	Zero dispersion wavelength

Contents

List of Figures

List of Tables

Chapter 1

Overview of Optical Fibers

1.1 Introduction

This chapter contains an overview of Optical Fibers, at first the physical phenomenon of total internal reflection to explain a conventional all-solid step index fibers, losses (or attenuation) in the fibers and then an overview of Photonic Crystal Fibers, including the classification of them. Also we will present an overview of group velocity dispersion. Then it is shown that group velocity dispersion can be widely engineered in photonic crystal fibers due to a strong contribution from waveguide dispersion. Other important properties of photonic crystal fibers such as loss, numerical aperture, geometrical parameters, band gap guidance and birefringence are then briefly explained.

1.2 The phenomenon of total internal reflection

The phenomenon that maintain the light into the core of the optical fibers is known as total internal reflection and happens in the interface between the core and the cladding. It means that the light is transmitted by multiple reflections along the fiber. The condition of this effect exists only when the rays impinge at an angle less than the critical angle. The value of critical angle is possible to obtain from the Snell law:

$$n_1 sin\theta_1 = n_2 sin\theta_2 \tag{1.1}$$

In the figure 1.1 three rays are shown with different angles of incidence. We can see: a) the refraction of light, b) the critical angle, and c) the total internal reflection [3],[12].

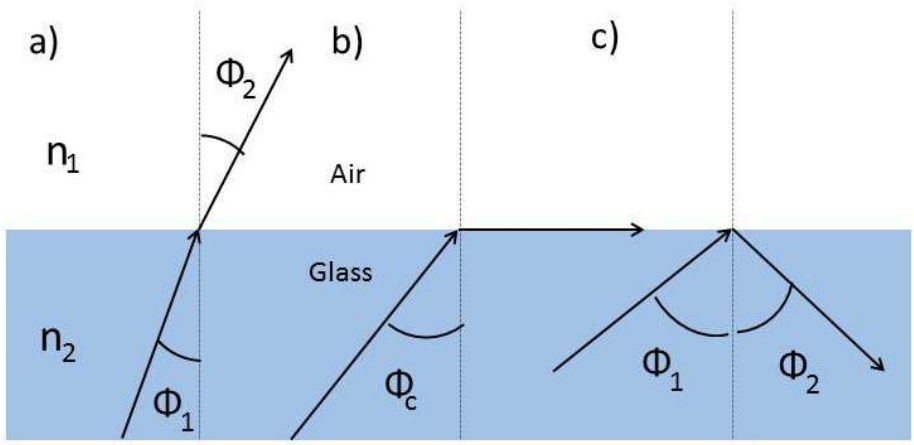

Figure 1.1: a) refracted ray, b) critical angle, and c) total internal reflection

1.3 Conventional step-index fiber

The optical fiber is one of the great inventions of the XX century, and have a lot of application as in telecommunication as in other fields of optics. The optical fiber, having an outer diameter mostly of about 125 μm, like a hair thread, has the capacity to transmit a lot of information in very long distances and with very high speed [1]. A conventional silica fiber is an optical waveguide consisting of a core with higher refractive index, surrounded by a cladding glass with lower refractive index. Due to the refractive index difference, guidance of certain wavelength of electromagnetic radiation (normally visible light or near infrared region for telecommunication) in the core can occur by total internal reflection. Figure 1.2 shows a typically index profile for a step index fiber. Exist other index profiles, where the refractive index changes slowly from the core to the cladding, this kind of profiles is called graded index, and also exist another index profiles in dependence of the applications [13]. The guidance of light through total internal reflection was first demonstrated in the XIX century, in a stream of water [14]. Later, this experiment was applied in glasses [15]. In the middle of the XX century, the concept of adding a cladding with lower index to the outside of a glass fiber was introduced [16].

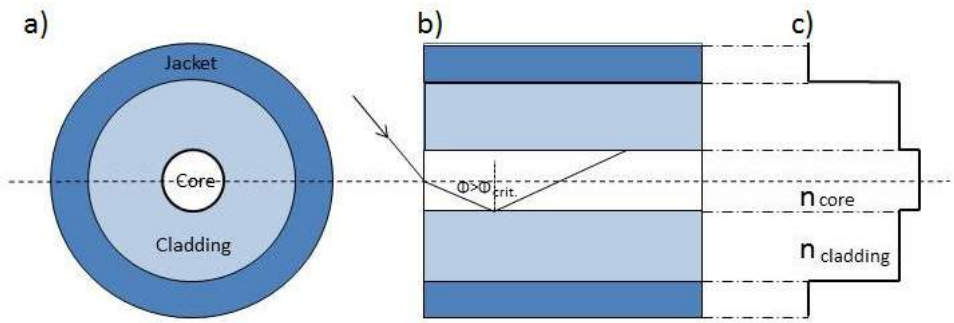

Figure 1.2: a) Step-index cross section, b) Step-index transversal section to show guidance by total internal reflection, and c) refractive index profile across the fiber diameter

1.4 Modes

When Maxwells equation are used to perform a full analysis of how light propagates in optical fiber, a discrete set of transverse electric field profiles which propagate without (confinement) loss are found [17]; these solutions are called bound modes (and will henceforth be referred to as modes). Modes have a transverse field profile that does not vary in magnitude with propagation, only the phase of the field varies in a manner determined by the propagation constant of the mode.

$$\gamma = \alpha + i\beta \tag{1.2}$$

Where γ is the propagation constant, α as a real part is the attenuation constant, and β as a imaginary part is the phase constant.

Waveguides that only support the fundamental mode are referred to as single mode, meanwhile waveguides that support additional higher order modes are referred to as multimode. In a conventional step index fiber higher order modes begin to be supported when the normalized frequency V is greater than 2.405, where:

$$V = \frac{2\pi}{\lambda} r_{\text{core}} \sqrt{n_{\text{co}}^2 - n_{\text{clad}}^2} \tag{1.3}$$

Where r_{core} is the radius of the fiber core, n_{co} is the refractive index in the core and n_{clad} is the refractive index in the cladding. An example of single

mode and multimode fibers is shown in the figure 1.3a and 1.3b respectively. These pictures are taken in the output of a single- and multimode fibers, lighted with a Helium Neon laser with a wavelength of 632.8 nm. In other words. These fibers are a single- and a multimode fiber for the such wavelength.1.3

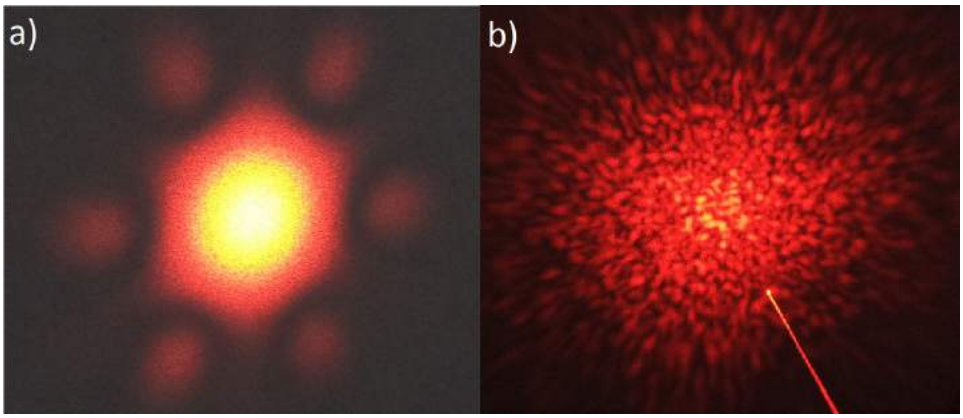

Figure 1.3: a) output image from a single-mode fiber, b) output image from a multimode fiber.

The two dimensional waveguide such is a step index fiber can support polarized light in two transversal directions. If the refractive index contrast between the core and the cladding is small, two dimensional field profiles can be thought to comprise two orthogonal linearly polarized modes [18]. Therefore, the single-mode fiber has not really a single-mode, but it supports two separate orthogonally polarized modes. In real fibers, some imperfections exist, which arise during fabrication, that is why two orthogonally polarized modes have different modal properties. This variation of modal properties with polarization is referred to as birefringence.

1.5 Photonic Crystal Fibers

Photonic crystals are periodic structures on the scale of a wavelength of light. Photonic crystals can be incorporated into the cladding of an optical fiber, producing photonic crystal fibers (PCFs). These fibers were introduced in the 1990s [19]. Photonic crystal fibers have some unique properties which set PCFs apart from conventional optical fibers. Usually PCFs are fabricated from pure silica, with an array of air holes in the cladding which run the entire length of the fiber. Alternatively, doped silica rods can be used instead

of air, or the air holes can be filled after fabrication with some liquid or gas.

Generally, PCFs can be split into two main groups: index guiding PCF and band gap guiding PCF. Index guiding PCFs have a solid core, which has an air-hole array around, this core is a missing hole in the center of the structure. Examples of these structures are shown in figure 1.4(a) and 1.4(b). Guidance in the solid-core PCF occurs in a similar way to total internal reflection in conventional fibers. The effective refractive index of the air hole lattice in the cladding is lower than the refractive index of the core material, and so guidance occurs by modified total internal reflection (MTIR). The second important group of the PCF cladding is the photonic band gap fiber, so called because the guidance in this case is due to the band gap effect. This effect allows light to be guided in a low-index core, such as a hollow air core, as can be seen in the figure 1.4(c).

The dimension of the photonic crystal cladding are described using the hole to hole spacing, or pitch (Λ), and the hole diameter (d). By changing the pitch and hole sizes, the dispersion and nonlinearity can be changed. The number of rings of air holes in the cladding around the core is also a very important parameter, impacting on confinement loss.

PCF can also be fabricated with multiple cores[20] to provide a high packing density of cores for endoscopy applications, or to provide cores with different properties suitable for pulse delivery and collection[21]. Air-silica PCFs are useful for sensing, because gases and liquids are able to penetrate into the air holes either from the fiber end or by drilling holes at regular intervals into the cladding along the length of the fiber [22]. Hollow core PCF can be filled with gases[23] and liquids[24] in order to increase their nonlinearity, and they can be also used to confine and guide particles [25, 26].

1.6 Classification of Photonic Crystal fibers

This section gives an overview of five PCFs:

Endlessly single-mode fiber

Large mode area photonic crystal fiber

High nonlinearity

Hollow core

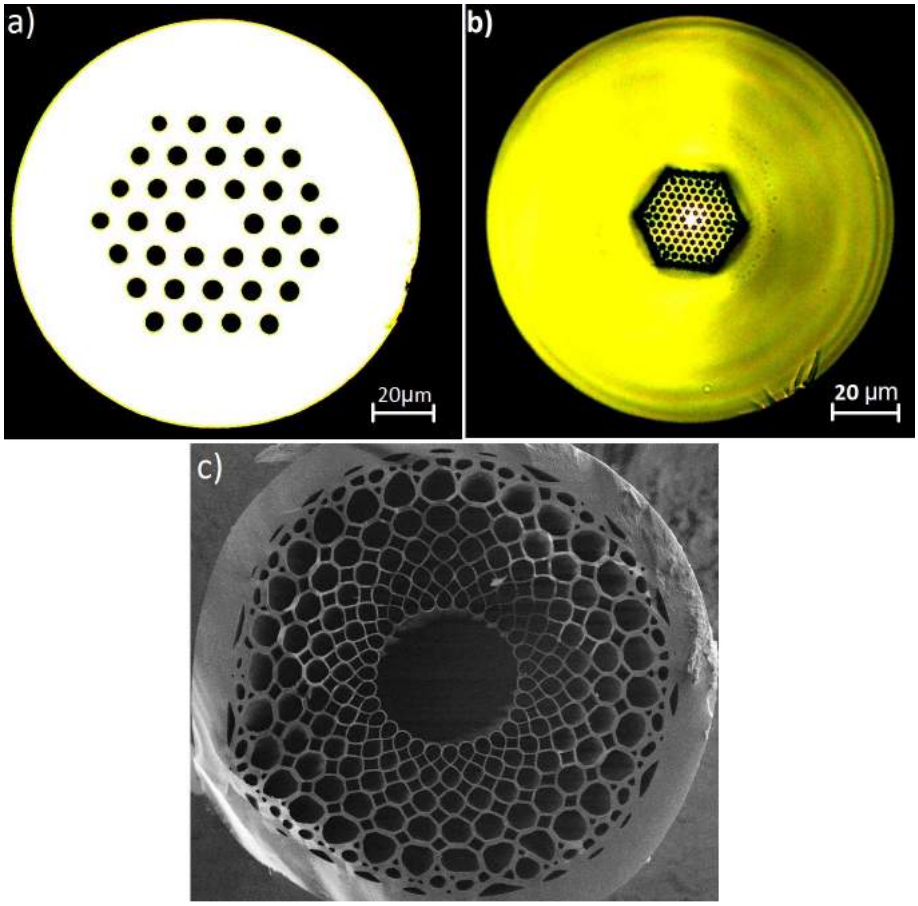

Figure 1.4: a)Large Mode Area PCF, b) High Nonlinearity PCF c) Hollow Core PCF (this picture is taken from reference [9]).

Kagome fiber

1.6.1 Endlessly single-mode fiber

This kind of fiber is designed to guide only one mode (the fundamental mode) independently of the wavelength. The structure of the fiber has a filling fraction $d/\Lambda < 0.4$ [27]. The single-mode nature of the ESM fiber is due to the dispersive nature of the cladding. As the wavelength decreases, light in the silica regions of the cladding decays quickly in the air regions and the effective index of the cladding tends to that of silica. This creates

a low refractive index contrast between the core and cladding keeping the fiber single-mode, however also making it susceptible to bend loss [28].

1.6.2 Large mode area photonic crystal fiber

Being a single mode fiber in a very wide range of wavelengths, a large mode area PCF has a big core area. This kind of fibers is useful for generating and propagating high optical powers [29]. Normally the ratio d/Λ for this fibers is lower than 0.4.

1.6.3 Highly nonlinear

This fiber consists of a silica core surrounded by a web of thin silica strands and are frequently used to observe nonlinear effects. The high index contrast created between the silica core and the air cladding strongly confine light to a core that can be less than 1 μm in diameter (commonly between 1μm and 5 μm), the guided mode of which experiences a large nonlinearity. Furthermore, by tailoring the pitch and air filling fraction of the cladding, significant control over dispersion of the fiber is possible allowing a high figure of merit for nonlinear interactions to be obtained [30].

1.6.4 Hollow core fiber

Hollow core fibers use micro-structured cladding region with air holes to guide light in a hollow core. The photonic bandgap guiding mechanism is fundamentally different from the traditional total internal reflection guiding principle. In this kind of fibers the 99 % of the light can propagate in air [31]. This kind of fibers is highly multimode.

1.6.5 Kagome fiber

Kagome fibers are also highly multimode, allowing the guidance of light in an air core with a typical loss of 1 dB/m. The cladding is larger than that of HC PCFs, with a typical pitch of 12 μm and does not support a bandgap [32].

The low loss of the core guided modes is due to the small overlap integral between the core and cladding modes. Cladding modes are highly confined

in the silica strand and exhibit a fast transverse phase oscillation. Core modes are confined to the air exhibiting a slow transverse phase oscillation [33].

1.7 Losses in fibers

In some systems the loss is defined as a relationship between the energy that is given to the system to the energy in the output of the system. In the case of optical fibers it is the same, but here exist different kinds of reasons causing the losses, that is described in detail.

1.7.1 Absorption losses

The losses in conventional or step index fibers, made of pure silica, for wavelength range from 0.8 μm up to 1.8 μm are very low, and theoretically, the electromagnetic radiation in this range of wavelengths can travel hundreds of kilometers without suffering a remarkable loss. Until 70s of the last century the absorption losses were considerable high, due to the material impurity, which could contain water or some metals together with the silica. G.A. Thomas et al. [34], demonstrated that optical fibers can be manufactured with a very low absorption loss, and consequently the losses of this fibers are very low. This kind of fibers can have an absorption loss about 0.18 dB/Km, in the wavelength of 1.55 μm, enabling the information transmission without amplification for hundreds of kilometers.

1.7.2 Bending losses

The origin of the losses by bending is explained below: In the fiber without bending, incidence rays with the greatest angle can be reflected by the effect of total internal reflection and reach the end of the fiber, while in the same fiber with bending, these rays leave the fiber just in the curvature, making the fiber have higher losses in dependence of the curvature angle [35].

1.7.3 Other factors

There exist other factors that happen in optical fibers and insert them losses: - Losses for Rayleigh scattering, that increases as the wavelength approaches that of the size of density fluctuation frozen in the glass during the manufacturing process. Loss from Rayleigh scattering scales as:

$$\alpha_{\text{Rayleigh}} = \frac{C_{\text{R}}}{\lambda^4} \tag{1.4}$$

Where C_R is the Rayleigh constant and λ is the wavelength of transmission.

Rayleigh scattering typically takes a value between 0.7-0.9 dB/(km.μm), in silica fibers. - Silica has vibrational resonances in the infra red and losses increase rapidly beyond 1.6 μm. - Across the transmission window loss is affected by impurities present in the glass, the most significant being absorption from the OH group. The groups fundamental vibrational resonance is centered at 2.73 μm, it however has harmonics at 1.38 μm, 0.95 μm and 0.72 μm as well as a peak at 1.23 μm. Typically the number of OH ions in high grade optical silica is less than one part per hundred million. This is achieved by displacing them during the manufacturing process with a more reactive ion such as C1 which has resonances in the UV.

1.7.4 Attenuation (or full losses)

As the amount of light loss in a length L of a fiber takes the form of a fraction of the input light, decibels are used to specify the attenuation constant α_{dB}.

$$\alpha_{\text{dB}} = \frac{-10}{L} log \frac{P_{out}}{P_{in}} \tag{1.5}$$

A typical value for commercially available fiber can be as low as 0.2 dB/km at 1550 nm. This value varies by several orders of magnitude across the guided wavelength range.

1.8 Dispersion

In telecommunication systems, the information is transmitted by binary data, which consists in optical pulses. In Optical waveguides, the dispersion

is one of the most important characteristics for a right data transmission. There are 4 principal causes of dispersion:

1.8.1 Intermodal dispersion

This kind of dispersion only exists in multimode fibers, and is the difference of the propagation of the different modes. The dispersion value is function of the wavelength.

1.8.2 Material dispersion

The material dispersion is the most important, because it depends only on the material. Spectrally, the light consists of a range of frequencies, which are located around the frequency modulation of the source, and based on the material each spectral component that will propagate at different velocities, in other words, for concrete material each wavelength has a different refraction index.

1.8.3 Waveguide dispersion

Even for the materials without dispersion, the solution for the propagation equations depends on the wavelength: The propagation constant of the mode depends on the wavelength. This leads to a pulse propagation and a deformation of the same for the same reasons.

1.8.4 Polarization dispersion

That is in fact the same phenomenon that happens in the intermodal dispersion, but the modes here are originally degenerated. It is possible to see that the single-mode fiber has 2 degenerated modes [36].

1.9 Sellmeier Equation

The refractive index of a material is linked to the resonances of bound electrons in the medium as such frequency dependent. Far from these resonances

the refractive index of bulk silica is well approximated by the following Sellmeier equation [37], where λ_j represents the wavelength of a resonance and aj its strength.

$$n = 1 + \sum_{j=1}^{3} \frac{a_j \lambda^2}{\lambda^2 - {\lambda_j}^2} \tag{1.6}$$

The most common material using for fiber fabrication in this thesis is the silica or quartz, which has the following coefficient for Sellmeier equation: λ_1=0.0684043, λ_2=0.1162414, λ_3=9.896161, and a_1=0.6961663, a_2=0.4079426, a_3=0.8974794.

1.10 Calculating photonic crystal fiber dispersion

It is possible to calculate the dispersion in PCFs. Optical fibers do not have the same dispersion as the core material they are made, because there is a contribution to their dispersion which depends on the geometry of the waveguide. Step index fibers have relatively small core-cladding index contrast (only about 1 %), and the mode is not tightly confined to the core.

Therefore the waveguide contribution to dispersion is weak, and the dispersion profile is close to the bulk material dispersion. It is possible to shift the zero dispersion wavelength (ZDW) by changing the core size or the doping level [38].

It is important to remark that in PCF the scope for dispersion changing is far greater. The core cladding contrast can be much higher in PCFs than in step index fibers. For example, the ZDW can be shifted to visible wavelength [39]. This special dispersion profile is of vital importance for creating low-noise supercontinuum sources, and also for the ultra-flattened dispersion in PCFs [40].

The waveguide dispersion of the PCFs can be controlled by adjusting the pitch Λ and/or the hole diameter d of the cladding. PCF with extremely high air filling fractions can be approximated as a strand of silica surrounded by air. Same samples of dispersion curves possible in PCF for different cladding dimensions are plotted in figure 1.5. These were calculated using the empirical formula in [10]. For a constant Λ, increasing d/Λ produces a more anomalous dispersion profile. For a constant value of d/Λ, increasing

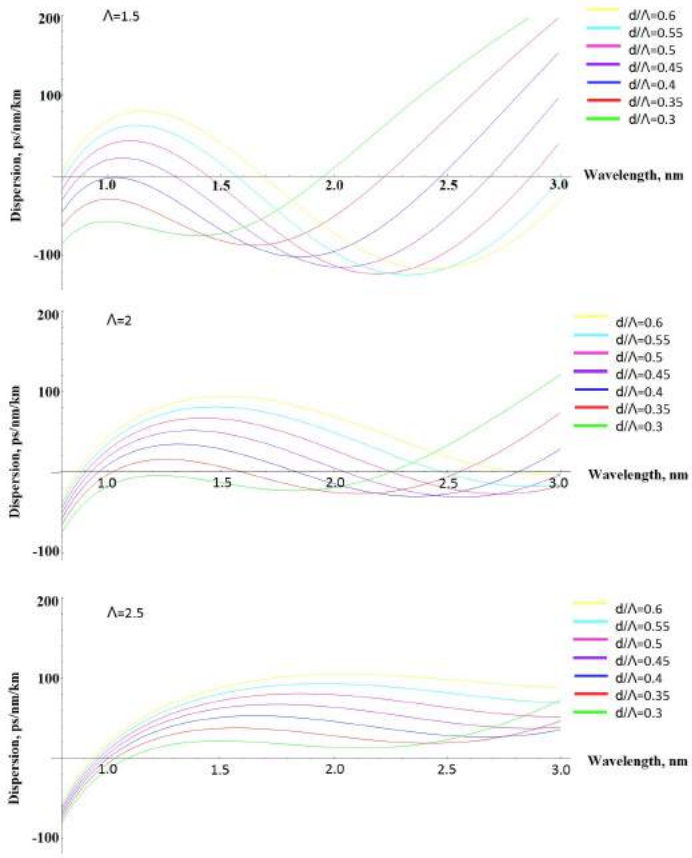

Figure 1.5: Dispersion calculated using empirical formula [10] for photonic crystal fiber with different values of Λ, and ratio d/Λ to show how the change of cladding parameter affects the dispersion on the fiber.

Λ makes the dispersion more anomalous, and also shifts the zero dispersion, or the minimum dispersion, to longer wavelengths.

1.11 Overview of the Fabrication process

PCFs can be fabricated using a variety of different materials, and methods. The most common method for the PCF fabrication is the stack and draw method [41], which includes stacking capillaries and rods, which are then drawn down to create a preform [42]. This method is used to fabricate the

PCFs described in Chapters 3 and 4.

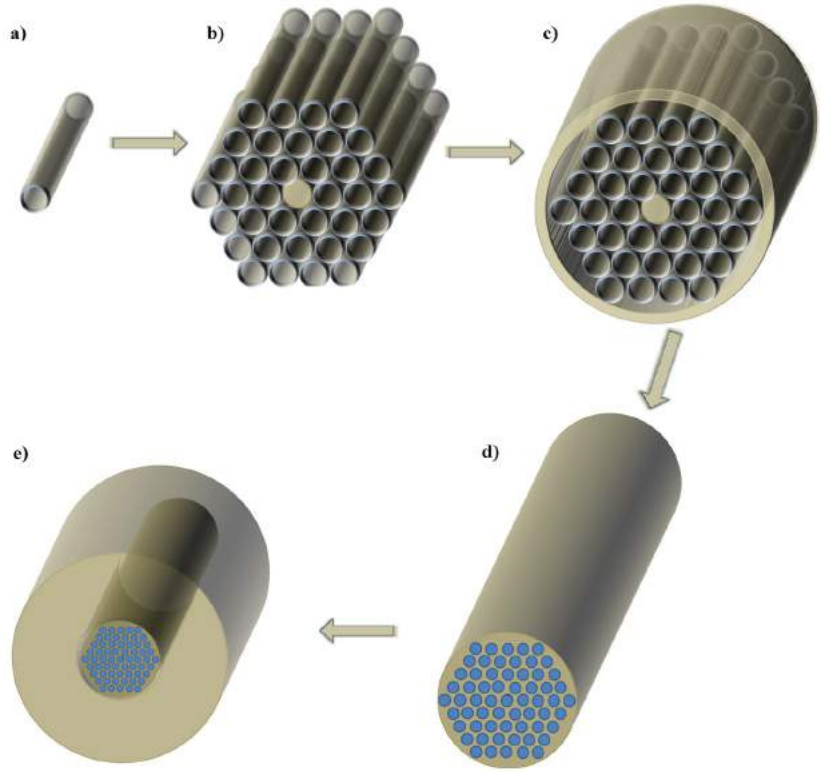

Figure 1.6: a) Draw capillaries and rods to about 1 mm, b)Build stack, c) draw the preform to obtain a cane of about 2-3 mm, d) insertion of the cane into a jacket tube to obtain the designed PCF.

Most fiber fabrication techniques, which include the stack and draw method, use a fiber drawing tower. Figure 1.6 shows a schematic representation of a fiber drawing system. The main idea of this system is to fabricate the fiber without contact between the preform and the furnace; this is in order to not contaminate the fiber due to the contact with other materials. The furnace heats the preform to a temperature of about 2000 °C. The preform is then fed into the furnace at a relatively low speed (in mm/min) and then the glass, emerging from the bottom of the furnace, is pulled at a higher speed (normally in m/min). The generalized procedure for the stack and draw method is shown in the figure 1.7. Firstly it is necessary to draw the capillaries and the rods to build the preform (this capillaries and rods are designed previously to obtain them with the required dimensions). The starting materials are pure silica rods and tubes which are produced

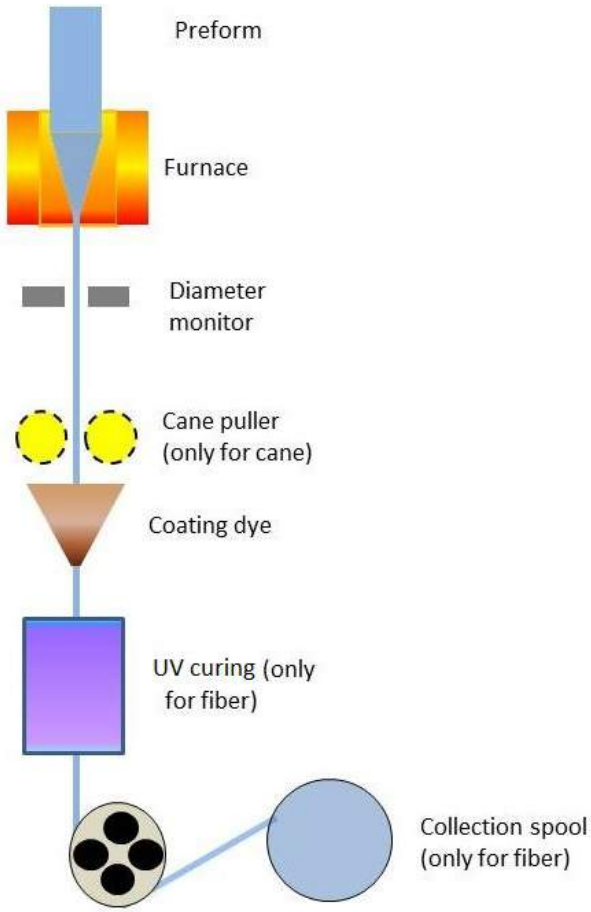

Figure 1.7: Schematic illustration of fiber drawing process with the different parts of the drawing tower.

commercially, and are typically 1m or 1.5 m long and about 20 mm in diameter (The maximum diameter that can be used is 25 mm, due to the small diameter of the existing in CIO furnace). The final capillaries drawn from these tubes have lengths of about 1 m and the outer diameter of about 0.8-1.5 mm. Then, it is necessary to stack the capillary manually in a hexagonal arrangement. A solid core fibers have a solid rod at the center of the capillary array to act as a core, while in a hollow core fiber it is necessary to remove the central capillary to obtain a hollow core PCF.

The stack is then inserted into another fused silica tube, which have an inner diameter of about 16-20 mm, and then it is necessary to draw this

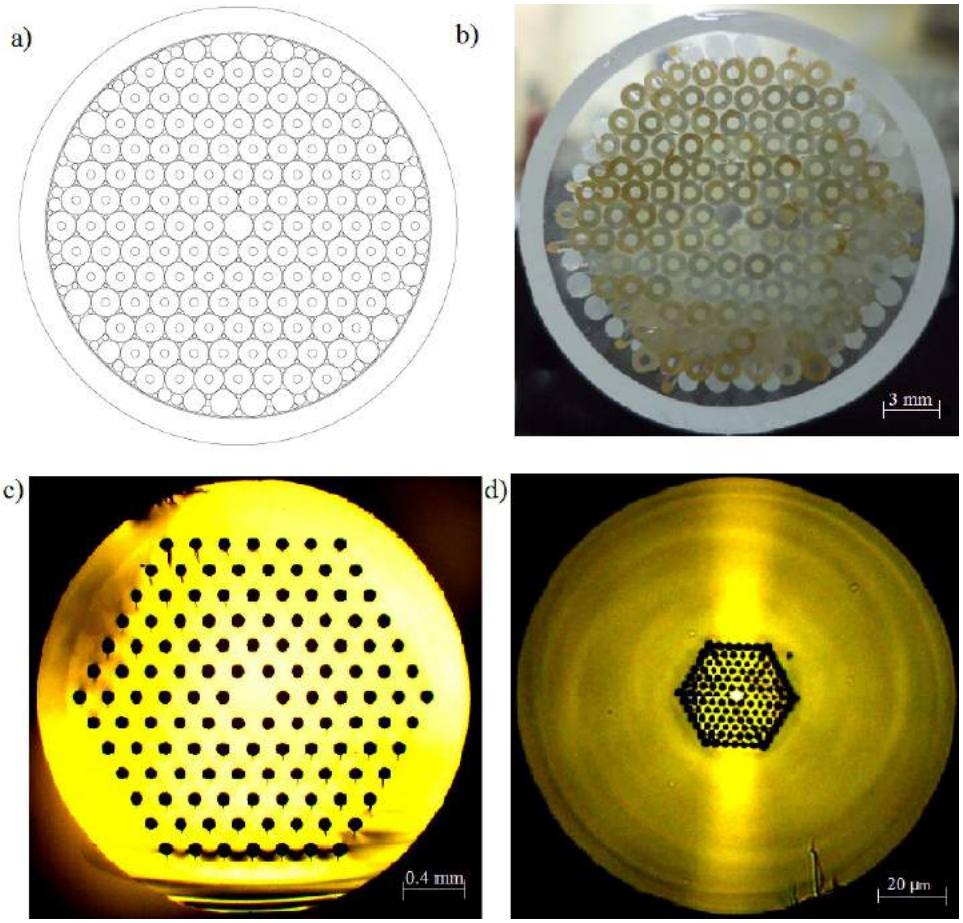

Figure 1.8: a) design of 6 rings PCF, b) Preform ready to be drawn, capillaries and rods arrangement, c) cane, d) PCF with outside diameter of 123,5 μm.

preform to obtain the cane of about 2-3 mm in outside diameter (or in case of LMA PCF it is possible to obtain the fiber in this first drawing process). After this drawing process it is necessary to put the cane into a so called jacket tube, a tube with inner diameter of about 2-3 mm and outer diameter approximately of 10-12 mm. Then it is necessary to make the last drawing process of this preform to obtain the required fiber. PCF stacks are generally drawn to fiber in two stages. In the first step the cane is drawn (it is shown in the figure 1.8(c)), in the second step a cane is inserted inside jacked tube, to create a preform that is then drawn to a fiber, shown in the figure 1.8(d), it is also necessary to introduce a pressure into the structure to control the capillary diameters in the PCF.

Fabricated fibers after this process are shown in figure 1.8(d). As the fiber emerges from the furnace, it passes through a container (the coating dye), where the liquid polymer remains, and after that the fiber goes through the UV curing system, that is a group of ultraviolet lamp in a special refrigerated structure. The fiber external cladding has two important functions: the first, to delete cladding modes and the second, to make a mechanical protection of an optical fiber glass surface. Typically several kilometers of fiber can be fabricated during one fiber draw.

PCF can also be fabricated by extrusion. Molten glass is forced through a die which molds it to the correct structure [43]. This can be used to create structures not possible using stack and draw method, and is useful, when using materials such as doped silica, polymer, or chalcogenide glasses, which are not commonly available in tube form.

Chapter 2

Empirical method for design of Photonic Crystal Fibers

2.1 Introduction

Photonic crystal fibers (PCFs) [44] have been under intensive study as they offer design flexibility in controlling the modal properties. Photonic crystal fibers have some extraordinary properties, such as wide single-mode wavelength range, unusual chromatic dispersion, and high or low nonlinearity. Theoretical descriptions have based normally on numerical approaches, such as the plane wave expansion method [45], the multipole method [46], the finite element method (FEM) [47, 48] and another methods. However, numerical simulations are, in general, time-consuming and costly. Recently, an analytical approach based on the V parameter (normalized frequency), frequently used in the design of conventional fiber, has been developed for PCFs [49]. Although the V parameter offers a simple way to design a PCF, a limiting factor is that a numerical method is still required to obtain the accurate effective cladding index. The empirical relations of V and W parameters only depend on wavelengths and the structural parameters, that is why they will very useful for the simple design of the PCFs. The geometrical parameters required for the V and W parameters of the PCFs are: the air hole diameter (d) and the hole to hole distance or pitch (Λ). This method demonstrates enough accuracy in comparison with full-vector FEM. Through the empirical relations we can easily evaluate the fundamental properties of PCFs without the need of numerical computations.

2.2 Some parameters for this method

For the V parameter it is important to consider that we have a triangular lattice of air holes into a silica glass that has a refractive index of 1.44 at wavelength of 1.55 μm. The triangular PCFs can be well determined in terms of the V parameter that is given by:

$$V = \frac{2\pi}{\lambda} a_{\text{eff}} \sqrt{n_{\text{co}}^2 - n_{\text{FSM}}^2} = \sqrt{U^2 + W^2}, \tag{2.1}$$

$$U = \frac{2\pi}{\lambda} a_{\text{eff}} \sqrt{n_{\text{co}}^2 - n_{\text{eff}}^2}, \tag{2.2}$$

$$W = \frac{2\pi}{\lambda} a_{\text{eff}} \sqrt{n_{\text{eff}}^2 - n_{\text{FSM}}^2}, \tag{2.3}$$

where λ is the operating wavelength, n_{co} is the core index, n_{FSM} is the cladding index, defined as the effective index of the so-called fundamental space-filling mode in the triangular air hole lattice [28], n_{eff} is the effective index of the fundamental guided mode, and a_{eff} is the effective core radius that here is assumed to be $\Lambda/\sqrt{3}$ [47, 49]. The parameters U and W are called, respectively, the normalized transverse phase and attenuation constants. Mortensen et al. proposed the following effective V_{eff} parameter [8] for triangular PCFs:

$$V = \frac{2\pi}{\lambda} \Lambda \sqrt{n_{\text{eff}}^2 - n_{\text{FSM}}^2} \tag{2.4}$$

and reported the empirical relation for V_{eff} of Eq. 2.4[50]. However, this definition is intrinsically different from the original V parameter definition in step-index fiber (SIF) theory and corresponds to the W parameter. Therefore it seems to be difficult to apply the design principle of SIFs straightforwardly to PCFs. So we adopt the V parameter definition of Eq. 2.1 . Although we can estimate the fundamental properties of PCFs using the V parameter in Eq. 2.1[49] , a limiting factor for using Eq. 2.1 is that a numerical method is required for obtaining the accurate effective cladding index n_{FSM}. Figure 2.1 shows V values calculated through vector FEM [50] as a function of λ/Λ for d/Λ ranging from 0.2 to 0.8 in steps of 0.05. By trial and error, we find that each data set in Fig. 2.2 can be fitted to a function of the form

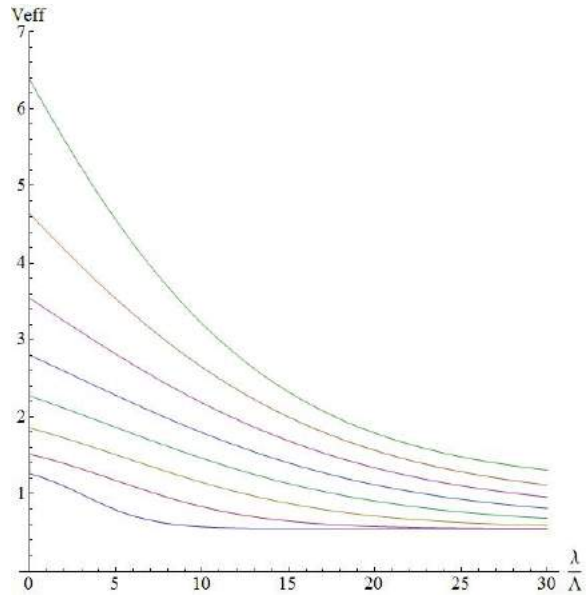

Figure 2.1: Effective V parameter as a function of λ/Λ.

$$V\left(\frac{\lambda}{\Lambda},\frac{d}{\Lambda}\right) = A_1 + \frac{A_2}{1 + A_3\, exp(A_4\lambda/\Lambda)} \tag{2.5}$$

and the results are indicated by the curves. For accurate fitting, the data sets are truncated at V = 0.85. In Eq. (5) the fitting parameters A_i (i = 1 to 4) depend on d/Λ only. The data are well described by the following expression 2.6

$$A_i = a_{i0} + a_{i1}\left(\frac{d}{\Lambda}\right)^{b_{i1}} + a_{i2}\left(\frac{d}{\Lambda}\right)^{b_{i2}} + a_{i3}\left(\frac{d}{\Lambda}\right)^{b_{i3}}, \tag{2.6}$$

the coefficients a_{i0} to a_{i3} and b_{i1} to b_{i3} are given in Table 2.1. For $\lambda/\Lambda < 2$ and $V \geq 0.85$ the expression 2.5 gives values of V which deviates less than 1.3% from the corrected values obtained from Eq. 2.1.

Using the effective V parameter in Eq. 2.5, the effective cladding index n_{FSM} can be obtained without the need for numerical computations. Figure 2.2 shows n_{FSM} as a function of λ/Λ for d/Λ ranging from 0.1 to 0.8 in steps of 0.1, where the curves show the results from Eqs. 2.1 and 2.5 with $a_{\mathrm{eff}} = \Lambda/\sqrt{3}$. Mortensen et al.[51] proposed the empirical expression for the value of n_{FSM} nFSM to directly fit the effective cladding index, however,

	$i=1$	$i=2$	$i=3$	$i=4$
a_{i0}	0.54808	0.71041	0.16904	-1.52736
a_{i1}	5.00401	9.73491	1.85765	1.06745
a_{i2}	-10.43248	47.41496	18.96849	1.93229
a_{i3}	8.22992	-437.50962	-42.4318	3.89
b_{i1}	5	1.8	1.7	-0.84
b_{i2}	7	7.32	10	1.02
b_{i3}	9	22.8	14	13.4

Table 2.1: Coefficients to find the V parameter.

the results are not so accurate. On the other hand, the expression of Eq. 2.5 gives values of n_{FSM} which deviates less than 0.25% from the values obtained through vector FEM for $\lambda/\Lambda \leq 1.5$ and $V \geq 0.85$.

In Ref. [49] and in Eq. 2.5 the cutoff condition is given by V=2.405, as in conventional SIFs. Using the empirical relation 2.5 and various formulas in terms of the V parameter found for SIFs, we can easily estimate the fundamental properties of PCFs, such as mode field diameter, beam divergence, splice loss, and so on [49].

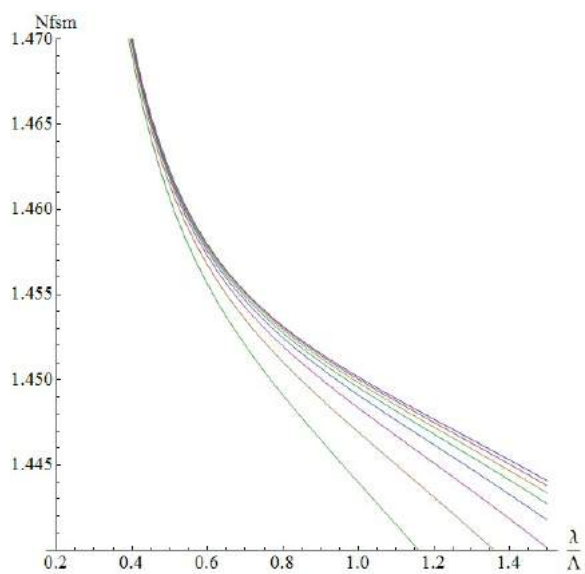

Figure 2.2: Effective cladding index as a function of Λ/Λ

2.3 The W parameter expression

In the previous section we provided the empirical relation for the V parameter of PCFs. Using Eq. 2.5 we can easily obtain the effective cladding index n_{FSM}, however, we usually need heavy numerical computations to obtain the accurate values of n_{eff} in Eq.2.3. It would be more convenient to have an empirical relation for the W parameter of PCFs. Nielsen et al. have reported the empirical relation for the W parameter [50], however, we can not obtain the value of neff from the W parameter only. In order to obtain n_{eff}, we need the empirical relations for both the V and W parameters.

Figure 2.3 shows W values calculated through vector FEM [48] as a function of λ/Λ for d/Λ ranging from 0.1 to 0.8 in steps of 0.1. Again, by trial and error, we find that each data set in Fig. 2.3 can be fitted to the same function in Eq. 2.5 as

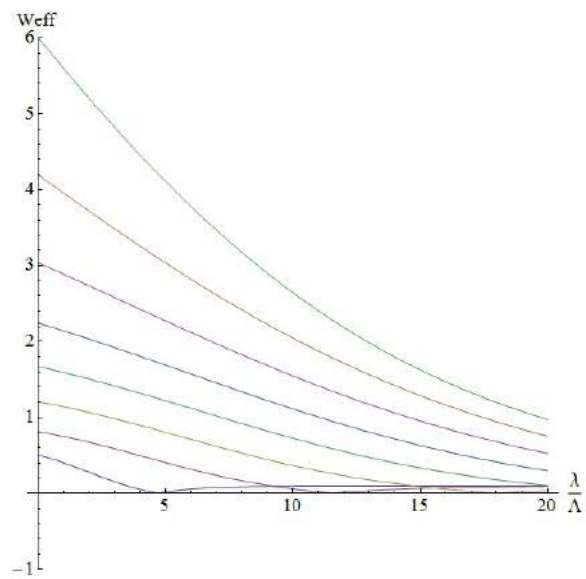

Figure 2.3: Effective W parameter as a function of λ/Λ

$$W\left(\frac{\lambda}{\Lambda},\frac{d}{\Lambda}\right) = B_1 + \frac{B_2}{1+\ B_3\, exp(B_4\lambda/\Lambda)} \tag{2.7}$$

and the results are indicated by the curves 2.3. For accurate fitting, the data sets are truncated at W = 0.1. In Eq. 2.7 the fitting parameters B_i (i

= 1 to 4) depend on d/Λ only. The data are well described by the following expression

$$B_i = c_{i0} + c_{i1}\left(\frac{d}{\Lambda}\right)^{d_{i1}} + c_{i2}\left(\frac{d}{\Lambda}\right)^{d_{i2}} + c_{i3}\left(\frac{d}{\Lambda}\right)^{d_{i3}} \tag{2.8}$$

and the coefficients c_i and d_i c_{i0} to c_{i3} and d_{i1} to d_{i3} are given in Table 2.2:

	$i = 1$	$i = 2$	$i = 3$	$i = 4$
c_{i0}	-0.0973	0.53193	0.24876	5.29801
c_{i1}	-16.70566	6.70858	2.72423	0.05142
c_{i2}	67.13845	52.04855	13.28649	-5.1830
c_{i3}	-50.25518	-540.66947	-36.80372	2.7641
d_{i1}	7	1.49	3.85	-2
d_{i2}	9	6.58	10	0.41
d_{i3}	10	24.8	15	6

Table 2.2: Coefficients to find the W parameter.

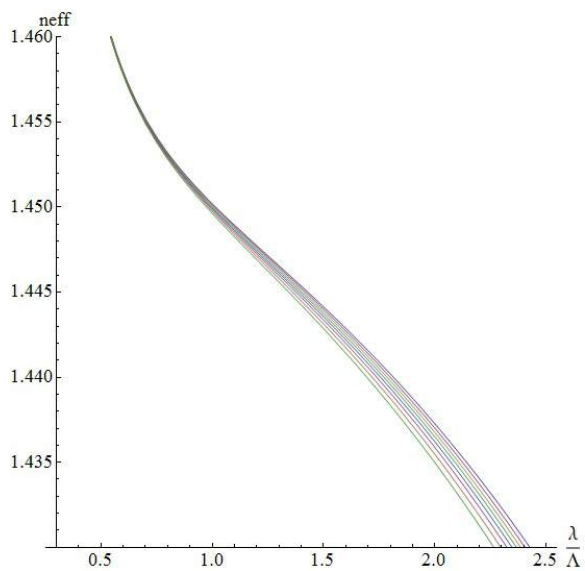

Figure 2.4: Effective index of the fundamental mode neff as a function of d/Λ

For $\lambda/\Lambda \leq 2$ and W ≥ 0.1 the expression 2.7 gives values of W which deviates less than 0.015 from the corrected values obtained from Eq. 2.3. Using the V parameter from 2.5 and the W parameter from 2.7, the effective index of

the fundamental mode n_{eff} can be obtained without the need for numerical computations. Figure 2.4 shows n_{eff} as a function of λ/Λ for d/Λ ranging from 0.2 to 0.8 in steps of 0.1, where the curves show the results in Eqs. 2.1, 2.3 , 2.5 and 2.7 with $a_{\text{eff}} = \Lambda/\sqrt{3}$. For $\lambda/\Lambda \leq 1.5$ and $W \geq 0.1$ the expressions of Eqs. 2.5 and 2.7 give values of n_{eff} which deviates less than 0.15% from the values obtained through vector FEM.

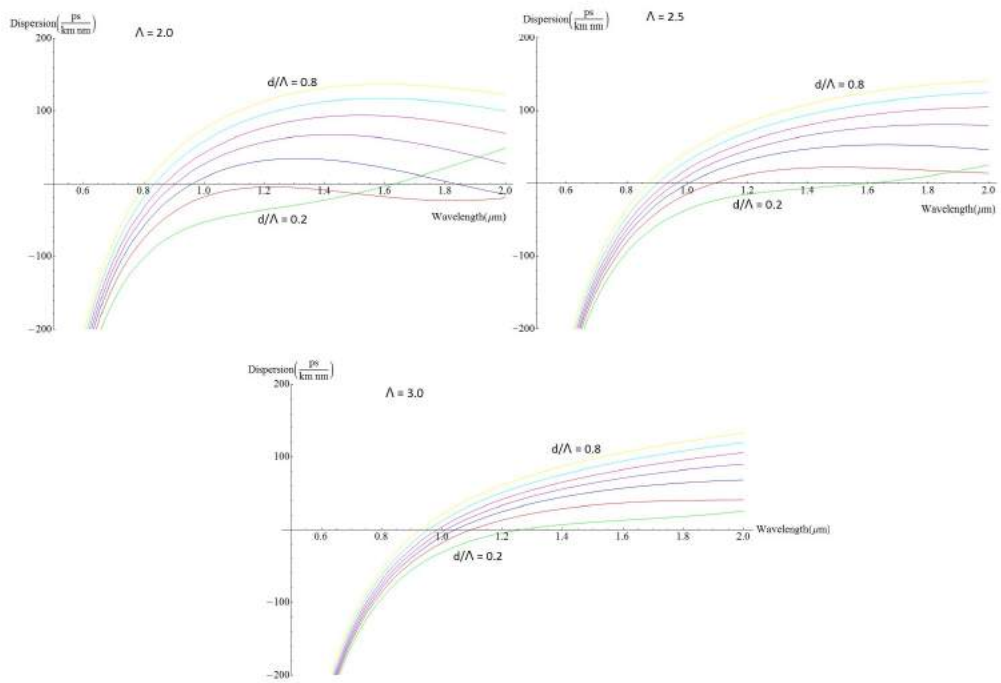

Figure 2.5: Chromatic dispersion as a function of wavelength for (a) $\Lambda = 2.0$ μm, (b) $\Lambda = 2.5$ μm, and (c) $\Lambda = 3.0$ μm. Curves, results of empirical relations; dashed curves, results of vector FEM.

Next, using the empirical relations of Eqs. 2.5 and 2.7 we calculate the chromatic dispersion in PCFs. In order to use universal data for the effective index of the fundamental mode neff, we assume that the waveguide contribution to the dispersion parameter D is independent of material dispersion D_m, 2.9 [49]

$$D = -\frac{\lambda}{c}\frac{d^2 n_{\text{eff}}}{d\lambda^2} + D_m, \tag{2.9}$$

where c is the light velocity in a vacuum and D_m is given by the Sellmeier relation. Figure 2.5 shows the dispersion parameter D as a function of wave-

length for d/Λ ranging from 0.2 to 0.8 in steps of 0.1, where the background index of silica is assumed to be 1.45, namely, $n_{\mathrm{co}} = 1.45$.

The results based on the empirical relations of Eqs. 2.5 and 2.7 agree well with the numerical results obtained by FEM . It is worth noting that, in Ref. [49], the chromatic dispersion of PCFs was calculated by using the Gloge formula [18] and V values, while, here, the expressions of Eqs. 2.5 and 2.7 are used for direct calculation of the chromatic dispersion. When we design a fiber, one of the most important parameters is to obtain a Single Mode Fiber (SMF), normally when the ratio d/Λ is less than 0.4, we have a single mode fiber. The ratio λ/Λ and d/Λ we can see in the figure 2.6

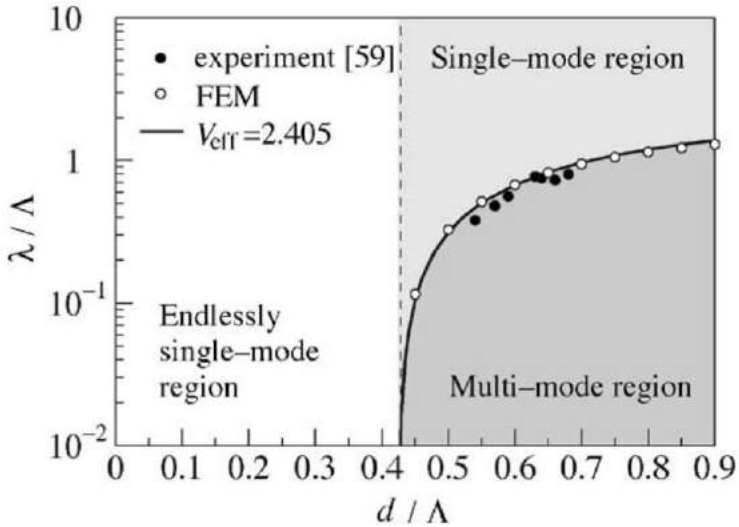

Figure 2.6: Relative cutoff wavelength λ/Λ as a function of relative hole diameter d/Λ. (Taken from reference [11])

2.4 Conclusion

In order to design a PCF, we used the empirical relations for both V parameter and W parameter of PCFs, wich only dependent on the air hole diameter and the hole pitch. We demonstrated the accuracy of these expressions with comparing the proposed empirical relations with the results of full-vector FEM. Through the empirical relations the fundamental properties of PCFs could be easily estimated without the need for numerical computations.

Chapter 3

Fabrication and Optimization of Special Large Mode Area Photonic Crystal Fibers [5]

3.1 Introduction

Large Mode Area Photonic Crystal Fibers (LMA PCFs) have specific waveguide properties due to the large area in their core. At the same time, it is very important that this kind of fibers maintain their operation in the fundamental mode. The development of LMA PCFs is important for a wide range of practical applications, in which high optical power is required. For applications where high optical power is transmitted, it is generally important to have this transmission without the influence of nonlinear effects that can appear in small core PCFs [29].

The core diameter in this kind of fibers can be defined as D=2Λ- d, which corresponds to the distance between opposite holes around the core. When the ratio d/Λ ≤0.4, the LMA PCF is endlessly single mode, meaning that the fiber transmits only one mode for any wavelength [52, 53]. LMA PCFs are often used for high power applications, because the nonlinear properties are drastically reduced.

Particularly, LMA PCFs are currently used in applications for high power delivery, such as laser machining and welding, as well as in high power lasers and amplifiers, providing significant advantages over traditional optical fiber [54]. The conventional fibers used in lasers and amplifiers are basically step index fibers whose cores are doped with rare elements (like Erbium or Ytterbium). These fibers are usually pumped only with single-mode laser,

and due to the limitation in their power, they are not suitable for high power applications.

This kind of fiber is very interesting, not only because it has a large mode field diameter (approximately 20 micrometers at a wavelength of 1550 nm), but also because it is a single mode fiber for any wavelength in which the silica material is transparent. There are many reports[55, 56] in the literature on the fabrication of such PCFs, and some of them have also low losses [57]. Matsui et al. [55] have proposed, for example, a LMA PCF; they reached a mode field diameter of more than 100 μm^2 in a double cladding structure. This fiber is also characterized with two distinct pitches (Λ), and air holes.

Although losses in this fiber are low, such fiber in double cladding [55] is a very complicated to fabricate. Reeves et al [40] have also investigated an LMA PCF with an effective area of 44 μm^2, but fabrication of their fibers has also proved to be very complicated.

3.2 First group of fabricated Large Mode Area Photonic Crystal Fibers

In 2013, we fabricated the first samples of LMA PCF. In the fabrication process we manufactured 4 different fibers from the same preform. The first one, which was called N1, was manufactured at a draw velocity of 15 m/min, the second fiber (N2) at a draw velocity of 16 m/min, the third fiber (N3) at a draw velocity of 17 m/min, and finally, the fourth fiber (N4) at a draw velocity of 18 m/min. In figure 3.1 we can see a transversal cut image of fiber N2, obtained using of an optical video microscope with a 40x objective. For this first group of LMA PCFs we made the following measurements:

- geometrical dimensions using an atomic force microscopy (AFM) (with the help of Dr. Sergio Calixto Carrera),
- numerical aperture (NA) and Gaussian mode field diameter (MFD),
- attenuation (or losses) in the fibers.

In table 3.1 we can see the geometrical parameters of the 4 fibers as diameters of the air-holes (d), pitch (Λ) or distance between the centers of the holes, external diameter of the fiber $D_{ext.}$, diameter of the core D_{core}, and ratio d/Λ.

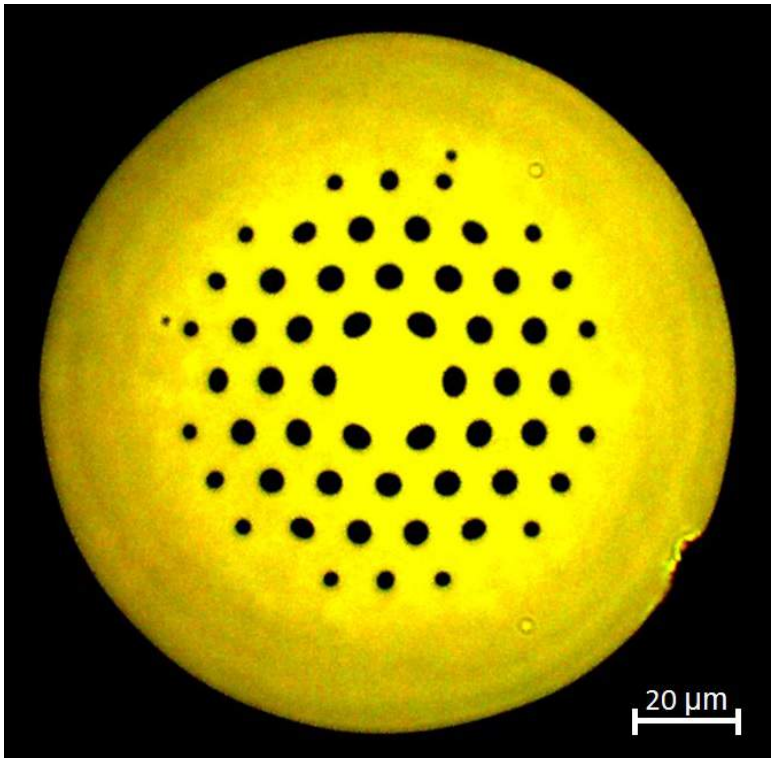

Figure 3.1: Transversal cut image of LMA PCF.

The losses measured for these four fibers are presented in figure 3.2. It is important to point out that the losses of fibers N1 and N2 are very high. It is seen in the figure that fibers N3 and N4 have lower losses, with fiber N4 showing losses of approximately 15-25 dB/km in a wavelength range between 1500 and 1700 nm.

Based on the results obtained, shown in table 3.2, it is possible to calculate the dispersion dependencies for the four fibers; these curves are shown in figure 3.3.

We can see in figure 3.1 that the holes are irregular in the structure; the outermost layer has small holes, which normally happens due to the fact that heating effects the external layer more. Also, it is possible to see that the first layer around the core has deformed holes, while the second and third layers have more or less regular holes. This kind of deformation and irregularity possibly affects the results of attenuation (loss) and dispersion values, but at the same time, as it was shown in [57], this kind of deformed

fiber	d (μm)	Λ (μm)	D ext. (μm)	D core (μm)	d/Λ
N1	3.516	10.664	122.2	21.79	0.33
N2	3.5156	10.313	123.2	20.391	0.34
N3	4.1403	10.312	122.8	20.156	0.40
N4	4.4533	10.428	120.2	19.453	0.43

Table 3.1: Geometrical parameters of the fabricated LMA PCFs.

fibers has found application for optical sensing [58].

3.3 Optimization of Large Mode Area Photonic Crystal Fibers

After finishing the previous work, it was decided to fabricate LMA PCFs with more regular structure, regardless of the technical problems still present in the drawing tower. After a lot of attempts and efforts, we managed to fabricate a group of LMA PCFs with regular structure. Unlike the fiber made in the first group, which has 4 layers around the core without the edges of the hexagon, this design contains three complete layers around the core. The design of the preform is presented in figure 3.4a.

The fabricated capillaries were stacked like in the preform of the first group (see figure 3.4b); then, just to finish the preform fabrication before the drawing process, it was necessary to put these stacked capillaries into another tube of 16x20 mm of diameter (inner and outer diameters respectively).

During the drawing of this preform, we fabricated 5 different fibers. We used different pressures into the holes for each fiber in order to obtain different hole diameters d and pitch Λ. For the first fiber, N5, the pressure was 14 mBar, and the drawing speed was about 25-26 m/min; the second fiber, N6, was fabricated with a pressure of 15 mBar, and the drawing speed was 26-27 m/min; the third fiber, N7, was fabricated with a pressure of 16 mBar and a drawing speed of 27-28 m/min; the fourth fiber, N7, was fabricated with a pressure of 18 mBar, and the drawing speed was 28-29 m/min; finally, the last fiber of this group, N9, was fabricated with a pressure of 22 mBar and a drawing speed of 29-30 m/min. In the table 3.2, it is possible to see the parameters of the 5 fabricated fibers.

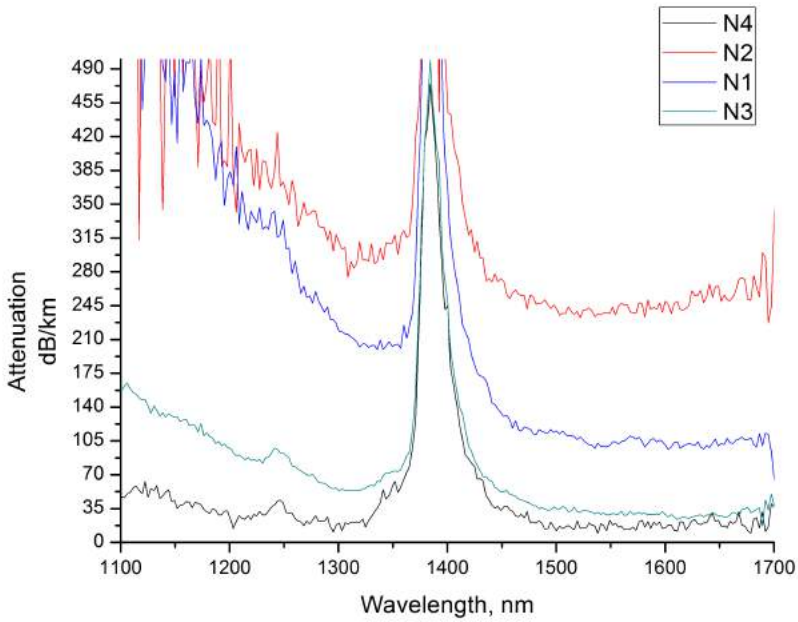

Figure 3.2: Losses for the four fabricated LMA PCFs

The transversal cut images obtained using an optical video microscope for the 5 fabricated fibers are shown in figure 3.5. In this figure, it is possible to see that increasing pressure increases the size of hole diameters, but the most important thing is that, in comparison with the fibers fabricated in the first group, the regularity of the hole diameters and the pitch is quite constant everywhere; independently of the pressure applied to the preform, the holes are regular everywhere. The difference between fibers N5, N6 and N7 is difficult to appreciate visually, but the difference between fibers N7, N8 and N9 is visible, because the hole pressure difference in this case is higher. All these pictures were obtained using a National DC-163 optical microscope, and they were taken with a 40x objective.

To get more precise geometrical parameters of the fibers, we made the measurements using an Atomic Force Microscope (AFM), and we obtained different values of diameter (d), pitch (Λ), core diameter, external diameter of the fiber and ratio d/Λ for each fiber. The average of those values is presented in table 3.3.

In table 3.3 it is possible to see how the diameters of the capillaries grow as

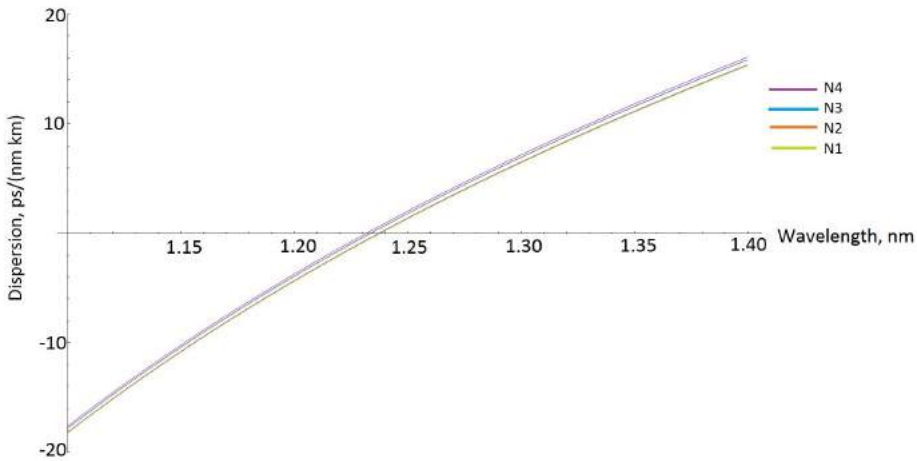

Figure 3.3: Dispersion for the four fabricated LMA PCFs

Fiber	T (^oC)	preform feed (mm/min)	average drawing speed (m/min)	pressure (mBar)
N5	1900	1.2	25.5	14
N6	1900	1.2	26.5	15
N7	1900	1.2	27.5	16
N8	1900	1.2	28.5	18
N9	1900	1.2	29.5	22

Table 3.2: Drawing parameters for the 5 fabricated fibers.

pressure rises; pitch also increases, but not as much as the diameters. The external diameter of these fibers is practically the same, and it is less than 125 μm; normally, these values shift between 122.5 and 124 μm. We chose to fabricate fibers with an outside diameter of a little less than 125 μm, just because if a fiber has an outside diameter slightly bigger than 125 μm, it is impossible to place the fiber into the connectors when optical measurements are made.

For attenuation (or loss) measurements we use the cutback method. The instrument used for our measurements was an Anritsu AQ-6315A Optical Spectrum Analyzer (OSA), along with a white light source.

The results of loss measurements of the 5 fabricated fibers are presented in the graphic of the figure 3.6. It is clear from the figure that the fiber N9 has

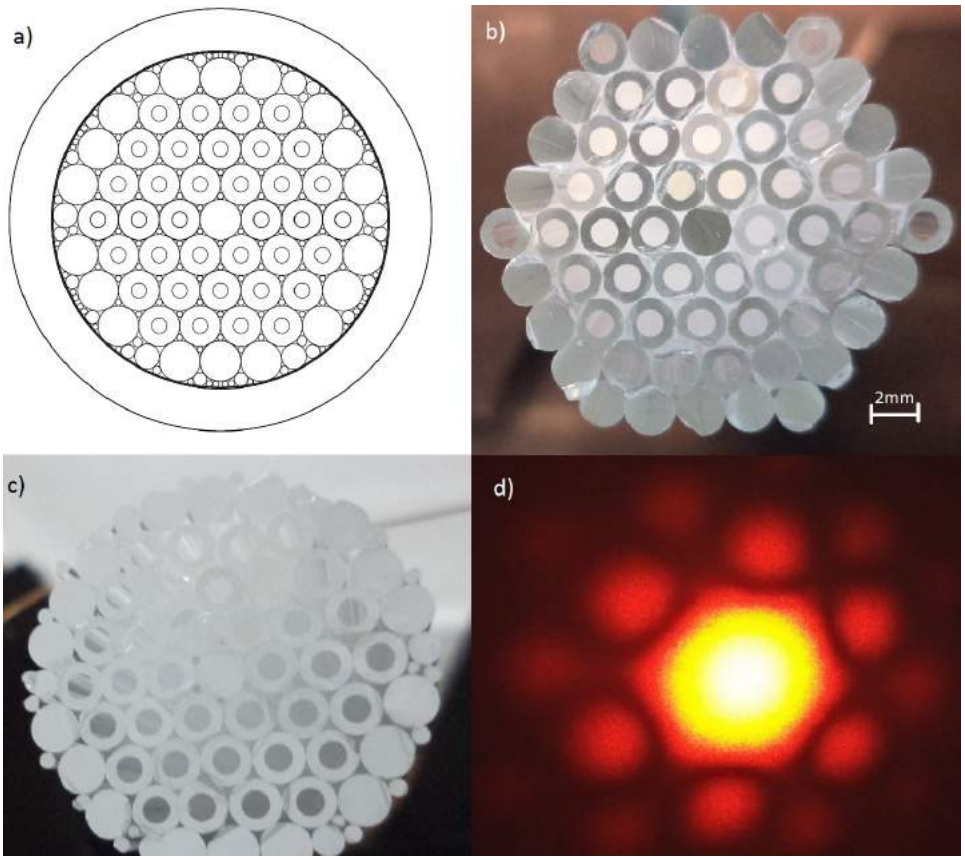

Figure 3.4: a) Design of the proposed LMA PCF, b) hexagonal arrangement of capillaries, c) capillaries and rods ready to be inserted into a tube to form a preform, d) signal obtained at the output of the single-mode fiber obtained with a He-Ne laser.

the lowest attenuation; the attenuation of this fiber is about 9-10 dB/km in the range of wavelengths between 1600 and 1650 nm. The fiber with the second lowest attenuation is fiber N6, with an attenuation of 10-15 dB/km at wavelengths between 1550-1750 nm. The next fiber on the list is fiber N5, with an attenuation of 15-18 dB/km in the same range of wavelengths as the previous fiber, and it has lower attenuation than N7 in the range of wavelengths from 1000 to 1300 nm.Fiber N7 has an attenuation of 26-30 dB/km in the wavelength range from 1550-1750 nm. Attenuation in fiber N8 is the highest, and is about 40-45 dB/km at 1550-1750 nm (this is the most important range of wavelength for telecommunications). The water peaks for all these fibers were very high, and it means that the preform absorbed a lot of OH groups from our laboratory atmosphere.

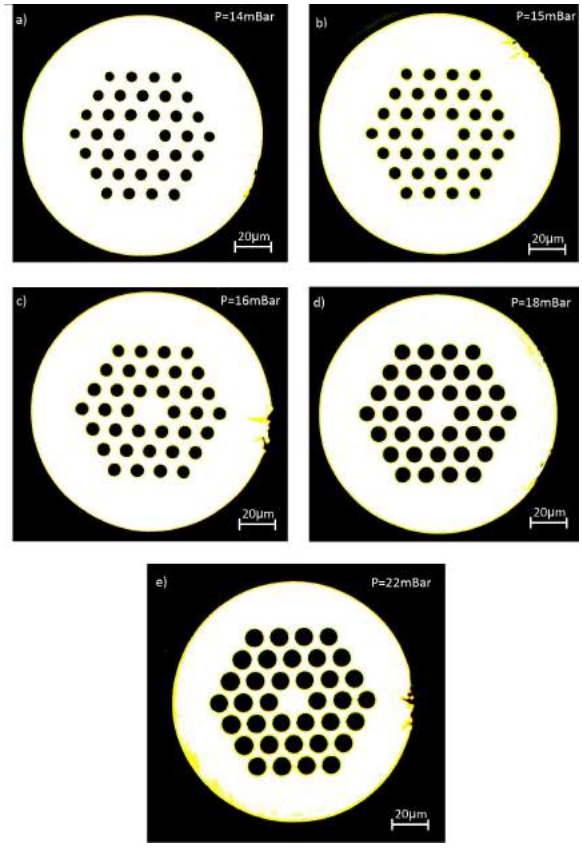

Figure 3.5: Large mode area PCFs, fabricated for different pressures: a)14 mBar, b)15 mBar, c) 16 mBar, d)18 mBar, e)22 mBar

On the basis of the geometrical parameters presented in table 3.3, it is possible to calculate dispersion curves for the five fibers, these curves are shown in figure 3.7. In this figure, it is possible to see that the five curves have the point of zero dispersion very closely, which means that for those values of pitch, hole diameter does not have a large influence on the Zero Dispersion Wavelength (ZDW). The value of ZDW for fiber N5 is 1.24602 nm, for N6 is 1.24459, for N7 is 1.24299, for N8 is 1.24092 and for N9 is 1.23928.

Fiber	Presure (mBar)	Diameter d(μm)	Pitch Λ (μm)	d core (μm)	d/Λ	d ext. (μm)
N5	14	4.68	12.63	24.80	0.37	122.5
N6	15	5.03	12.60	24.70	0.40	123.2
N7	16	6.67	13.33	26.06	0.50	123.0
N8	18	7.39	13.40	26.10	0.55	122.9
N9	22	8.85	13.95	27.02	0.63	123.8

Table 3.3: Geometrical values of the fabricated LMA PCFs.

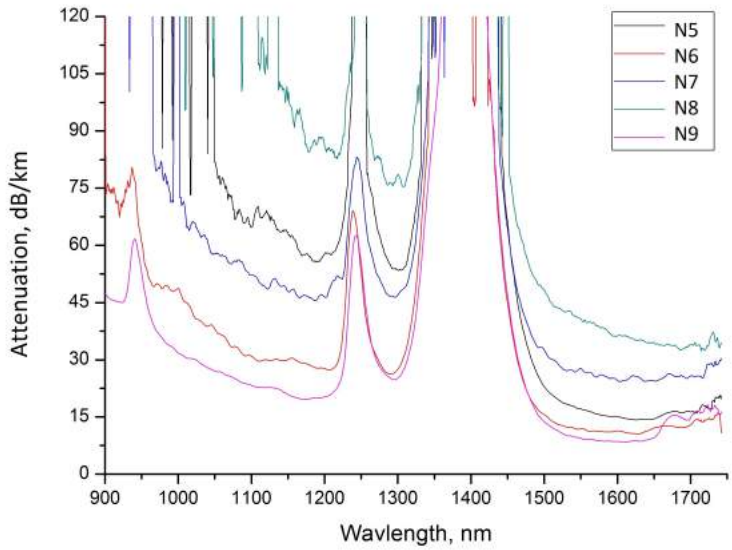

Figure 3.6: Graphic of losses for 5 fabricated LMA PCFs.

3.4 Conclusion

The quality and the geometrical characteristics of the fabricated fibers for the last group (N5, N6, N7, N8 and N9) are very similar to those of the NKT Photonics LMA PCF (LMA-20) [59]. In the above mentioned figures, we can see that the structure of the holes is very uniform, and also, we obtained very low attenuation in some of these fibers.

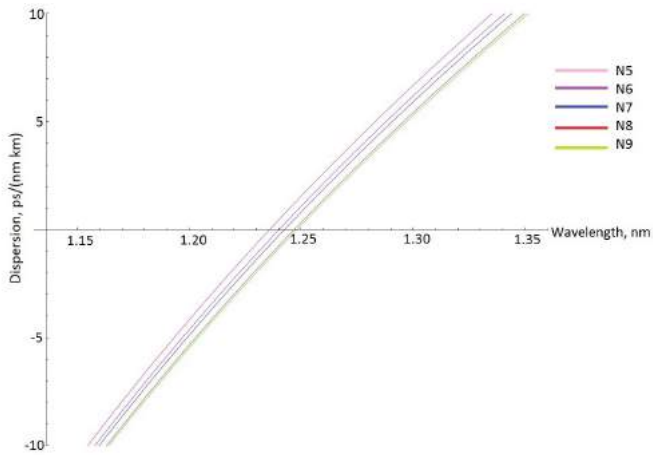

Figure 3.7: Dispersion curves for 5 fabricated fibers.

Chapter 4

Design and fabrication of High Nonlinearity Photonic Crystal Fibers

4.1 Introduction

This kind of PCF (HNL PCF) was designed to obtain high nonlinearity, namely, for the supercontinuum generation, and it must have a small core area, which means a small core diameter, and therefore, a small air-hole structure around this core. The sizes of the pitch (Λ) and the hole diameter (d) must also be very small, at least in 4 and 6 times less than in LMA PCFs. This kind of fibers is much more difficult to fabricate, because of such small air-hole diameters, which can be of about 1 μm or less. That is why the cost of this kind of fibers in a world market is very high, of about 1300 USD per meter.

This chapter is organized as follows. First we made the dispersion simulations with a special software based on an empirical method, and the optimization HNL dispersion curves were made to obtain the flattened HNL PCFs, which means they have a dispersion near to zero in a wide range of wavelengths. After the simulation, we analyzed the already fabricated fibers that exist commercially just to compare the parameters we obtained with parameters of fabricated fibers from the company NKT photonics. The third part reports on the design and fabrication of 3-ring and 6-ring HNL PCFs.

4.2 Simulation for regular air-hole structure

As we said before, our theoretical simulation is based on an empirical method that is presented in reference [10]. This method was designed to obtain the HNL PCF dispersion curves from only two parameters of a regular air-hole structure around the core of the PCF: the pitch (Λ), or distance between the centers of the holes, and the diameter (d) of the capillaries, or the diameter of the holes, which has the same value along all the structure (It is called a regular structure). In the simulation, we tried to obtain the minimum possible dispersion values within a large range of wavelengths. It means the modeling was made to obtain an optimized value of pitch (Λ) and diameter (d), even without analyzing whether the construction of this fiber is technologically possible to fabricate or not.

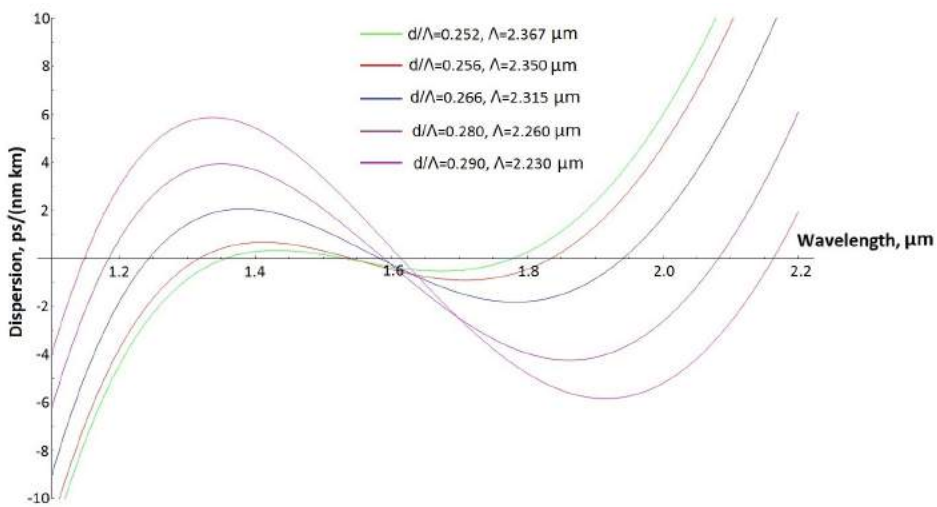

Figure 4.1: 5 curves of optimized flattened dispersion for HNL PCFs

In chapter I (Figure 1.5), it is possible to see that the best relationship for the HNL PCF is for the ratio d/Λ=0.3 and for Λ=2. Within these parameters, the fiber has a little negative dispersion; for Λ=2.5, the fiber has a little positive dispersion. In Figure 4.1, it is possible to see 5 curves of optimized flattened dispersion.

Theoretically, we also found a second range of wavelengths, which includes a little part of visible range; in this second range of optimization, we have a flattened region between 0.65 and 0.85 μm, and in figure 4.2, it is possible

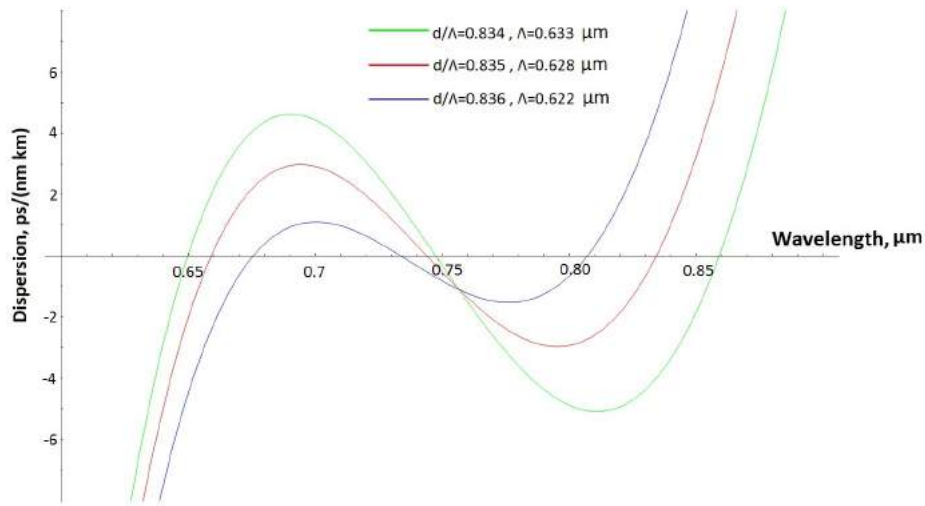

Figure 4.2: 3 curves of flattened dispersion between 0.65 and 0.9 μm.

to see three curves of flattened dispersion within this range of wavelengths.

The values from figures 4.1 and 4.2 are also shown in table 4.1.

From figure 4.1 and 4.2, and also from table 4.1, we can conclude the following:

- The range of wavelengths for the first group is between 1.1-2.2 μm.
- The pitch for the first group is around 2.2-2.3 μm, and for the second group is around 0.62-0.63 μm; in this case, it is easier to fabricate fibers from the first group.

Groups	Ratio d/Λ	Pitch Λ μm	Range of λ (μm)	Values of Dispersion (ps/nm/km)
	0.252	2.367	1.35-1.80	$\pm$0.5
First group	0.256	2.350	1.30-1.85	$\pm$1
	0.266	2.315	1.20-2.00	$\pm$2
1.1-1.2 μm	0.280	2.260	1.15-2.15	$\pm$4
	0.290	2.230	1.05-2.25	$\pm$6
Second group	0.834	0.633	0.64-0.87	$\pm$5
	0.835	0.628	0.65-0.85	$\pm$3
0.7-0.9 μm	0.836	0.622	0.67-0.81	$\pm$1

Table 4.1: Results of optimization for two wavelength ranges of flattened dispersion.

Technologically, it is easier to fabricate fibers from the first group, since the second group of fibers has very small holes that are not possible to fabricate with the equipment that we have.

4.3 Some theories and simulations for the optimization of flattened dispersion in photonic crystal fibers

In recent years, some simulations and designs of HNL PCFs with flattened dispersion have been proposed and reported to obtain the minimum possible dispersion in the maximum range of wavelengths. In these proposals, some authors designed an irregular structure of holes, which have different air-hole diameters in the different layers, but with the same pitch (Λ) in all the structure. As we can see in section 4.2, the design of the flattened dispersion PCF is limited when we have regular hole diameters. Then, when we try to minimize the values of dispersion, the range of wavelengths becomes increasingly narrow.

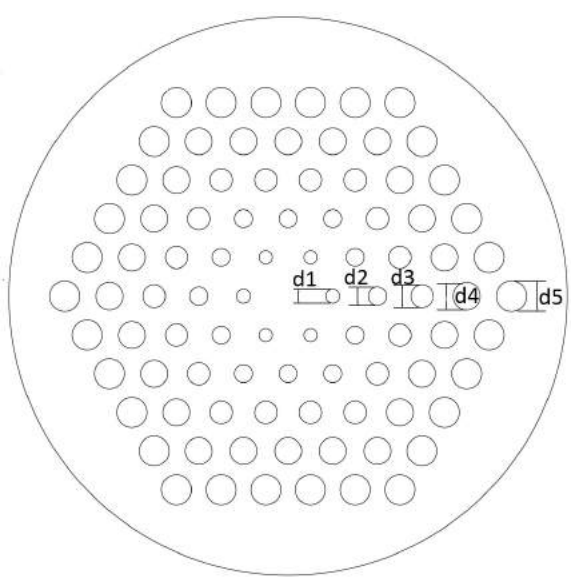

Figure 4.3: Design of HNL PCF with ultra-flattened dispersion and with 5 different air-hole diameters.

Based on the design with different diameter of the holes in each ring, it is

possible to obtain, in a wide range of wavelength, dispersion that varies only in the range of ±1 ps/(km nm), or less than this value. Practically in all the design cases, the first ring around the core (the innermost ring) has the smallest hole diameter of the structure; then, in each next air-hole ring, the hole diameter increases, and the biggest air-hole diameter is in the last ring (the outermost ring). In figure 4.3, it is possible to see a 5-ring PCF as an example of the above explanation.

In their article, K. Saitoh and M. Koshiba [57] proposed an HNL PCF structure with flattened dispersion in the range of ± 0.4 ps/(km nm) from 1250 to 1700 nm with the following parameters: Λ=1.58 μm, d1/Λ=0.31, d2/Λ=0.45, d3/Λ=0.55, d4/Λ=0.63 and d5/Λ=0.95.

F. Poli, A. Cucinotta, et al [60] reported an HNL PCF design in which they only changed the air-hole diameters in three first air-hole rings as follows: Λ= 0.9 μm, d1/Λ=0.42, d2/Λ=0.86, d3/Λ=0.93. The relative air-hole diameters d4/Λ and d5/Λ have the same value, 0.9. For this calculation they obtained a dispersion in the range of ±0.5 ps/(nm km) from 1425 to 1600 nm.

In reference [61], they reported a design in which the fiber has only four air-hole rings with the following parameters: Λ= 1.618 μm, d1/Λ=0.31, d2/Λ=0.43, d3/Λ and d4/Λ have the same value of 0.54, obtaining a dispersion of ±0.5 ps/(km nm) for wavelengths from 1210 nm to 1780 nm.

	Saitoh	Poli	Barrientos	El-Mosalmy	Hammed (PSO)	Hammed (CFO)
Λ(μm)	1.58	0.90	1.62	1.782	1.833	1.738
d1/Λ	0.31	0.42	0.31	0.290	0.303	0.311
d2/Λ	0.45	0.86	0.43	0.365	0.338	0.372
d3/Λ	0.55	0.93	0.54	0.409	0.465	0.524
d4/Λ	0.63	0.90	0.54	0.569	0.436	0.423
d5/Λ	0.95	0.90	-	0.569	0.719	0.689
dispersion (ps/(km nm))	±0.4	±0.5	±0.5	±0.27	±0.5	±0.35
Range of λ (nm)	1250 1600	1425 1600	1210 1780	1300 1670	1250 1600	1250 1600

Table 4.2: Data for comparison of geometrical parameters for irregular cladding from some published works.

Dalia D. El-Mosalmy, M.F.O. Hameed et al. reported in [62] about their

modeling results on a base of neural network based on an optimization approach, in which they got the following parameters: Λ= 1.7825 μm, d1/Λ=0.29, d2/Λ=0.3646, d3/Λ=0.4095, d4/Λ=0.5698 and d5/Λ=0.5698, obtaining a dispersion of $\pm$0.27 ps/(km nm) for wavelengths from 1300 nm to 1670.

Finally, in one of the latest works published on flattened dispersion optimization, Mohamed Farhat o. Hammeed, et al. [63] used two optimization methods, the particle swarm optimization (PSO) and the Central force optimization (CFO). In table 4.2, it is possible to see the proposed geometrical parameters of above mentioned authors.

It is possible to see in table 4.2 that the value of pitch must have an average of about 1.70 μm, d1/Λ of about 0.30, d2/Λ of about 0.39, d3/Λ of about 0.49, d4/Λ of about 0.73 and d5/Λ of about 0.73.

In practice, nobody has yet fabricated this kind of fibers with different air-hole diameters in the structure, due to the fact that for these cases, it is necessary to put different values of pressure into each air-hole ring, but this problem has not been solved yet.

4.4 NKT Photonics Commercial Photonic Crystal fibers

NKT Photonics is the leading supplier of high performance fiber lasers and photonic crystal fibers. Their products include a wide range of specialty fibers. NKT Photonics has its headquarters in Denmark, with sales and service worldwide. They fabricate Large mode Area PCF, High Nonlinearity PCF, Hollow core PCF and others. Optimized for supercontinuum generation and nonlinear wavelength conversion, their nonlinear photonic crystal fibers offer a combination of tailored dispersion profile and a very high nonlinear coefficient. As an example of these fibers, we particularly want to analyze a NKT photonics HNL PCF, the SC.05.1040 [64], which has a core diameter of about 5 μm, and has the wavelength of zero dispersion at 1040 nm. The fiber is used for supercontinuum generation. In figure 4.4, it is possible to see a photograph of a transversal cut of the HNL PCF SC.05.1040 obtained with a National DC-163 optical microscope using an optical objective of x40. It is seen that the fiber has a perfect regular structure with 5 complete air-hole layers around the core.

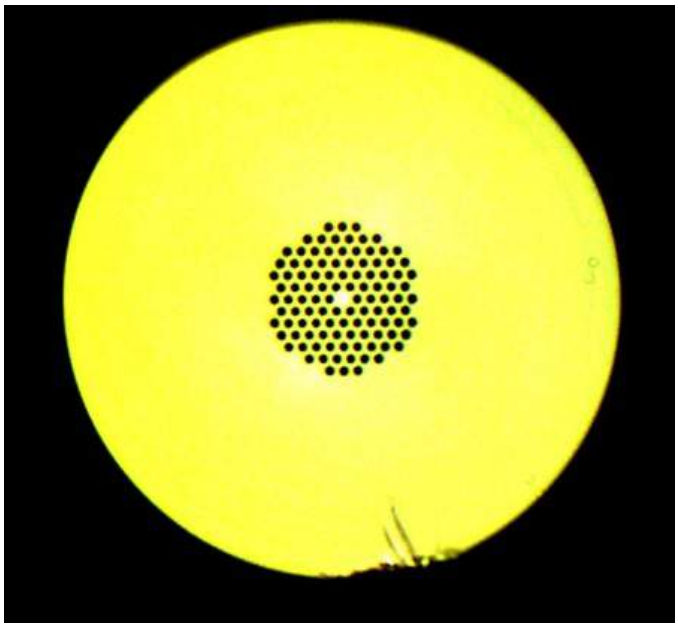

Figure 4.4: Transversal view of NKT Photonics HNL PCF SC.05.1040

NKT Photonics fabricate NHL PCF for different ZDW, for specific lasers, for example. Fiber SC.05.1040 is fabricated to be used with Nd3+ microchip lasers, to obtain a compact ultra-bright supercontinuum source. It works in combination with a laser that delivers pulses of 1 ns, with few tens of milliwatts of average power at a wavelength of 1064 nm.

We made the measurement of pitch Λ, the core diameter d_{core} and the air-hole diameter d of the SC.05.1040 fiber using a scanning atomic force microscope, and we obtained that d=1.4648 μm, Λ=3.17 μm, and d_{core}=4.87 μm.

Then, we calculated the dispersion curve using these parameters of pitch and diameter. The curve crosses the axis of zero dispersion at the wavelength of 1037.43 nm, which is very near the zero dispersion nominal value for this fiber, 1040 nm $\pm$10nm. This fact shows us that the empirical method that we used is totally reliable.

Also, we can see from reference [64] that the nominal diameter of the core of this fiber is 4.8 μm $\pm$2 μm, and from our measurements, we obtained 4.87 μm, which implies we made right the measurements of the geometrical parameters of the fiber.

Another example of NKT Photonics HNL PCF is NL-1050-NEG-1 [65], which has negative dispersion with a value of -10 ps/(nm km) within a range of 1000-1100 nm of wavelength. Unfortunately, in their tables, they do not present any information about the geometrical parameters of this HNL PCF.

4.5 PCF fabrication

The process of HNL PCF fabrication is very long, with a lot of possible failures. In this part, we would like to talk about the fabrication of fibers with only good optical properties. The fibers have both regular and irregular air-hole structures. First, we designed a 3 ring HNL PCF, on the basis of results obtained in [66]. The results show that sometimes it is not necessary to fabricate the PCFs with a lot of air-hole rings. So, in the first step, we fabricated HNL PCFs with 3 air-hole rings in the cladding. In the second part, we decided to fabricate a more complex cladding structure, with 6 rings of air-holes around the core.

4.5.1 3 ring PCF

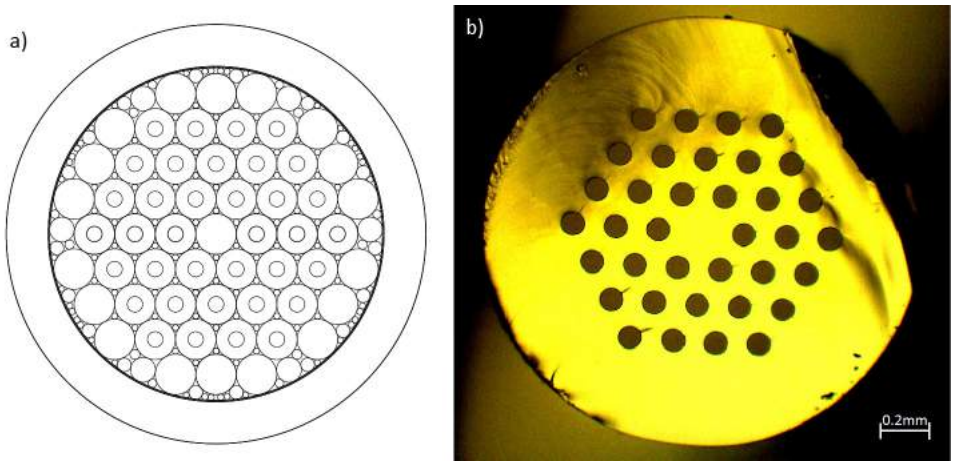

Figure 4.5: a) Stack design of 3 ring preform, b) optical microscope image of 3 ring cane cross section.

The first set of fabricated PCFs had 3 air-hole rings surrounding a central core. The stack design is shown in figure 4.5(a). The stack was drawn into

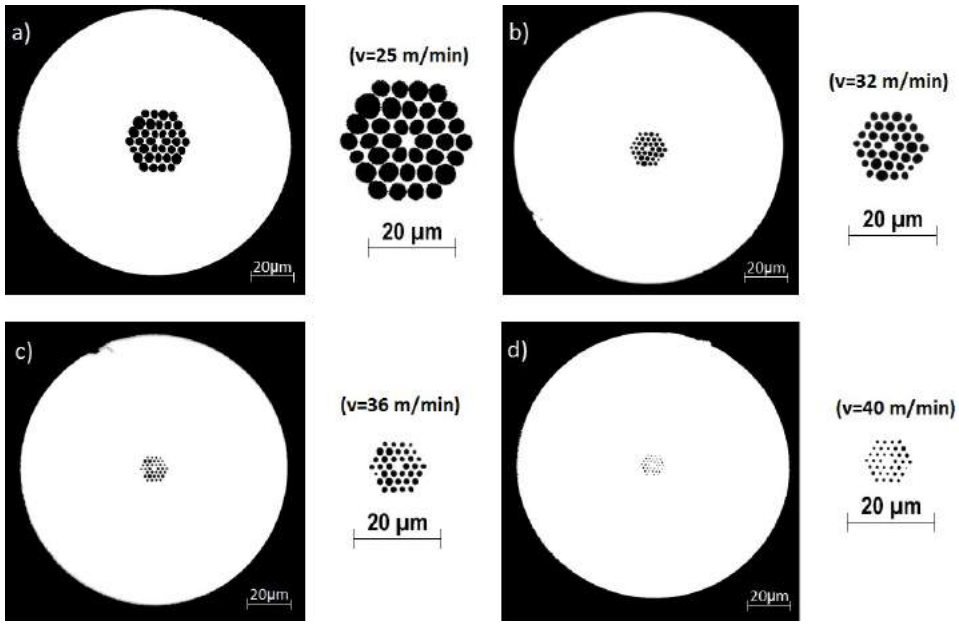

Figure 4.6: Optical microscope images of 4 fiber cross section: a)NL1, b)NL2, c)NL3 and d)NL4.

approximately 10 canes with an outer diameter of 1.8-1.85 mm. An optical microscope image of a cane cross section is shown in figure 4.5(b).

For practical reasons, we gave the name of NL + number for each fiber just to identify them more easily.

To draw fiber, a cane was inserted into a jacketing tube with 1.89 mm inner diameter (ID) and 12 mm outer diameter (OD). During the draw, a pressure is applied to the holes; for the two first fibers, pressure was held constant at 100 mBar. The draw rate was set to yield a fiber OD 123.5 μm, and the temperature was 1950 °C. The optical microscope images of these two fibers cross section are shown in figure 4.6 (a) and (d). Other two fibers were drawn from another preform to obtain a result between the two previous fibers. The pressure was 100 mBar. The draw rate was also set to give a fiber OD 123.5 μm with a constant temperature of 1950 °C. The optical microscope images of these two fibers cross section are shown in figure 4.6 (b) and (c).

These 4 first fibers were fabricated with a constant pressure, and basically we changed only the velocity of drawing. It is clear from the results that when the velocity of drawing is higher, the obtained structure is smaller, the

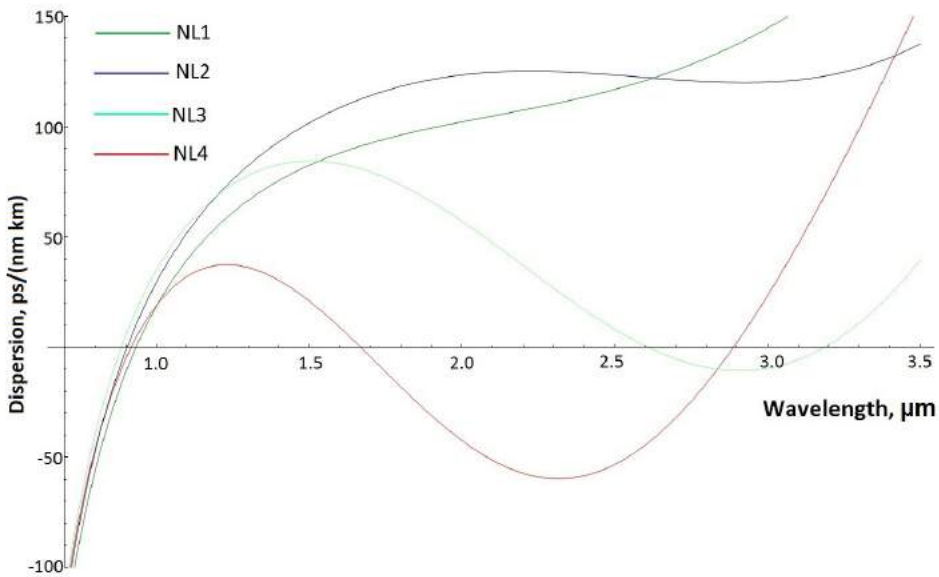

Figure 4.7: Graphic of dispersion for the first group of 4 fabricated fibers, for feed rate changes

air-hole diameter is smaller, and the pitch also is smaller, and therefore, the relative hole diameter d/Λ ratio is smaller; only the core diameter is bigger. All the geometrical parameters for this first group of fibers are shown in table 4.3.

Fiber No.	Velocity of drawing (m/min)	P (mBar)	T °C	diameter (μm)	Λ (μm)	d core (μm)	Ratio d/Λ
NL1	25	100	1950	3.628	4.219	2.42	0.86
NL2	32	100	1950	1.735	2.501	2.52	0.69
NL3	36	100	1950	1.134	2.025	2.83	0.56
NL4	40	100	1950	0.766	1.805	3.09	0.43

Table 4.3: Fabrication parameters and obtained geometrical parameters of first group of HNL PCFs.

Using the geometrical parameters presented in table 4.3, we calculated the dispersion curves for these four fibers. The curves are shown in figure 4.7; it is possible to see here that only two curves cross the axis in 3 points (NL3 and NL4), which means that they have 3 points of zero dispersion at different wavelengths, while the other 2 fibers (NL1 and NL2) only have one point of zero dispersion, which is near 0.9 μm.

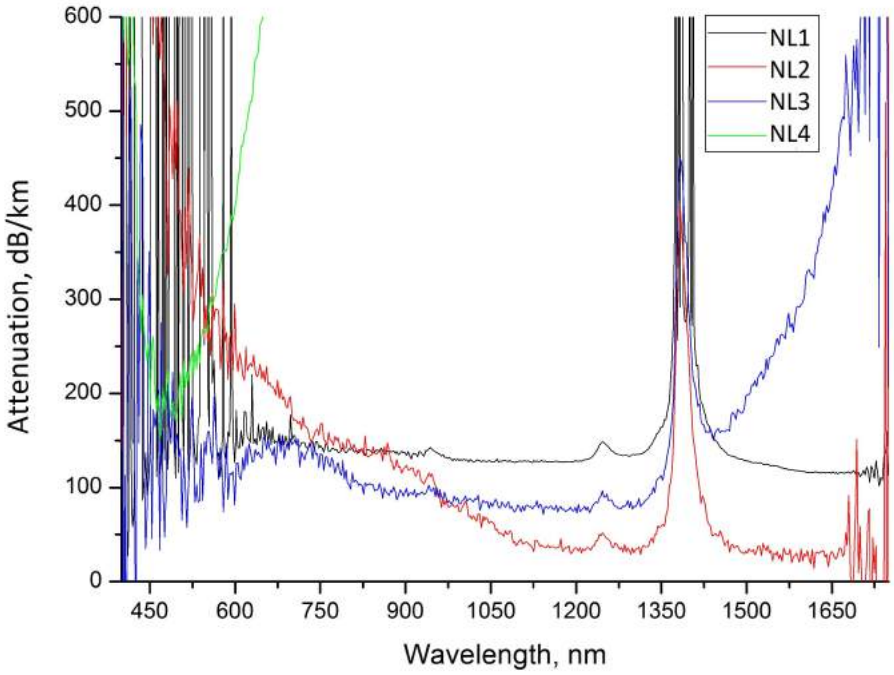

Figure 4.8: Attenuation distributions for the first group of 3 ring fabricated fibers.

In figure 4.8, we show the attenuation distributions for the first group of fibers, which include attenuation curves for 4 fabricated fibers with different drawing velocities. It is clear from the graphic that the best one from the point of view of attenuation (losses) is fiber NL2, which has losses of about 20-25 dB/km in the range of wavelengths between 1500 an 1650 nm. It is difficult to decide which fiber is the next better one, because NL3 has lower attenuation in the range of wavelengths between 700 and 1300 nm (about 70-80 dB/km) than NL1 (about 130-140 dB/km in the same range).

Meanwhile, for the range of wavelengths between 1500 and 1650 nm the NL1 fiber has lower attenuation (losses) than the NL3 fiber (which rapidly increases at the higher wavelength). The worst fiber from the point of view of attenuation, is the NL4 fiber. This fiber transmits light only between 450 nm and 650 nm (in the visible wavelength range), with a lower attenuation at about 500 nm (the attenuation at this point is 200 dB/km).

Then, we decided to fabricate another group of fibers, but in this process,

we did not change the drawing velocity, keeping it constant at 40 m/min. In the process, pressure into the holes was varied: for fiber NL5, pressure was 108 mBar, for NL6 it was 110 mBar, and for NL7 it was 115 mBar.

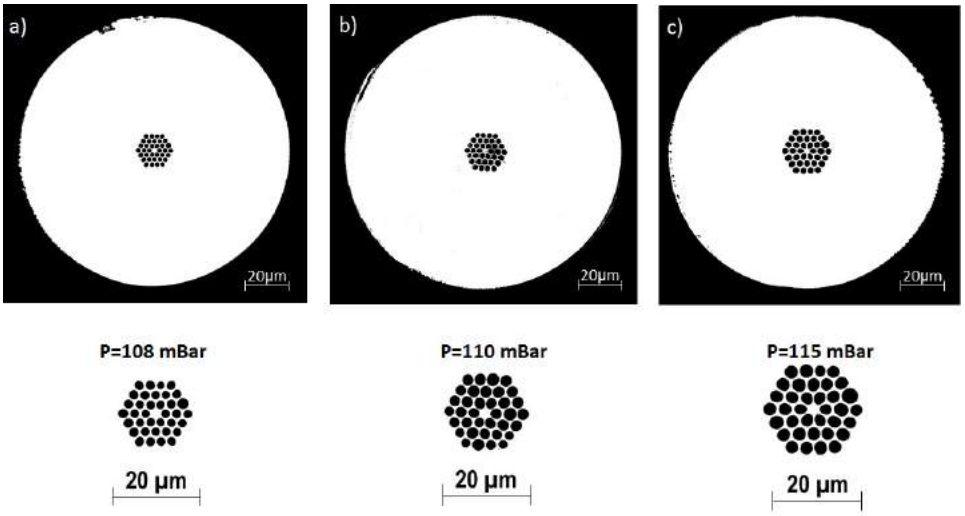

Figure 4.9: Optical microscope cross section images of three fibers: a) NL5 (P=108 mBar), b) NL6 (P=110 mBar), c) NL7 (P=115 mBar).

Temperature was constant for all the fibers, and was 1950 °C, and the draw rate was also set to yield a fiber OD of 123.5 μm. The optical microscope cross section images of these three fibers are shown in figure 4.9(a), 4.9(b) and 4.9(c). These three fibers were fabricated with constant drawing velocity and constant temperature; basically, we only changed the applied pressure to the preform from 108 to 115 mBar. It is clear from the figure 4.9 that when more pressure is applied to the preform, the obtained pitch and the air-hole diameters are bigger; therefore, d/Λ ratio is bigger. All geometrical parameters for this second group of fibers are shown in table 4.4.

Fiber No.	Velocity of drawing (m/min)	P (mBar)	T °C	diameter (μm)	Λ (μm)	d core (μm)	Ratio d/Λ
NL5	40	108	1950	1.911	2.419	2.628	0.79
NL6	40	110	1950	2.466	2.864	3.050	0.86
NL7	40	115	1950	2.738	3.227	3.844	0.84

Table 4.4: Fabrication parameters and geometrical parameters obtained for the second group of fibers.

On the basis of the geometrical parameters obtained for the second group of the fibers, we calculated dispersion curves for these 3 fibers. The curves for this second group of fibers are shown in figure 4.10, and in this figure it is possible to see that all the lines cross the zero dispersion axis only once, and their wavelengths of zero dispersion are between 0.8 and 1 μm.

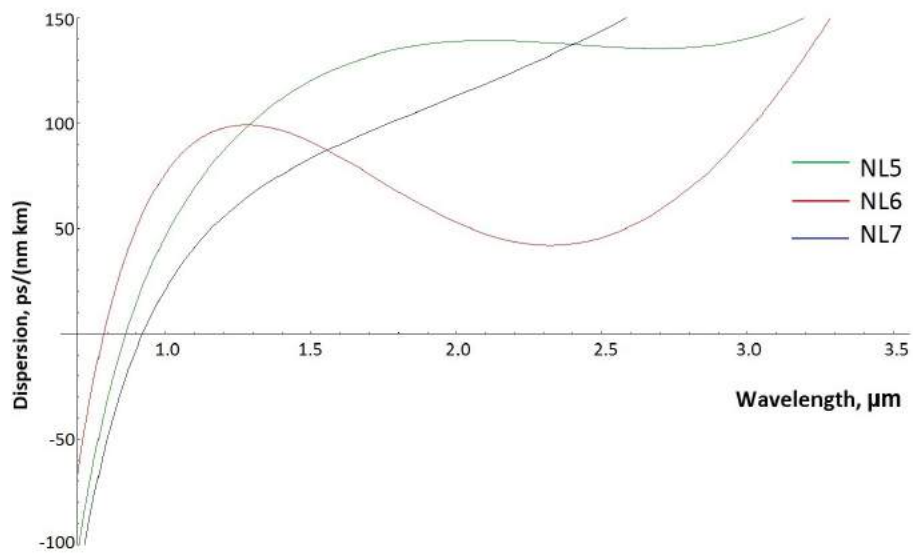

Figure 4.10: Dispersion curves for the second group of fabricated fibers, while pressure changes

We also made the attenuation measurement for the three fibers of the second group. This attenuation graphics are shown in figure 4.11. From the point of view of attenuation, the best fiber is NL5, with a particular difference in the range of visible wavelength, but now, we will analyze the region of low attenuation, 1500-1650 nm. For this range of wavelength, the NL5 fiber has an attenuation of about 15-30 dB/km, while the NL7 fiber has an attenuation of about 25-40 dB/km, and the NL6 fiber of about 35-50 dB/km. We can conclude from the figure that the worst fiber in the wavelength range between 600-1350 is the NL6, with an attenuation of 200-400 dB/km.

For the third and the last group of 3 ring fibers, we fabricated only two fibers, and in this case, we only changed the temperature; drawing velocity was constant at 41 m/min, and pressure also was constant at 115 mBar for both fibers. Temperature was 1950 °C for the NL8 fiber, and 1955 °C for the NL9 fiber. They were fabricated from the same preform on the same day. The draw rate was set to give the fiber an OD of 123.5 μm for all fibers.

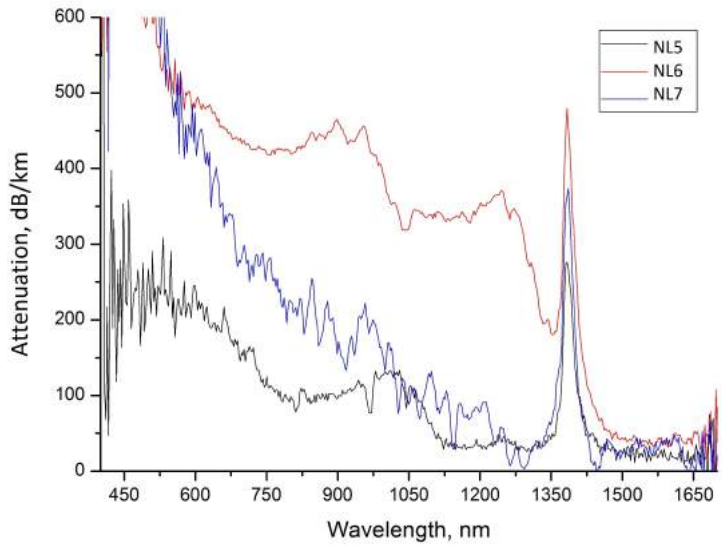

Figure 4.11: Attenuation graphics for the second group of fabricated 3 ring fibers

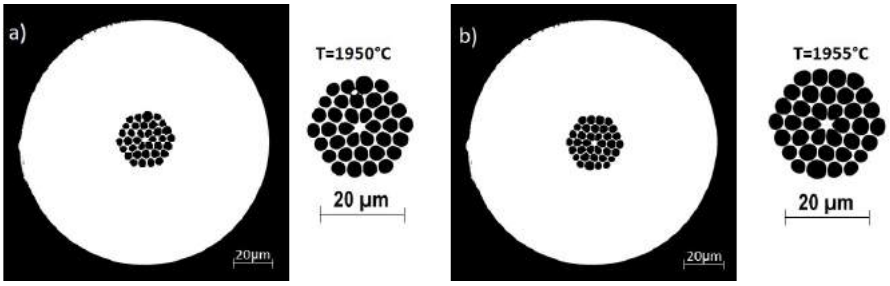

Figure 4.12: Optical microscope cross section images of two fibers: a) T=1950 °C, b)1955 °C.

The optical microscope cross sections of these two fibers are shown in figure 4.12 (a) and (b).

For these two fabricated fibers, we can conclude that when we have a lower temperature, we can obtain a smaller structure (lower values of air-hole diameters and pitch), which is visually clear in figure 4.12. The geometrical parameters of these fibers are also presented in table 4.5. The air-hole structure in general is smaller at lower temperature, but the ratio is bigger. On the basis of the geometrical parameters obtained and presented in table 4.5, we calculated dispersion curves for the two fibers. They are shown in figure 4.13. We can see here that the zero dispersion wavelength (ZDW) is

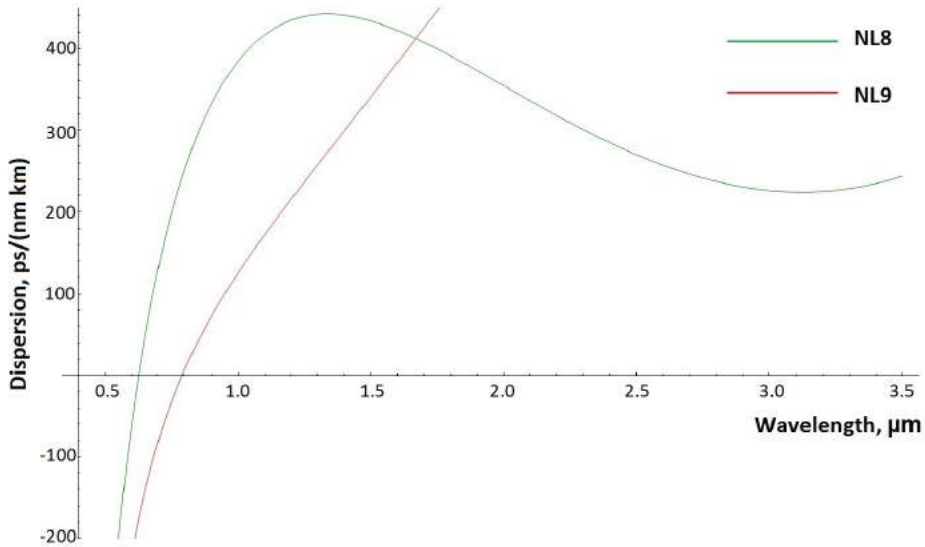

Figure 4.13: Dispersion curves for 2 fabricated fibers (from the third group) with temperature changes.

lower than in the previous groups, about 0.63 μm for fiber NL8 (for 1950 °C), and 0.8 μm for fiber NL9 (for 1955 °C).

Fiber No.	Velocity of drawing(m/min)	P (mBar)	T °C	diameter (μm)	Λ (μm)	d core (μm)	Ratio d/Λ
N8	41	115	1950	3.67	4.00	2.66	0.91
N9	41	115	1955	4.00	4.57	2.62	0.87

Table 4.5: Fabrication parameters and obtained geometrical parameters of the third group of fibers.

In figure 4.14 the attenuation graphics for the third group of 3 ring fibers are shown; they include data for 2 fibers fabricated only at different temperatures. It is clear from the graphic that the best one is the NL9 fiber, fabricated at 1955 °C, although fiber NL8, fabricated at 1950 °C, is better in a little wavelength range between 1580 and 1700 nm, and in a little wavelength range around 1350 nm. The average losses for this group are about 400-500 dB/km; the losses are very high in comparison with the ones of the fibers from the two previous groups.

To compare all the fabricated 3 ring fibers, we prepared table 4.6, where data for the 9 fabricated fibers are presented. Data about the most impor-

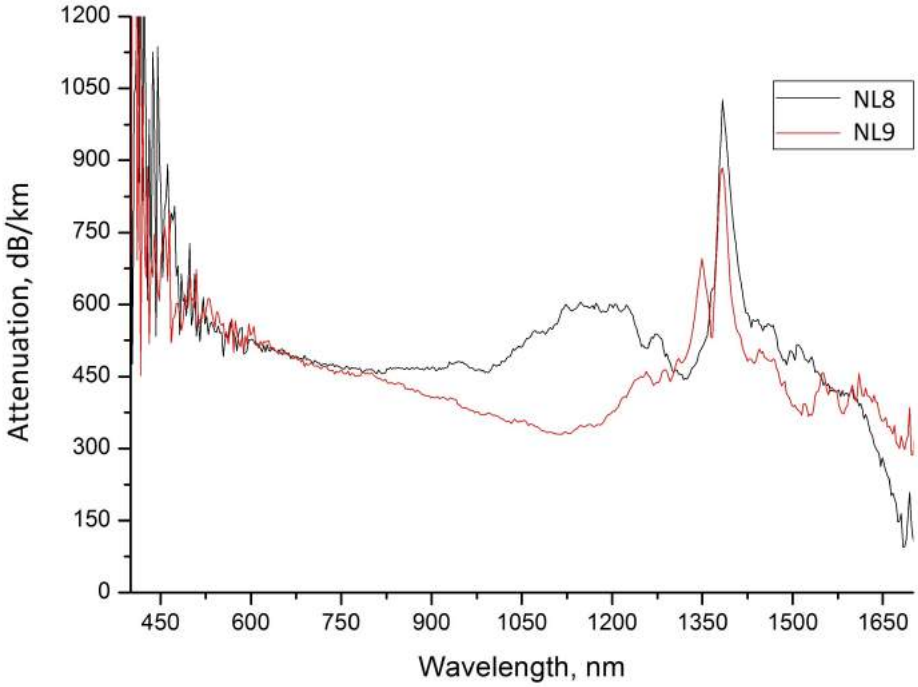

Figure 4.14: Graphic of attenuation for the third group of 3 ring fabricated fibers

tant parameter, the wavelength of zero dispersion for each fiber, are also presented in the table.

4.5.2 6 ring PCF

To reduce the fiber confinement losses [67], a second stack was created with 6 rings of air holes surrounding the core. The design and fabrication of these fibers was carried out by the thesis advisor and the author. The stack design is shown in figure 4.15 (a). The preform, formed by tubes, is shown in figure 4.15 (b) and (c). The stack was drawn to produce around 10 canes of 3 mm in diameter. An optical microscope transversal image of the cane used to draw fibers can be seen in figure 4.15 (d).

From these canes, about 17 different fibers with different parameters of pressure, temperature, and draw velocity were fabricated. In this chapter, we will analyze only 3 of these fibers, the 3 best ones, with regular structure and relatively small air-hole diameters. The transversal cut images of these

Fiber No.	Vel. draw. (m/min)	P (mBar)	T °C	d (μm)	Λ (μm)	d core (μm)	Ratio d/Λ	$\lambda\circ$ (nm)
NL1	25	100	1950	3.62	4.219	2.42	0.86	933
NL2	32	100	1950	1.73	2.501	2.52	0.69	904
NL3	36	100	1950	1.13	2.025	2.83	0.56	885
NL4	40	100	1950	0.76	1.805	3.09	0.43	917
NL5	40	108	1950	1.91	2.419	2.628	0.79	864
NL6	40	110	1950	2.46	2.864	3.050	0.86	821
NL7	40	115	1950	2.73	3.227	3.844	0.84	922
NL8	41	115	1950	3.67	4.00	2.66	0.91	627
NL9	41	115	1955	4.00	4.57	2.62	0.87	790

Table 4.6: Fabrication parameters and obtained geometrical parameters for all fabricated 3 ring fibers, including the wavelength of zero dispersion.

three fibers are shown in figure 4.16. The first fiber (NL10) in figure 4.16(a) was fabricated at a drawing velocity of 35 m/min, while the second fiber (NL11) shown in the figure 4.16(b) was fabricated at a drawing velocity of 45 m/min (these two fibers were fabricated in the same process from the same preform); the third fiber (NL12), shown in figure 4.16(c), was fabricated at a drawing velocity of 40 m/min. For all this three fibers the drawing parameters were set to give the required fiber outer diameter of approximately 123.5 μm. The pressure inside the holes was set at 115 mBar. All the three fibers were fabricated at temperature of 1950 °C.

To have more precision in the measurement of the geometrical fiber parameters, we decided to use an Atom Force Microscope (AFM) for the measurements. In figure 4.17(a), it is possible to see a transversal cut image obtained for the air-hole structure region of fiber NL12. In figure 4.17(b), we can see the section of the structure near the core of the same fiber. If we compare the pictures obtained with the optical microscope and with the AFM for the same fiber, it is clear that with the AFM we obtain the parameters of the fibers more precisely.

Fiber No.	Vel. draw. (m/min)	P (mBar)	T °C	d (μm)	Λ (μm)	d core (μm)	Ratio d/Λ	$\lambda\circ$ (nm)
NL10	35	-	1950	1.96	3.137	3.86	0.62	990
NL11	45	-	1950	1.68	2.934	3.93	0.57	985
NL12	40	-	1950	2.01	3.183	4.15	0.63	992

Table 4.7: Obtained geometrical parameters for 6 ring fibers.

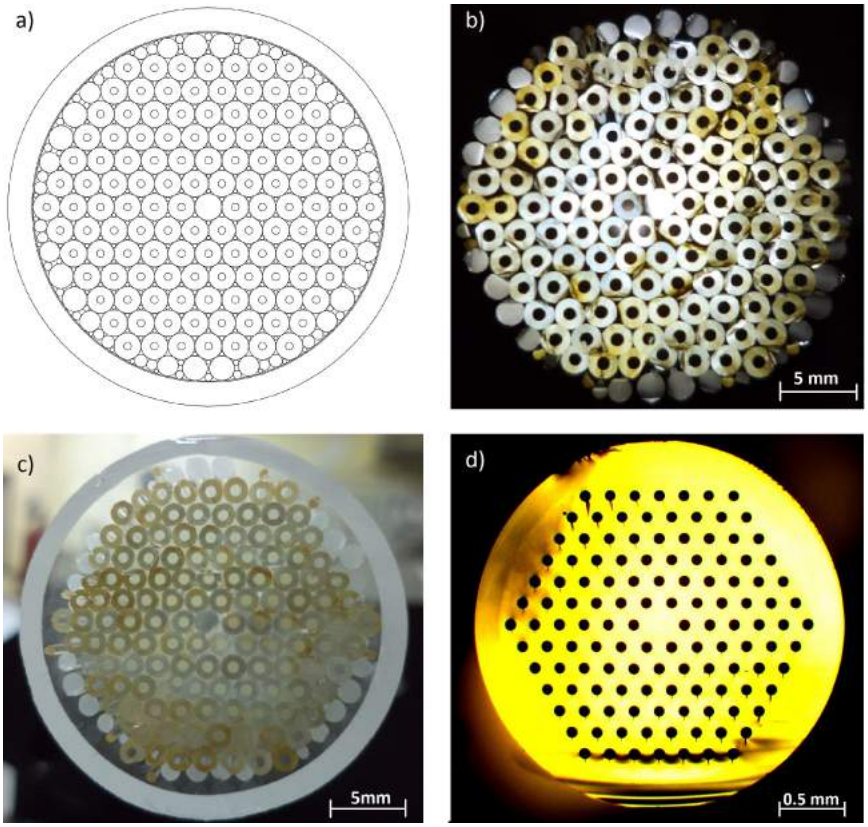

Figure 4.15: 6-ring fiber a) Stack design, b) and c) Array of tubes, forming the preform, d) Optical microscope image of a cane cross section.

From the measurements made with the AFM, we prepared table 4.7, in which we can see the parameters of fiber fabrication, such as drawing velocity, temperature and pressure; the geometrical parameters obtained, such as air-hole diameter, pitch, d/Λ ratio and core diameter are also presented. Additionally, we present zero dispersions for the three fibers (ZDW).

On the basis of the results shown in table 4.7, we calculated the dispersion curves for these three fibers, which are shown in figure 4.18; in it, we can see that for the NL10 fiber and the NL12 fiber, the curves are practically the same, and that the NL11 fiber has lower dispersion in the wavelength range between 2.0 and 3.5 μm. The three curves cross the zero dispersion axis very close to each other, which means that they have very similar zero dispersion wavelength.

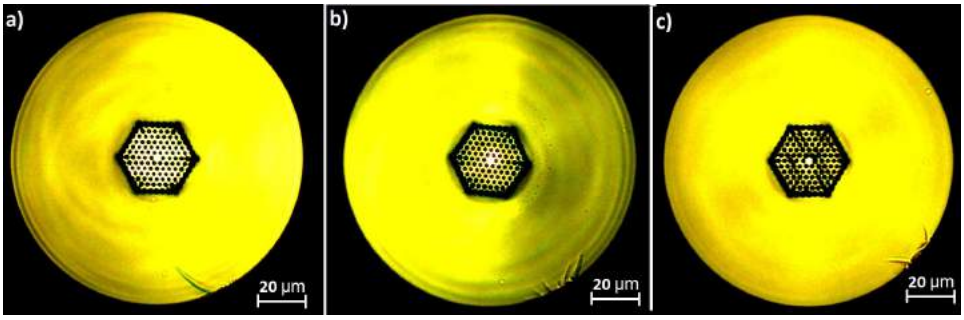

Figure 4.16: a) first fiber (NL10) fabricated with a drawing velocity of 35 m/min, b) second fiber (NL11) fabricated with a drawing velocity of 45 m/min and c) third fiber (NL12) fabricated with a drawing velocity of 40 m/min.

The graphic of loss distributions for this group of three fibers with 6 rings around the core are shown in figure 4.19. We can conclude from the point of view of loss distribution that the best fiber is the NL12 fiber, with losses of about 40-50 dB/km in the wavelength range of 750-1300 nm; the next one is the NL11 fiber, with losses of 300 dB/km in the same wavelength range; finally, the worst one is the NL10 fiber, which has losses of about 500-800 dB/km in the range from 600 nm to 1300 nm.

4.5.3 Conclusion

We can conclude from this chapter that it is possible to fabricate good fibers of 3 and 6 air-hole rings in the cladding, with more or less low losses, and that the fabricated fibers can be for different wavelengths.

From the point of view of flattened dispersion, the best fabricated fiber is the NL4 fiber; the fiber dispersion curve crosses the zero dispersion line at three points, whitin the range of wavelengths between 0.9 μm and 3 μm, and the fiber has a dispersion value of about $\pm$50 ps/nm/km. However, this fiber has very high attenuation in practically all the analyzed spectrum; in fact, this fiber has small diameters and small d/Λ ratio, which is why its transmission properties are bad. Then, the next best fiber from the point of view of flattened dispersion is the NL3 fiber; the fiber dispersion curve crosses the zero dispersion line axis at three points, and has acceptable losses in the analyzed range of wavelengths. In our dispersion simulation, we used a software for regular air-hole structures in the PCF cladding, which means the software is valid for structures with the same air-hole diameters. We really fabricated HNL PCFs with an irregular structure of air-holes in

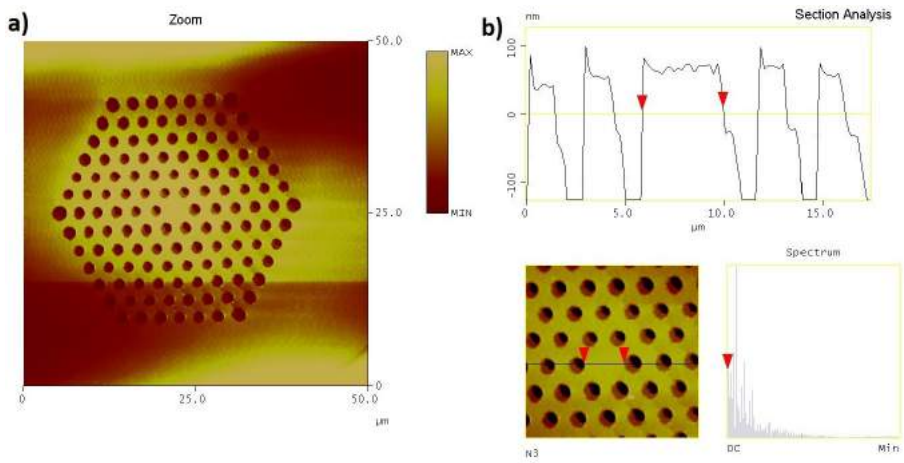

Figure 4.17: a) transversal cut image of the air-hole structure region for fiber NL12, b) section of the structure near the core of fiber NL12. Both pictures were taken using the Atomic Force Microscope.

the cladding (air-holes with different diameters). In chapter 6, devoted to supercontinuum generation in our fibers, we will discuss this case in details.

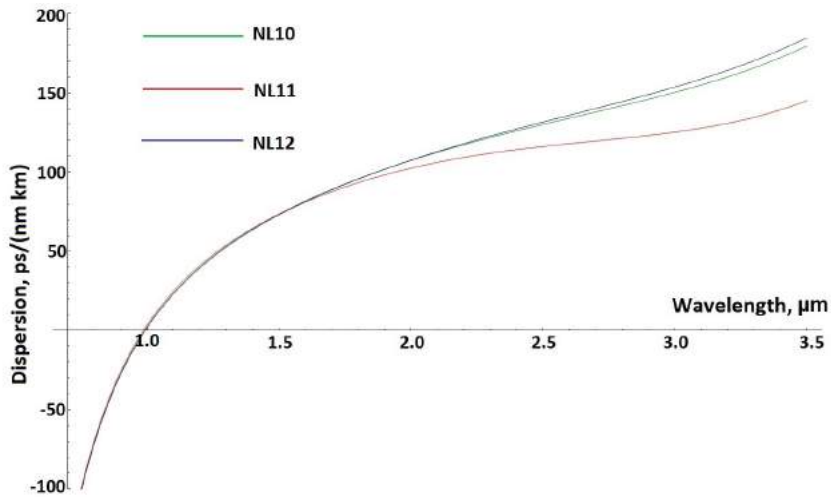

Figure 4.18: Dispersion curves for 6 ring fibers

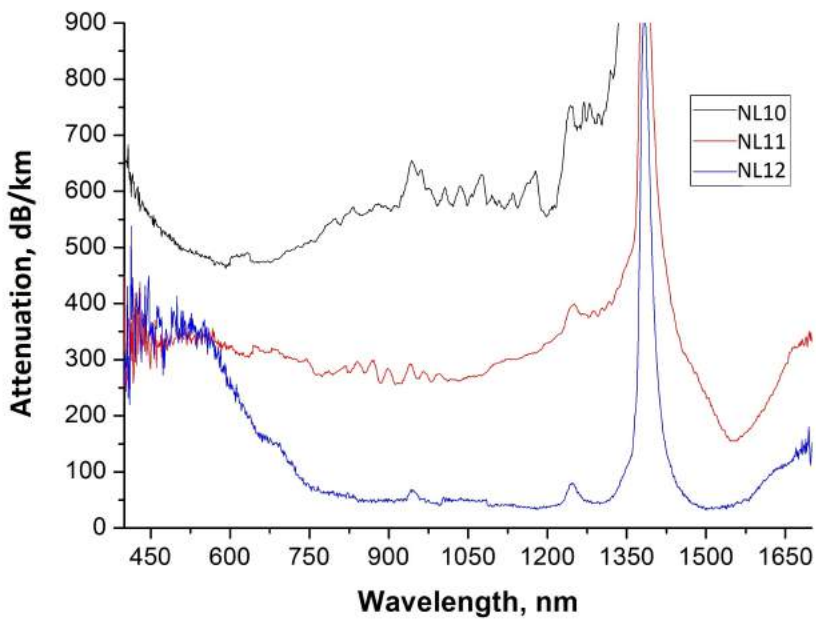

Figure 4.19: Attenuation distributions for the three 6 ring fibers

Chapter 5

Polarimetric parameters associated to special microstructured fibers[6]

5.1 Introduction

It is well known from conventional fiber theory that deviations from a fibers ideal structure (some imperfections or asymmetries) cause the two polarization states of the fundamental mode to experience different waveguiding properties; this is known as birefringence [17]. For some applications, it is necessary to enhance the difference, thus creating the high-birefringent or polarization-maintaining fibers [68]. For other applications, in particular for high-speed, long-distance optical communication systems, even low birefringence may greatly decrease upper limits for transmission speed of the system.

Index guiding microstructured fibers (IG MFs), also known as holey or photonic crystal fibers, guide light by means of total internal reflection between a solid core and cladding with multiple periodic air channels (holes) oriented along the fiber axis [19, 44, 69]. Actually, this kind of fibers has found large applications in laser physics [70], nonlinear optics [71], optical communication systems and optical fiber sensors [72, 73]. For these applications of microstructured fibers, as for conventional fibers, it is important to predict and understand the polarization properties of IG MFs, which may result from non-uniformities and asymmetries of microstructured cladding.

Unfortunately, the action of IG MFs fabrication conditions on the polarization properties of the fibers has not been discussed completely. The optical response to polarized light is usually represented by the Jones matrix formalism if there are no depolarization processes involved, but if there exists

the possibility to deal with depolarization effects, the Mueller-Stokes formulism must be employed to describe it correctly [74, 75, 76, 77]. In this sense, the determination of the Mueller matrix becomes the main objective as the first step for any polarimetric characterization, because it provides any possible information related with the optical response to polarized light at a given incident wavelength [75].

In this work, the Mueller matrices associated to six different home-made IG MFs are determined experimentally, at 1550 nm. Some polarimetric parameters are calculated directly from the Mueller matrices, which show that the fiber fabrication parameters have a clear effect on the output degree of polarization, providing an inverse relationship between the degree of polarization output and the relative hole diameter, d/Λ value. The obtained results show that the investigated optical fibers can be used in any application where high values for the degree of polarization are required, at totally polarized incident illumination.

It is well known that the Mueller-Stokes formalism describes the linear response of an optical medium (characterized by the Mueller matrix M) to the polarization intensity (denoted by a Stokes vector S), according to [74]

$$S^0 = MS^1 \begin{bmatrix} {S_0}^0 \\ {S_1}^0 \\ {S_2}^0 \\ {S_3}^0 \end{bmatrix} = \begin{bmatrix} m_{00} & m_{01} & m_{02} & m_{03} \\ m_{10} & m_{11} & m_{12} & m_{13} \\ m_{20} & m_{21} & m_{22} & m_{23} \\ m_{30} & m_{31} & m_{32} & m_{33} \end{bmatrix} \begin{bmatrix} {S_0}^i \\ {S_1}^i \\ {S_2}^i \\ {S_3}^i \end{bmatrix} = \tag{5.1}$$

$$\begin{bmatrix} m_{00}{S_0}^i + m_{01}{S_1}^i + m_{02}{S_2}^i + m_{03}{S_3}^i \\ m_{10}{S_0}^i + m_{11}{S_1}^i + m_{12}{S_2}^i + m_{13}{S_3}^i \\ m_{20}{S_0}^i + m_{21}{S_1}^i + m_{22}{S_2}^i + m_{23}{S_3}^i \\ m_{30}{S_0}^i + m_{31}{S_1}^i + m_{32}{S_2}^i + m_{33}{S_3}^i \end{bmatrix} \tag{5.2}$$

where S^i and S^0 represent the polarization state of the incident and the output light beams, respectively, defined in terms of the orthogonal components of the electric field vector (E_p, E_s) and their phase differences.

The Mueller matrix contains all the information related with the optical characteristics associated to any given optical system [74]. The normalized polarized Stokes parameters can be expressed in terms of the azimuth ($0 \leq 2\psi \leq \pi/2$) and the ellipticity ($-\pi/2 \leq 2\varepsilon \leq \pi/2$) angles of the Poincarè sphere [74]

$$S = S_0 DoP \begin{bmatrix} 1 \\ cos(2\varepsilon)cos(2\psi) \\ cos(2\varepsilon)sin(2\psi) \\ sin(2\varepsilon) \end{bmatrix} \tag{5.3}$$

where S_0 represents the average light intensity associated to the Stokes parameters, and DoP is the degree of polarization [74]

$$0 \leq DoP = \frac{\sqrt{{S_1}^2 + {S_2}^2 + {S_3}^2}}{S_0} \leq 1 \tag{5.4}$$

Where value 0 is associated to totally un-polarized light, the upper limit means the beam is totally polarized, and the remaining values are associated to partially polarized light.

5.2 Fabrication of microstructured Fibers

We fabricated silica IG MFs with different cladding structures. In some fibers, the diameter of the holes d had different values, but the same hole-to-hole spacing (pitch Λ) everywhere, see fibers N1 and N5 in Figs. 5.1(a) and 5.1(e); in other fibers, with the best uniformity of the cladding structure, diameter of the holes d had almost the same value, and pitchΛ was equal for the cladding structures, see fibers N2, N3, N4, N6 in Figs. 5.1(b), 5.1(c), 5.1(d), and 5.1(f), respectively.

In our fabrication process, we used the stack-and-draw technique [44]. First, we fabricated identical capillary tubes and rods with previously calculated sizes to make fibers with 3 rings of air-holes around the core [66]. Then, the preforms were prepared; that is, we arranged the fabricated capillaries in a hexagonal structure around a rod inside a 20x16 mm tube. The large-mode-area fibers, N1-N4, were drawn from the prepared preforms in one step process. Fiber N1 was drawn without any pressure inside capillaries, Fibers N2, N3, and N4 were drawn from the same preform, but with different pressures inside capillaries of 14, 15, and 16 mbar, respectively. Nonlinear fibers N5 and N6 were drawn in two step process. In the first drawing process, we fabricated canes with an outside diameter of 1.8 mm.

The canes were inserted into jacket tubes with an outside diameter of 12 mm and an inside diameter of 2 mm, and then, after the second drawing

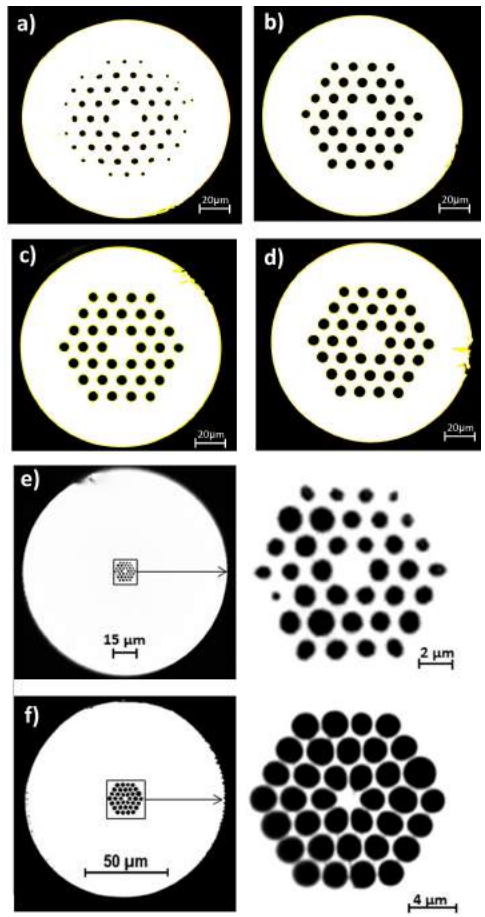

Figure 5.1: Images of the fabricated fiber cleaved end faces obtained with a Leica DM2500 microscope: a) fiber N1, b) fiber N2, c) fiber N3, d) fiber N4, e) fiber N5, f) fiber N6.

process, we obtained the designed fibers. Fiber N5 was manufactured with a cane fabricated from the preform prepared with capillary tubes of the same outside diameter, but with a different inside diameter, and they were accidentally arranged in a hexagonal structure around a rod inside a 20x16 mm tube. The fiber was drawn at a constant pressure of 100 mbar inside the cane.

Fiber N6 was made with a cane fabricated with identical capillary tubes and with a pressure of 110 mbar inside the cane. The outside diameter of the fabricated fibers is about 123 μm. During the drawing, the fibers were coated with a conventional polymer coating, yielding an outer diameter of

fiber	hole	Pitch Λ (μm)	Outside fiber diameter(μm)	D core (μm)	d/Λ
N1	3.52	10.31	122.2	21.79	0.33
N2	4.68	12.63	122.5	24.801	0.37
N3	5.03	12.60	123.2	24.70	0.40
N4	6.67	13.33	123.0	26.06	0.50
N5	1.13	2.03	123.2	2.83	0.56
N6	3.63	4.22	123.3	2.84	0.86

Table 5.1: Measured geometric parameters for 6 fabricated fibers.

250 μm. The images of the cleaved end faces for the six investigated fibers were obtained with a Leica DM2500 optical video microscope (see Fig.5.1). All the geometric parameters of the fibers were measured with a commercial scanning atomic force microscope (Digital Instruments) with a resolution of 50 nm for 30 μm X 30 μm images. The measured geometric parameters for the 6 fabricated fibers are presented in Table 5.1.

The modal structures of the investigated fibers were estimated using a focused beam from a standard red He-Ne laser centered at 632.8 nm. Specifically, the far-field measurements showed that fibers N1-N5 were single-mode (or quasi single-mode) fibers [66] at 632.8 nm. Fiber N6 was a multimode fiber for the wavelength of 632.8 nm.

5.3 Polarimetric characterization

The experimental determination of the Mueller matrices associated to the special optical fibers we are reporting here was performed employing the same experimental setup (Fig. 5.2) and a similar method of analysis recently reported in [77].

A tunable laser, within a 1450-1590 nm range (Anritsu, Tunics Plus SC), tuned at 1550 nm was used as the source of the Deterministic Polarization Controller, DPC, (Thorlabs, model DPC5500). An arbitrary input polarization state enters the DPC, while at its output we obtain a signal with a fixed and predetermined polarization state. The output signal from the DPC is used as a polarization state generator, PSG, for the fiber being studied, which is connected directly to the polarizer state analyzer, PSA, (Thorlabs, model PAX5710/IR3). A computer controls the PSG and the PSA, and

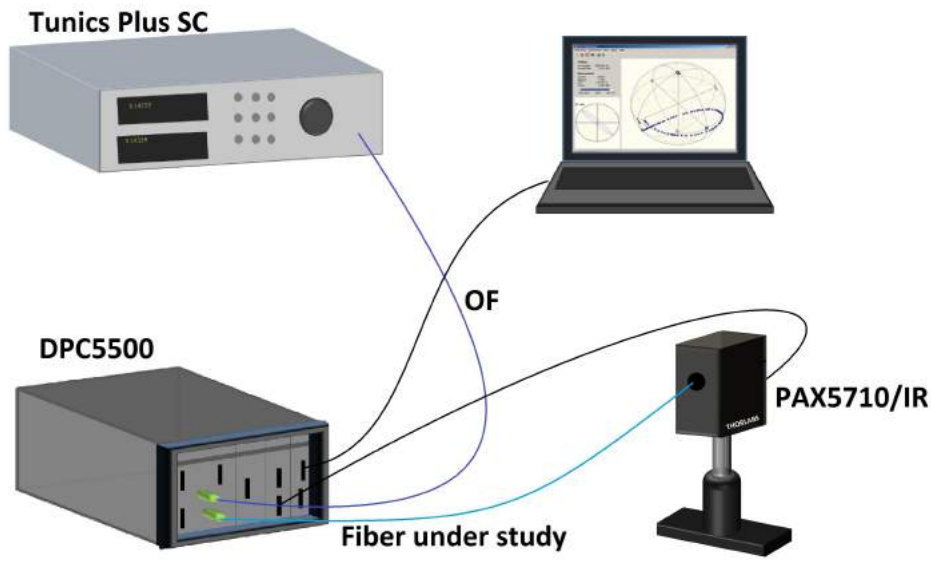

Figure 5.2: Experimental setup used for the determination of the Mueller matrices of the investigated fibers.

a computer program provides the calculation of the Mueller matrix, using the Stokes vectors measured. For each polarization state generated, the polarimeter analyzes the Stokes vector of the light beam leaving the system under study. Then, six measurements provide the 16 Mueller parameters required. The incident and the analyzed Stokes vectors correspond to linear polarization states parallel (p), perpendicular (s), at +45 degrees (+) and at -45 degrees (-), and to circular right- (r) and left-hand (l) polarization states, respectively [77].

The experimental Mueller matrices, normalized with respect to the m00 element, are given by Eqs. (3.1-3.6). By applying some of the relationships given in Table 1 of Ref. [77], it is possible to analyze some polarimetric properties associated to the 2 m long optical fibers (see Table 5.2).

$$M_{N1} = \begin{bmatrix} 1.0000 & -0.0149 & 0.0901 & 0.0197 \\ 0.0138 & 0.9489 & 0.2449 & 0.0582 \\ 0.0494 & 0.0436 & 0.4545 & 0.8528 \\ -0.1217 & 0.2581 & -0.8201 & 0.4321 \end{bmatrix} \tag{5.5}$$

$$M_{N2} = \begin{bmatrix} 1.0000 & -0.0011 & 0.0511 & -0.0183 \\ 0.0316 & 0.7583 & 0.5102 & 0.0926 \\ -0.0314 & 0.4537 & -0.0739 & 0.8674 \\ -0.0469 & 0.4107 & -0.8386 & -0.2805 \end{bmatrix} \tag{5.6}$$

$$M_{N3} = \begin{bmatrix} 1.0000 & 0.0004 & 0.0768 & 0.0090 \\ 0.0554 & 0.1146 & 0.7910 & 0.5786 \\ 0.0001 & -0.2013 & -0.3755 & 0.7624 \\ -0.0034 & 0.9324 & -0.2167 & 0.1299 \end{bmatrix} \tag{5.7}$$

$$M_{N4} = \begin{bmatrix} 1.0000 & -0.0087 & 0.0521 & 0.0004 \\ 0.0224 & 0.3386 & 0.8538 & 0.2388 \\ 0.0464 & -0.8529 & 0.3143 & -0.1705 \\ -0.0274 & 0.0567 & 0.4000 & 0.8442 \end{bmatrix} \tag{5.8}$$

$$M_{N5} = \begin{bmatrix} 1.0000 & -0.0060 & 0.0599 & -0.0295 \\ 0.0205 & 0.5414 & -0.1693 & -0.5274 \\ -0.0083 & 0.8592 & 0.2825 & 0.3957 \\ -0.0392 & 0.2195 & -0.9381 & 0.2755 \end{bmatrix} \tag{5.9}$$

$$M_{N6} = \begin{bmatrix} 1.0000 & -0.0340 & 0.2744 & 0.1946 \\ -0.2462 & 0.2775 & -0.7945 & -0.4777 \\ -0.1719 & -0.6040 & -0.2187 & -0.4631 \\ -0.0893 & 0.3539 & 0.1853 & -0.5537 \end{bmatrix} \tag{5.10}$$

The theorem of Gil-Bernabeu (TGB) is a necessary and sufficient condition for a Mueller matrix to be expressed in terms of a Jones matrix, for a passive optical system. It can be formulated as [78]

$$0 \leq TGB = \frac{Tr(M^T M)}{4{m_{00}}^2} \leq 1, \tag{5.11}$$

where the lower limit is associated to a totally depolarizing system, the upper limit means the system does not depolarize at all, and the intermediate values are associated to partial depolarization. The depolarization index, DI(M), is defined as [79]

$$0 \leq DI(M) = \frac{\sqrt{\sum_{j,k=0}^{3} {m_{jk}}^2 - {m_{00}}^2}}{\sqrt{3} m_{00}} \leq 1 \tag{5.12}$$

It is a measure of the average capability of the system to depolarize the incident light (0 means the system depolarizes totally, and 1 means the

system does not depolarize, while the intermediate values are associated to partial depolarization, independently of the incident polarization state). Indeed, DI(M) could be interpreted as the output degree of polarization (DoP) averaged over all the possible polarization states incident from the Poincarè sphere.

The Average degree of polarization (Avg. DoP) is defined by integrating the degree of polarization DoP as the incident Stokes vector S varies over the Poincarè sphere, normalized with $1/(4\pi)$ for the area of the sphere [80]:

$$Avg.DoP = \frac{\int_0^{2\pi}\int_{-\pi/2}^{\pi/2} DoP[MS(\theta,\phi)]cos(\phi)d\phi d\theta}{4\pi} \tag{5.13}$$

Q(M) is a scalar metric, defined as [81]

$$0 \leq Q(M) = \frac{\sum_{j=1,k=0}^{3} {m_{jk}}^2}{\sum_{k=0}^{3} {m_{0k}}^2} = \frac{3[DI(M)]^2 - [D(M)]^2}{1+[D(M)]^2} = \tag{5.14}$$

$$= \frac{\frac{\sum_{j,k=1}^{3} {m_{jk}}^2}{{m_{00}}^2} + [P(M)]^2}{1+[D(M)]^2} \leq 3 \tag{5.15}$$

where the upper limit indicates the systems does not depolarize and also does not diattenuate. Add is the anisotropic degree of depolarization [82],

$$0 \leq Add = \frac{{(DoP)^0}_{Max} - {(DoP)^0}_{min}}{{(DoP)^0}_{Max} + {(DoP)^0}_{min}} \leq 1 \tag{5.16}$$

PDL is the polarization dependent loss [76]

$$PDL = 10log\frac{T_{max}}{T_{min}} = 10log\frac{m_{00} + \sqrt{(}{m_{01}}^2 + {m_{02}}^2 + {m_{03}}^2)}{m_{00} - \sqrt{(}{m_{01}}^2 + {m_{02}}^2 + {m_{03}}^2)} \tag{5.17}$$

D(M), LD, and CD indicate the total-, linear and circulardiattenuation parameters, respectively [83]

$$0 \leq D(M) = \frac{\sqrt{{m_{01}}^2 + {m_{02}}^2 + {m_{03}}^2}}{m_{00}} \leq 1 \tag{5.18}$$

$$0 \leq LD(M) = \frac{\sqrt{{m_{01}}^2 + {m_{02}}^2}}{m_{00}} \leq 1 \tag{5.19}$$

No.	TGB	DI(M)	Avg.DoP	Q(M)	Add	PDL
N1	0.9629	0.9749	0.9737	2.8182	0.0811	1.8740
N2	0.9413	0.9601	0.9532	2.7542	0.1475	1.0863
N3	0.9197	0.9450	0.9438	2.6570	0.0605	1.5505
N4	0.9095	0.9377	0.9262	2.6279	0.2002	1.0574
N5	0.8740	0.9121	0.9070	2.4802	0.0795	1.3434
N6	0.8106	0.8645	0.8418	1.9095	0.1550	7.0400
No.	D(M)	LD	CD	P(M)	LP	CP
N1	0.0934	0.0913	0.0197	0.1320	0.0513	0.1217
N2	0.0543	0.0511	0.0183	0.0647	0.0446	0.0469
N3	0.0774	0.0769	0.0090	0.0555	0.0554	0.0034
N4	0.0528	0.0528	0.0004	0.0583	0.0515	0.0274
N5	0.0671	0.0602	0.0295	0.0450	0.0221	0.0392
N6	0.3381	0.2765	0.1946	0.3133	0.3002	0.0893

Table 5.2: Measured geometric parameters for 6 fabricated fibers.

$$0 \leq CD(M) = \frac{\sqrt{{m_{03}}^2}}{m_{00}} \leq 1 \tag{5.20}$$

P(M), LP, and CP indicate total-, linear- and circular-polarizance parameters, respectively [83]

$$0 \leq P(M) = \frac{\sqrt{{m_{10}}^2 + {m_{20}}^2 + {m_{30}}^2}}{m_{00}} \leq 1 \tag{5.21}$$

$$0 \leq LP(M) = \frac{\sqrt{{m_{10}}^2 + {m_{20}}^2}}{m_{00}} \leq 1 \tag{5.22}$$

$$0 \leq CP(M) = \frac{\sqrt{{m_{30}}^2}}{m_{00}} \leq 1 \tag{5.23}$$

The data shown in table 5.2 represent the average linear response of the optical fibers to any linear, circular or elliptical incident polarization state, even when only six different polarization states have been used for the incidence.We have ordered the data according the optical fiber average depolarization capability, where the first four scalar metrics (theorem of Gil-Bernabeu, TGB, depolarization index, DI(M), Avg. DoP, and Q(M) metric) indicate that the optical fibers depolarize slightly, all of them following the same tendency consistently.

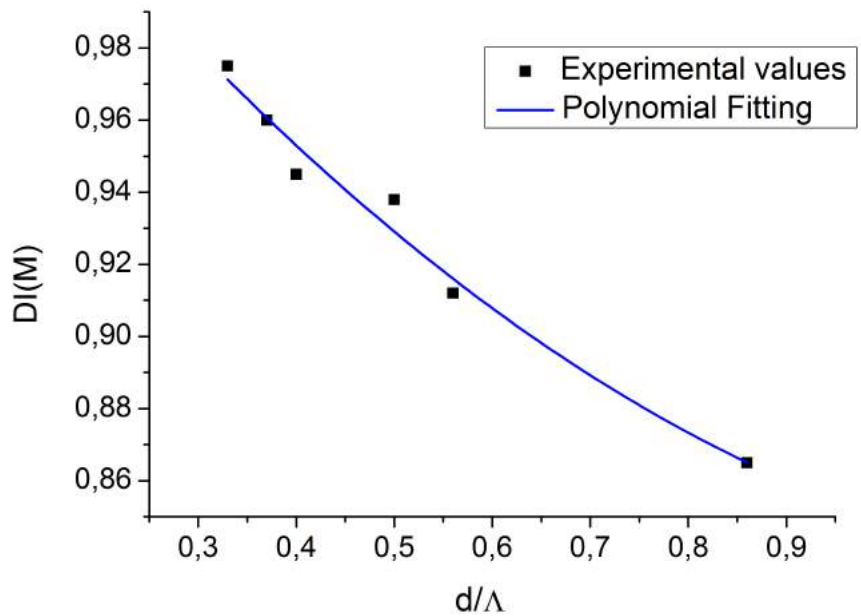

Figure 5.3: Correlation between the relative hole diameter d/Λ and the depolarization index DI(M) for the investigated fibers.

The anisotropic degree of depolarization, Add, shows that all the optical fibers can depolarize slightly; this result implies that the fiber depolarizes light depending on the type of the transmitted polarization state employed. Fiber N4 exhibits the lowest polarization dependent loss, PDL, while fiber N6 presents the highest loss. Fiber N6 also presents a total diattenuation value corresponding to an order of magnitude higher than those associated to the remaining fibers of the set studied here. Fibers N1 and N6 have associated polarizance parameter values with an order of magnitude higher than fibers N2-N5, which imply they have a tendency to polarize light circularly (N1) and linearly (N6), respectively.

Comparing the results shown in Table 5.1 and Table 5.2, a clear correlation of the relative hole diameter, d/Λ, exists with the depolarization index, DI(M) [or the degree of polarization (DoP)]: a lower ratio implies a higher DI(M) (or DoP) output, and conversely, a higher ratio provides a lower DI(M) (or DoP).

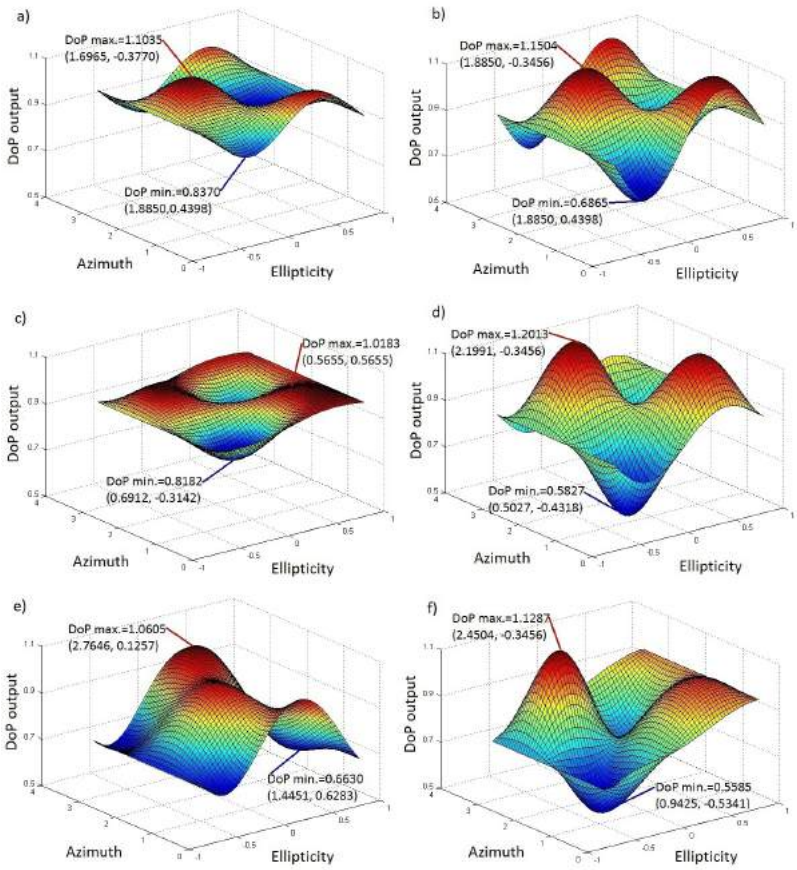

Figure 5.4: Output degree of polarization versus the azimuthal (ψ) and the ellipticity (ϵ) angles, for fibers N1 (Fig. 1a), N2 (Fig. 1b), N3, (Fig. 1c), N4, (Fig. 1d), N5 (Fig. 1e), and N6 (Fig. 1f).The values in brackets are the azimuth and the ellipticity angles, respectively, expressed in radians.

This correlation is shown also in Fig. 5.3. Probably the increase of an inflation pressure into the cladding holes leads to the increase of imperfection numbers [84] along the IG MFs. Figure 5.4 shows the graphical representation of the output degree of polarization, as a function of the incident polarization states for the six optical fibers. The basal plane, defined by the azimuth and the ellipticity angles, is the mapped representation of the Poincarè sphere, for incident totally polarized states (for which DoP =1).

Note that the general DoP output behavior associated to fiber N5 (Fig. 5.4.e) differs notably from the rest of the fibers. Ellipticity values close to zero mean that the fiber maintains higher DoP output values preferably for

incident totally polarized linear states (located at the equator in the Poincaré sphere), possibly due to cladding asymmetry (see Fig. 5.1e) and azimuthally asymmetric axial stress distributions [85] in the fiber. On the other hand, the remaining optical fibers show some similar DoP output behavior among them. Note that some transmitted polarization states maintain the degree of polarization, but others are affected by the fibers, generating slightly low depolarization values. Even when the incident polarization state could change under transmission, the average degree of polarization tends to be maintained.

The scalar metrics show the general tendency of a given system towards incident polarization. Based only on the information provided by the scalar metrics, according to table 5.2, all of those values are associated to physically realizable processes (they are located within their defined limits). However, when the analysis is applied in more detail, it is possible to find un-physically realizable points, as can be observed from Fig. 5.4, where there exist maximum values outside the physical limit for the output degree of polarization (the corresponding incident Stokes vectors can be obtained from Eq. 5.3, using the azimuth and the ellipticity angles). We think those values are associated to unstable incident Stokes vectors (we have registered physical realizable limits for the 6 basic polarization states measured experimentally). The general behavior associated to the output degree of polarization of the fibers studied here could be of great interest for some specific applications where the coherence of light transmitted by optical fibers requires to be maintained.

5.4 Conclusion

Six special home-made IG MFs with different relative hole diameter d/Λ were fabricated and their polarimetric parameters were investigated. The linear response to 1550 nm polarized light was determined experimentally for the six fibers, and their Mueller matrices were explicitly reported. A polarimetric analysis showed that the fiber fabrication parameters had a clear effect on the output degree of polarization, providing an inverse relationship between the degree of polarization output and the relative hole diameter, d/Λ value.

It seems that the increase of an inflation pressure into the cladding holes leads to the increase of imperfection numbers along the IG MFs. Additional

experiments are being conducted to understand this result more correctly. Fibers with the physical characteristics reported here could be useful for those who are searching for applications where the spatial coherence (degree of polarization) under transmission through an optical fiber could be a relevant factor.

Chapter 6

Supercontinuum Generation in Special Microstructured Fibers With Irregular and Regular Claddings Using Pumping Wavelengths in a Broad Range [7]

6.1 Introduction

Index-guiding microstructured optical fibers (IG MOFs), also known as holey or photonic crystal fibers, consist of a solid core surrounded by a cladding with multiple periodic air channels (holes) oriented along the fiber axis, and they guide light by means of total internal reflection [19], [86]. Such optical fibers have unique properties that are very important for applications in laser physics, nonlinear optics, optical communication systems and optical technology. The unique properties of IG-MOFs allow the possibility of controlling their chromatic dispersion in a wide wavelength range by varying a hole diameter d and a hole-to-hole spacing, pitch Λ. To date, IG MOFs with zero dispersion wavelengths in the visible and near-infrared wavelengths [87][39][88][89], with two zero dispersions [90],[91], with varying dispersion [91][92][93], with flattened and near zero dispersion [94][60][95], and even with ultra-flattened and near zero chromatic dispersion for wavelengths of about 1.0 to 1.8 μm [96][40][57][97][98][61] have been reported. IG MOFs with ultra-flattened dispersion can be used in wide-band supercontinuum generation, dispersion compensation, ultra-short soliton pulse transmission, optical parametric amplification, wavelength-division multiplexing or pulse

reshaping [40][57][97][98][61][71]. However, the fabrication of a such type of IG MOFs is a very complicated process. For IG MOFs with the same air-hole diameter d [96]-[40], [98] it is necessary to fabricate at least 11 air-hole rings in the cladding with a relative hole diameter d/Λ of about 0.26. At this very small relative hole diameter, the confinement losses [67] in the IG MOFs, even for a large number of air-hole rings in the cladding, are very high. For example, the overal losses of the IG MOFs reported in [40] were of about 2 dB/m at 1500 nm. Other designs of IG MOFs consist of fibers with four or five rings of air-holes with different air-hole diameters in the cladding [57], [61]. Theoretical calculations show that such IG MOFs have low losses, and ultra-flattened and near zero chromatic dispersion for wavelengths of about 1.0 to 1.8 μm. However, the fabrication of such IG MOFs has not been reported in the literature until now. As it was mentioned before, there are some possibilities to obtain IG MOF with exotic dispersion properties, for example, by changing the hole diameter d, the pitch Λ, or the arrangement of air-holes. Thus, IG MOFs with regular or irregular cladding structures can exhibit new or exotic properties.

In this work, we report in detail on the fabrication of a special nonlinear silica IG MOF with different air-hole diameters in the cladding (irregular cladding) and its applications for supercontinuum (SC) generation. Some preliminary results about the properties of the fiber were reported in [7]. Our IG MOF has a constant pitch Λ and air-holes with different diameters. For comparison, supercontinuum generation in a nonlinear silica IG MOF with regular cladding is also investigated. It was found that SC in IG MOF with irregular cladding can be generated in a broader wavelength pumping range than in the IG-MOF with regular cladding.

6.2 Fabrication of nonlinear microstructured fibers

We fabricated two types of special nonlinear silica IG MOFs for SC generation. In the first type of the fiber, denoted here as IG-MOF with irregular cladding, the diameter of the holes d had different values, but the same pitch Λ everywhere. In the second type of MOF, denoted here as IG-MOF with regular cladding, the cladding structure was uniform: the diameters of the holes d had almost the same value, and the pitch Λ was equal for all the cladding structure. In our fabrication process, we used the well-established stack-and-draw technique [44]. First, we fabricated tubes and rods with previously calculated sizes to make special MOFs with 3 rings of air-holes

around the core to have a better higher-order mode suppression [66]. Then, the preforms were prepared; that is, we arranged the fabricated tubes in an hexagonal structure around a rod inside a 20x16 mm tube. In the first drawing process, we fabricated canes of 1.8 mm in outside diameter. The canes were inserted into jacket tubes with an outside diameter of 12 mm and an inside diameter of 2 mm, and then, after the second drawing process, we obtained our MOFs.

We fabricated the IG MOF with irregular cladding using a cane fabricated from the preform prepared with tubes of the same outside diameter but a different inside diameter, which were arranged arbitrarily in an hexagonal structure around a rod inside a 20x16 mm tube.

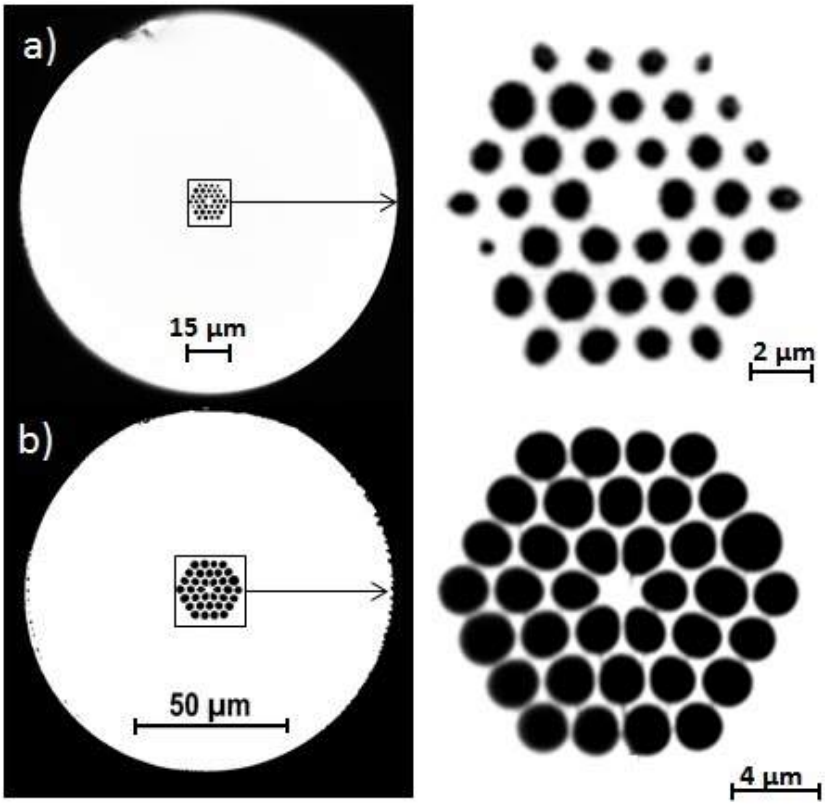

Figure 6.1: Images of the fiber cleaved end faces obtained with a Leica microscope DM2500: a) the MOF with irregular cladding, b) the MOF with regular cladding.

The MOF was drawn at a constant pressure of 100 mbar inside the cane. The IG MOF with regular cladding was manufactured with a cane fabricated

with identical tubes and with a pressure of 110 mbar inside the cane .

The outside diameter of the fabricated MOFs with either irregular or regular cladding was about 123 μm. During the drawing process, both MOFs were coated with a conventional polymer coating, giving an outer diameter of 250 μm. The parameters obtained for the MOF with irregular cladding are as follows: the average air-hole diameter is of 1.13 μm (diameters of the air-holes are different, and are from 0.82 μm to 1.25 μm), the average pitch is of about 2.03 μm, and the core diameter (i.e. the average diameter of the solid core at the center of the fiber) is of 2.84 μm; all the air-hole structure has about 10 μm in diameter. After fabrication, the profiles of the fiber modes were estimated using a focused beam from a standard red He-Ne laser centered at 632.8 nm with output power of 1 mW.

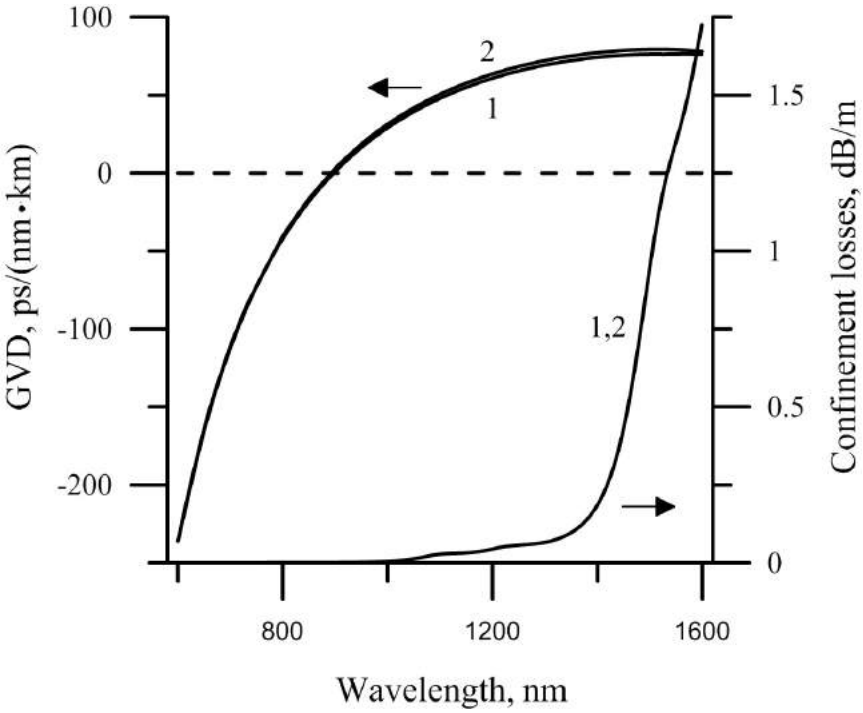

Figure 6.2: The spectral profiles of the GVD and confinement losses for two orthogonally polarized fundamental modes (1) and (2) of the MOF with irregular cladding. Zero GVDs take place at 897 nm and 893 nm for the modes (1) and (2), respectively.

Specifically, the far-field measurements showed that the MOF with irregular cladding was a single-mode fiber at such a wavelength. Our MOF with irregular cladding also has high birefringence [7], [6] and can be used, for

example, in some optical sensing devices or optical Kerr gates [37].

The IG MOF with a regular cladding structure had hole diameter with almost the same value for all the cladding structure of the fiber. The average diameter of the holes was 1.91 μm, the average pitch value was about 2.42 μm, and the core diameter was 2.63 μm.

The outside diameter of the fiber was also 123 μm. Our MOF with regular cladding was a multimode fiber for the wavelength of 632.8 nm. It is important to mention here that all the geometric parameters of our MOFs were measured with a commercial Dimension 3100 scanning atomic force microscope (Digital Instruments) with a resolution of 10 nm for 5 μm x 5 μm images. The images of the cleaved end faces for the two investigated MOFs, obtained with an optical microscope Leica DM2500, are shown in Fig. 6.1.

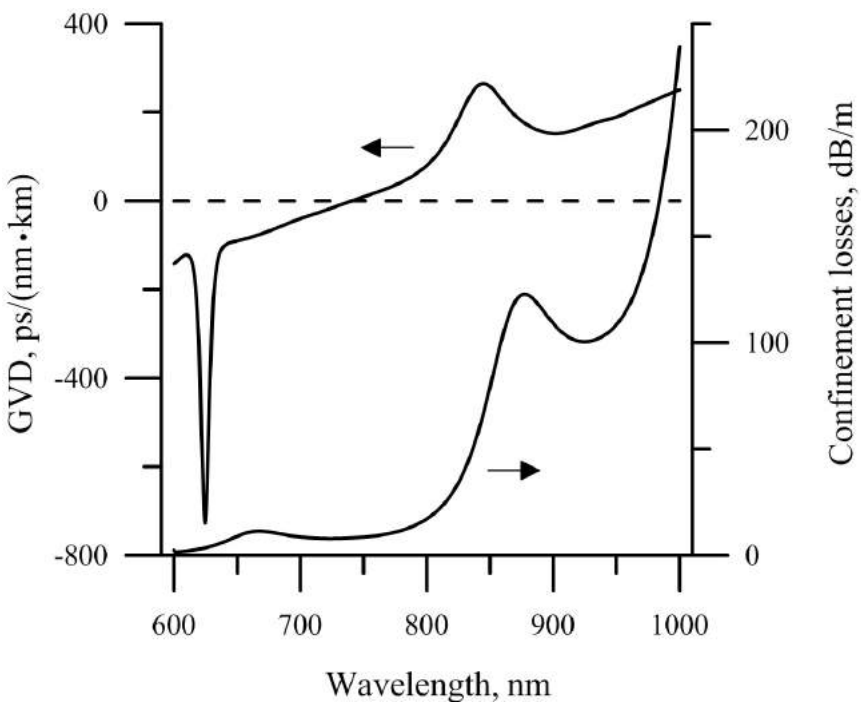

Figure 6.3: The spectral profiles of the GVD and confinement losses for the first higher-order mode of the MOF with irregular cladding. Zero GVD takes place at wavelength of 740.4 nm.

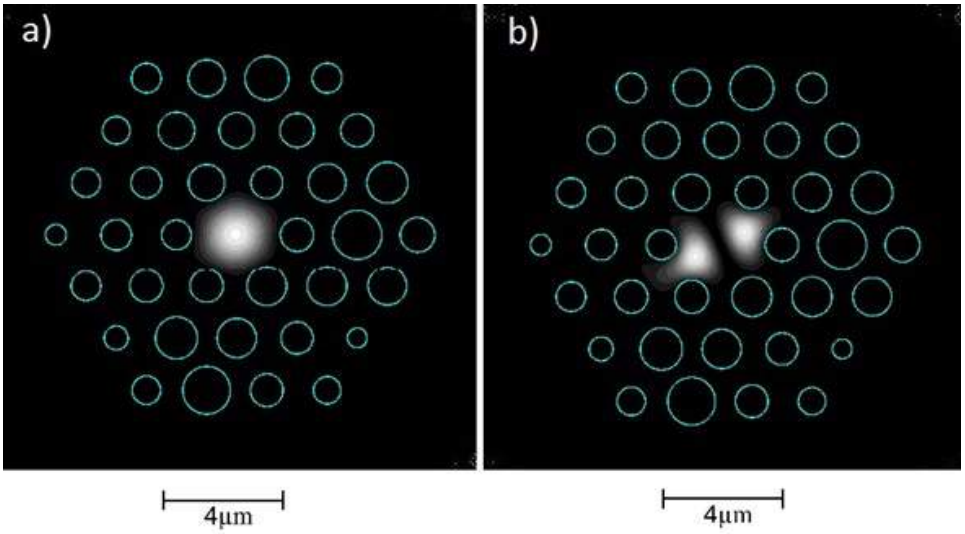

Figure 6.4: Calculated intensity profiles of (a) the fundamental mode (1) at 897 nm, and (b) the first higher mode at 740.4 nm of the MOF with irregular cladding.

6.3 Numerical simulations and discussion

The properties of the fabricated IG MOFs were calculated through the implementation of a full vectorial method for computing MOFs with a finite number of air holes that is based on an analysis of the integral equations for the transversal components of the magnetic field in the holes [7], [66], [99]. As it was shown in [66], this method is comparable in power to the multipole method [46], [100]. The precise transversal map of the holes was extracted from the images obtained using an atomic force microscope. Figure 6.2 and 6.3 demonstrate the calculated spectral profiles of the group-velocity dispersion (GVD) and the confinement losses for two orthogonally polarized fundamental LP01 modes, and for the first higher-order mode LP11 of the MOF with irregular cladding, respectively. The calculations were made with the use of the well-known Sellmeier formula for bulk silica glass [101]. The radius of the silica cladding was supposed to be 61.5 μm, and the complex refractive index of the used single-layer protecting acrylate coating to be 1.54-í2ů10-5. In the assessment of confinement losses for the first fiber we supposed the diameter d of all air-holes to be the same and equal to the above average diameter 1.13 μm. Validity of such approuch for IG MOFs with irregular cladding was experimentally confirmed in [102].The zero values of the GVDs for the fundamental modes (1) and (2), see Fig. 6.2, take

place at wavelengths of 897 nm and 893 nm, respectively.

Figure 6.3 shows that zero GVD for the first higher-order mode, which has minimal confinement losses among all the higher-order modes [103], takes place at a wavelength of 740.4 nm. Calculations also predict (see Fig. 6.3) that the higher-order mode posseses high confinement losses across the spectral window between 600 and 1000 nm (8.2 dB/m at 740 nm).

Figure 6.4 shows the calculated intensity profiles for both the fundamental and the first higher-order modes of the MOF with irregular cladding.

Fig. 6.5 illustrates the wavelength dependencies of the effective mode area

$$A_{eff} = \left(\iint_S S_z \, d\sigma\right)^2 \left(\iint_S {S_z}^2 \, d\sigma\right)^{-1} \tag{6.1}$$

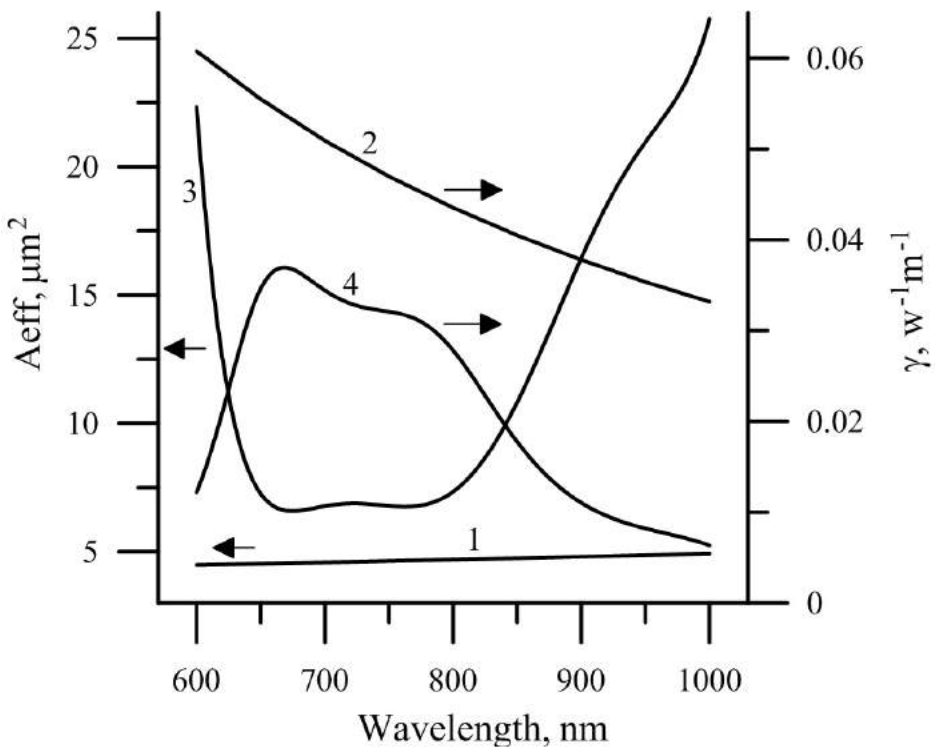

Figure 6.5: The spectral profiles of the effective area A_{eff} (1,3) and nonlinear parameter γ (2,4) of modes for the MOF with irregular cladding. Curves 1 and 2 refer to the fundamental mode, curves 3 and 4 refer to the first higher-order mode.

and the nonlinear parameter $\gamma = k_0 n_2 / A_{eff}$. Here S_z is the Pointing vector component directed along the fiber, k_0 is the vacuum wave number, $n_2 = 2.6 * 10^{-16} cm^2/W$ is the fused silica nonlinear-index coefficient and integration is performed over whole cross-section of the fiber [37].

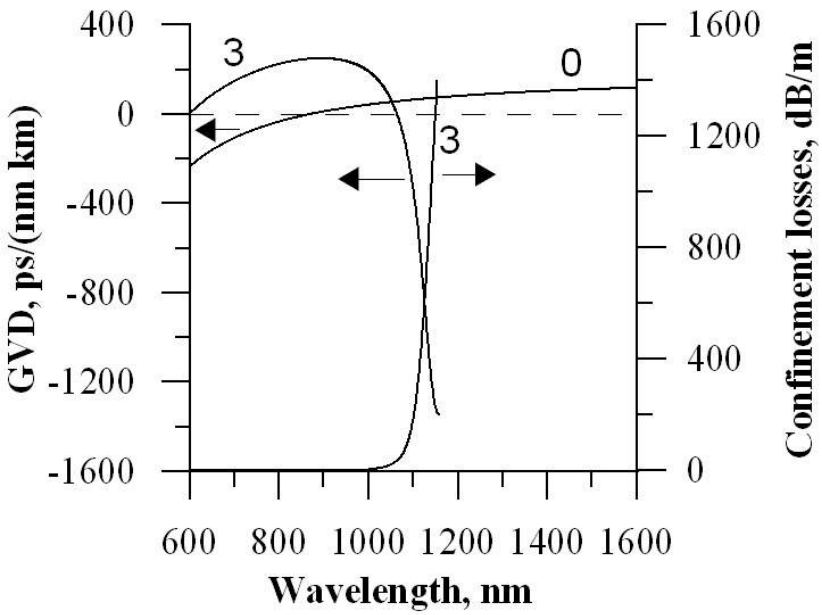

Figure 6.6: The spectral profiles of the GVD and confinement losses for the fundamental mode (0) and the third higher-order mode (3) of the MOF with regular cladding. Zero GVDs take place at 870 nm for the fundamental mode (0), and at 600 nm and 1064 nm for the third higher-order mode (3). Confinement losses of the fundamental mode do not exceed 2x10-5 dB/m in the presented wavelength range.

Then, the dispersion and confined loss spectral properties were calculated for the fiber with symmetric geometry of the cladding. Figure 6.6 shows the calculated spectral profiles of the GVD and confinement losses for the fundamental LP01 mode (0) of the mentioned fiber. Now, in contrast to the fiber with irregular cladding, the transversal components of the electromagnetic field of the first and the second higher-order modes (in the terminology of paper [103]) of the MOF with regular cladding are described by the odd functions with respect to the center of the fiber. As a result, these modes can not be excited with the use of the symmetric excitation scheme used in our experiments (see below). So, we calculated the spectral profiles of the GVD and the confinement losses for the third higher-order LP02 mode (mode 3)

of the MOF with regular cladding, which is effectively excited because it has the same symmetry of the field, as the fundamental mode (see Fig. 6.7) [99], [103]. These data are also shown in Fig. 6.6. The predicted zero GVD for the fundamental mode was equal to 870 nm, and the confinement losses do not exceed 2x10-5 dB/m across the whole simulated band. Unlike in the fiber with irregular cladding, the higher-order mode demonstrates neglible confinement losses at wavelength below 1000 nm that can be considered as cut-off wavelength for this mode. The corresponding dispersion profile possesses the concave shape and crosses the line of zero dispersion twice at 600 nm and 1064 nm. Figure 6.7 shows the calculated intensity profiles for the fundamental and the third higher-order modes of the MOF with regular cladding. Fig. 6.8 ilustrates the wavelength dependencies of the effective mode area A_{eff} and the nonlinear parameter γ of the fundamental and the third higher-order modes for the MOF with regular cladding.

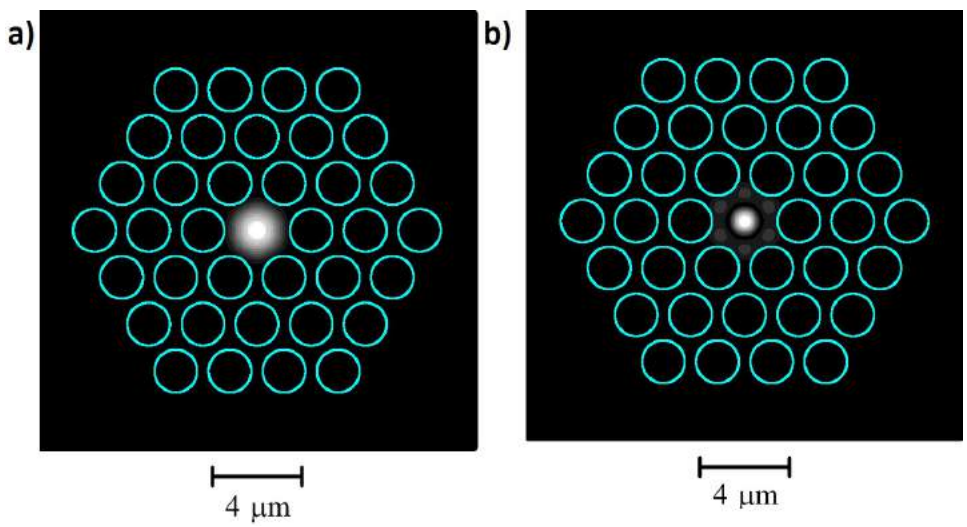

Figure 6.7: Calculated intensity profiles of the fundamental mode at 870 nm (a) and the third higher-order mode at 600 nm (b) of the MOF with regular cladding.

6.4 Supercontinuum generation in the fabricated fibers

The supercontinuum (SC) spectral broadening was carried out with a tunable Ti:Sapphire laser (MAITAI HP) with 100-fs pulses and a 80-MHz repetition rate. The center wavelength of such a laser can be tuned continuously

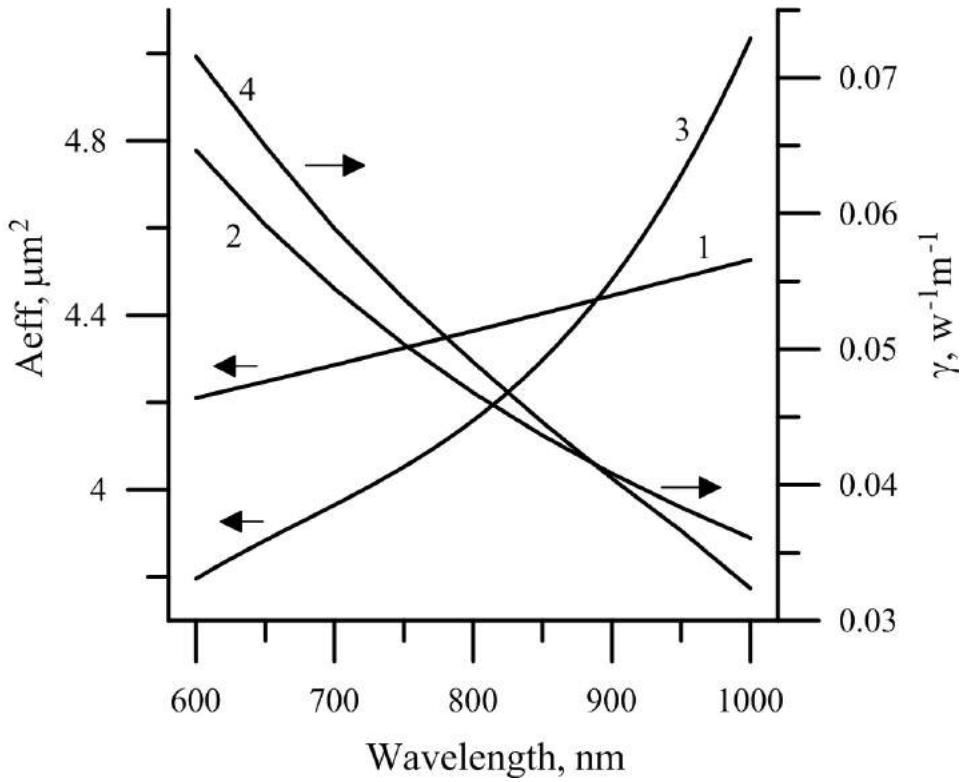

Figure 6.8: The spectral profiles of the effective area A_{eff} (1, 3) and nonlinear parameter γ (2, 4) of modes for the MOF with regular cladding. Curves 1 and 2 refer to the fundamental mode, curves 3 and 4 refer to the third higher-order mode.

between 700 and 1040 nm. The average power of the coupled pulses was constant; it was set to 56 mW for each wavelength used. The length of the MOFs used in the experiments was roughly 1 m. The schematic representation of our measurement setup is shown in Fig. 6.9.

The femtosecond pulses from a Ti:Sapphire laser were coupled into the fibers under test using a collimator and a matching 25X microscope objective. The generated SC spectra were monitored with an Agilent 86142B Optical Spectrum Analyzer (OSA) that provides detection in the 600 - 1650 nm wavelength range with an average resolution of 1.0 nm. Additionally, we recorded the transversal power profile of the output beam at the far-field zone using a CCD camera operating in the visible band. For each fiber sample, we recorded SC spectra seeded by the laser with center wavelength swept between 700 nm and 1040 nm in 10-nm steps. Figure 6.10 and Fig.

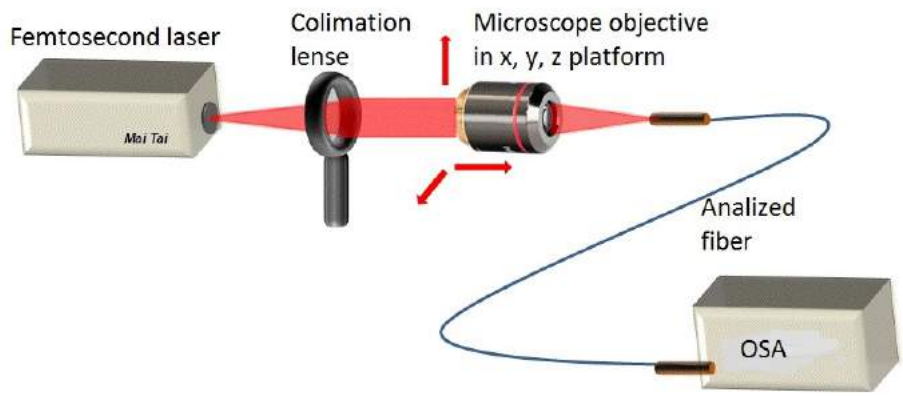

Figure 6.9: Schematic of the experimental setup used for supercontinuum generation in the fabricated MOFs.

6.11 show SC spectra generated in the fiber with irregular cladding.

It can be observed that for all pumping wavelengths, the SC spanned over the full wavelength range of the OSA used, and it exceeded an octave. Figure 6.12 shows the corresponding far-field distributions for the pumping wavelengths indicated in the figure. Such distributions were recorded with a CCD camera. It can bee seen from Figs. 6.10, 6.11 and 6.12 that at 750 nm and at 800 nm pumping wavelengths, we have the broadband supercontinuum spectra ranging from visual wavelengths up to 1650 nm. Also note that the supercontinuum was also generated when the pumping wavelength was 700 nm, but it was not asspectrally efficient (flattened) as the SC when pumping wavelengths were 750 nm or 800 nm.

We can note in Figs. 6.4(b), 6.12(a), 6.12(b), and 6.12(c) that far-field images observed in the IG MOF with irregular cladding when it is pumped at 700 nm, 750 nm, and 800 nm are similar to the intensity distribution of the first high-order mode. From such figures, we can conclude that the first higher-order mode is a pumping mode of the MOF in the wavelengths range from 700 nm to 800 nm, where its confinement losses do not exceed 17.2 dB/m (see Fig. 6.3). It is also important to note that the zero GVD of the first high-order mode for the aforementioned fiber takes place at wavelength of 740.4 nm.

As one can see in Fig. 6.3, the confinement losses of the first high-order mode are high enough in the wavelength range from 700 nm to 800 nm

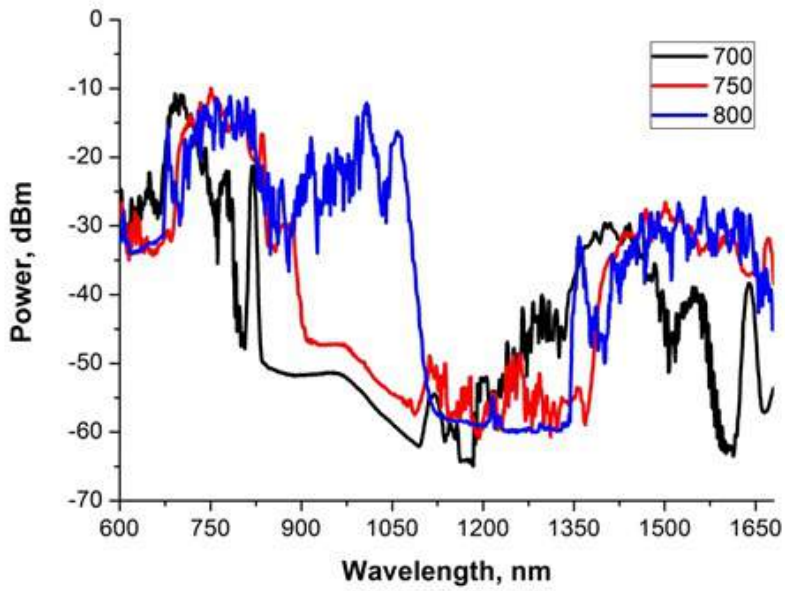

Figure 6.10: Supercontinuum spectra for the IG MOF with irregular cladding obtained when the pumping was a femtosecond Ti:Sapphire laser emitting at 700 nm, 750 nm, and 800 nm.

(the range of losses is 7.9-17.2 dB/m). As a result, this mode can reach the output end of the MOF with a length of 1 m with low power in the linear regime of propagation and the fiber is a really single-mode fiber. In order to explain the experimental data shown in Figs. 6.10, 6.11 and 6.12, it is reasonable to assume that upon the excitation of the first higher-order mode by high power ultra short laser pulses with wavelengths a little higher than zero GVD, the mode propagates in the anomalous dispersion regime, generating a supercontinuum based on the soliton fission mechanism [104], [105].

The soliton fissing in this case most likely happens for all pumping wavelengths; otherwise, the long-wavelength tail of SC will not appear. What we wanted to emphasize is that the SC spectrum for 700 and 750 nm pumps contains higher powers within 600-900 nm band than the other parts of the spectrum. Since the mode profiles of the MOF with random holes is not fully symmetrical, the overlap between the first high-order mode pump and higher-order modes of the newly created harmonics could be significant. It is reasonable to assume that the other nonlinear mechanisms such as self

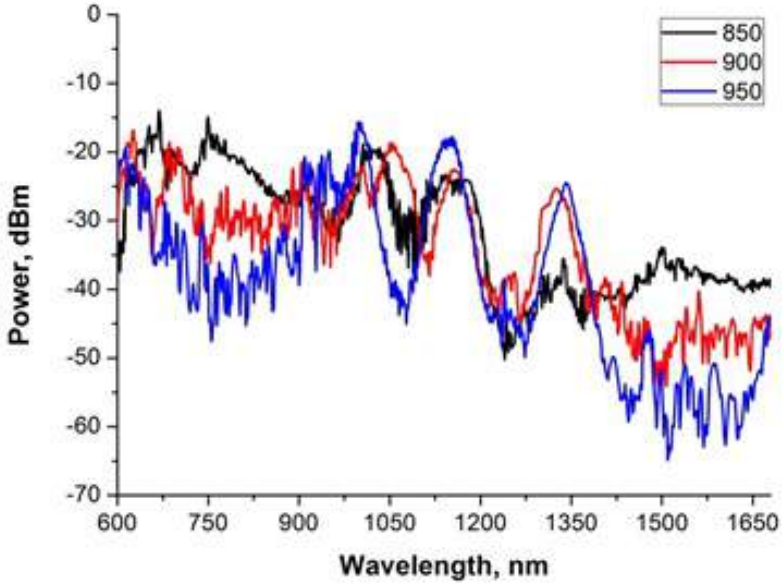

Figure 6.11: Supercontinuum spectra for the IG MOF with irregular cladding obtained when the pumping was a femtosecond Ti:Sapphire laser emitting at 850 nm, 900 nm, and 950 nm.

phase modulation, phase-matched four-wave mixing, modulation instability are involved to the process of SC generation since the numerically predicted zero GVD is sitting close to the pump wavelength. At the same time, the middle part of the spectrum [Fig. 6.10] is highly suppresses and does not match the typical flattened spectrum generated by means of soliton fission. We suppose that the long-wavelength part (>1200 nm) can be partly attributed to the phase matched "copy" of the energetic part of the SC. Also, we can see in Fig. 6.11 that at 850 nm and 900 nm pumping, we have the broadband supercontinuum spectrum in the wavelength range from visual wavelengths to 1650 nm; at 950, the supercontinua also exist, but they are not as spectrally efficient as at 850 nm and 900 nm pumping.

We wanted to emphasize a fact that power of 850 nm and 900 nm pump is tranferred more effective over the whole spectrum and is not localized at certain spectral windows.

We also can see in Figs. 6.4(a), 6.12(d), 6.12(e) and 6.12(f) that far-field images obtained when the IG MOF with irregular cladding was pumped

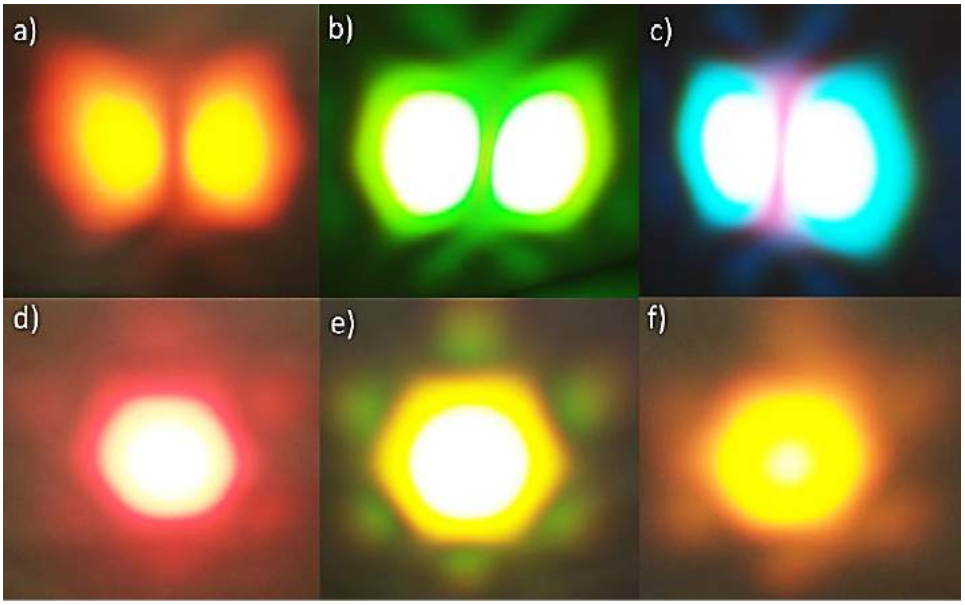

Figure 6.12: Photographs of far-field images obtained with the IG MOF with irregular cladding with length of 1 m. The pumping source was a femtosecond Ti:Sapphire laser with wavelengths: a) 700 nm, b) 750 nm, c) 800 nm, d) 850nm, e) 900nm, f) 950nm.

at 850 nm, 900 nm and 950 nm are like the intensity distribution of the fundamental fiber mode. It follows from these figures that in this case, only the fundamental modes (1) and (2) of the fiber with zero GVDs, respectively, at 897 nm and 893 nm (see Fig. 6.2) are the pumping modes of the IG MOF with irregular cladding. The GVD and confinement losses of the first higher-order mode of such a fiber are very high at wavelength values greater than 800 nm, see Fig. 6.3. So, a supercontinuum generation for the first higher-order mode becomes impossible in this case. Figure 6.13 shows supercontinuum spectra for the IG MOF with regular cladding, obtained by means of pumping the fiber at wavelengths of 850 nm, 900 nm, 950 nm and 1000 nm.

As it can be seen in Fig. 6.5, zero GVDs for the quoted fiber take place at 870 nm for the fundamental mode, at 600 nm and at 1064 nm for the third high-order mode, respectively. It can be noted that the behavior of the fiber with regular cladding is different from that of the fiber with irregular cladding. In spite of the fact that the IG MOF with regular cladding is a multimode fiber in the linear regime of transmission, only the fundamental mode with a zero GVD at 870 nm is the pumping mode in the second fiber.

Due to the symmetry of the MOF, only mode 3, among all higher-order modes, can be effectively excited and generate a supercontinuum.

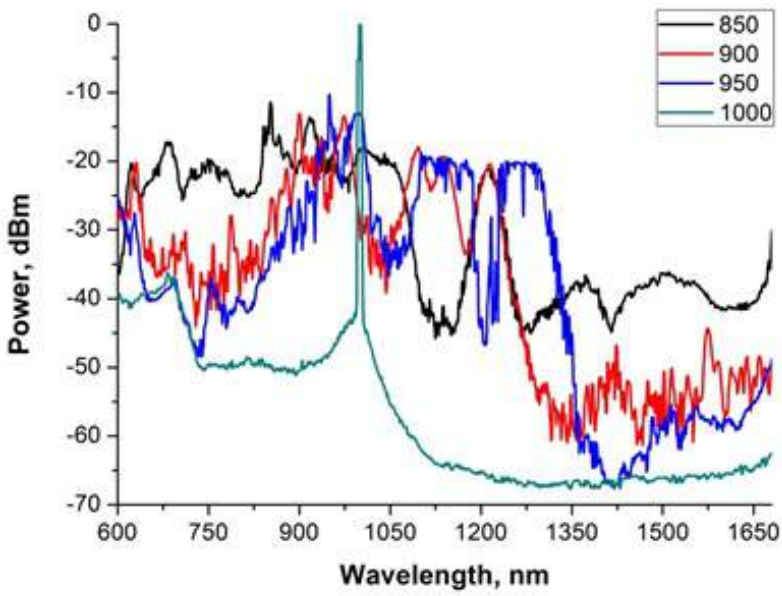

Figure 6.13: Supercontinuum spectra observed in the IG MOF with regular cladding for pumping wavelengths of 850, 900, 950 and 1000 nm. Zero GVD for the fundamental mode takes place at 870nm.

The absence of this effect in our case may be explained by the sharp wavelength dependence of GVD for this mode, see Fig. 6.6. At 850 nm pumping we have the broadband supercontinuum spectrum in the wavelength range from 600 to 1650 nm. The spectrum has higher intensity at wavelengths of 600-1070 nm and wavelengths of 1200-1650 nm. At 900 and 950 nm pumping, we also have the broadband supercontinuum spectra in the wavelength range from 600 to 1650 nm; but the spectra are not as spectrally flattened as at 850 nm pumping. We can also see in Fig. 6.13 that broadband supercontinuum generation does not happen at wavelengths higher than 950 nm, due to a high GVD of the fundamental mode for the MOF with regular cladding at these wavelengths, see Fig. 6.6.

6.5 Conclusion

In this work, we report on the fabrication of special (3 number of air-hole rings) nonlinear, index guiding air-silica microstructured fibers with regular and irregular claddings. A single-mode fiber with irregular cladding and a multimode fiber with regular cladding were fabricated. The structure of the modes and dispersion properties of these fibers were numerically predicted and experimentally verified. Broadband supercontinuum generation from visual wavelengths up to 1600 nm in such fibers, both with the length of 1 m, was observed. We experimentally proved that the supercontinuum bandwidth can be significantly extended in the MOF with irregular cladding, since the such fiber supported effective nonlinear coversion both to the fundamental and to the higher order mode. Optimal pumping conditions were identified by tuning the center wavelength of the pump. The optimum pump wavelengths agreed well with the ZDWs obtained from numerical analysis.

Chapter 7

Polymer optical fibers

7.1 Introduction

At present, Polymer optical fibers (POFs) have a lot of applications, especially in short-distance communication systems, in the automotive industry [106, 107], and also in special sensing devices [106, 107, 108], due to their high flexibility and low stiffness in comparison to those of glass fibers. Attenuation in optical fibers is one of the most important parameters, and it is necessary to have in mind that POFs have significantly greater attenuation than conventional glass or silica fibers (about 150 dB/km in POFs, while only about 0.2 dB/km in glass fibers, respectively, at the optical communication window). A nondestructive scheme for measuring attenuation in POFs has been recently reported [109].

7.2 Conventional polymer optical fibers

The most commonly used conventional POFs with an outside diameter of 1 mm, for the car building industry, are fabricated from PolyMethyl MethAcrylate (PMMA), which is a transparent thermoplastic material [110]; fluorinated PMMA, polycarbonates, polystirene, and some silicones are also used in the fabrication of POFs, but PMMA is the most commonly used polymer for POFs, since it is the most transparent polymer and has low cost.

7.3 Design and fabrication of microstructured polymer optical fibers (mPOF)

After the first demonstration in 1996 of a silica microstructured (or photonic crystal) fiber (mPOF)[19], it was quickly realized that a variety of PCF optical properties could be achieved through diverse materials used. The first nonsilica PCFs were fabricated using PMMA [111].

The change to polymers had significant potential, given the range of polymers and processing methods available, along with the low processing temperatures, which would allow organic and inorganic dopants to be used that would not otherwise survive the higher processing temperatures of silica. The preforms to fabricate mPOF can be fabricated by means of extrusion [111, 110, 112], stacking [113], casting/molding [114], billet extrusion [115] and solvent deposition [116], and the properties of polymers are crucial for the success of some of these methods. In the experimental part we fabricated mPOF by extrusion and stacking, two of the most used methods nowadays.

One of the advantages of a polymer optical fiber drawing tower is that the furnace has a large inside diameter, about 70 mm, compared to the 27 mm of the furnace for silica fibers, and it is possible to fabricate fibers or canes with a relative large diameter of preforms, tubes or rods. Another advantage of the Polymer drawing tower is the fact that the temperature is not so high, and it is not necessary to use an inert gas into the furnace. Consequently, drawing becomes the most economical process.

Extrusion was the first method employed to fabricate mPOF [111]. It allows a variety of mPOF designs. Hole positions are not restricted to the hexagonal arrangement that is typical for stacked preforms, leading to the first nonhexagonal microstructured fiber, a ring-structured fiber with the holes placed in concentric circles [112].

Once the preform is completed, it can be drawn to a cane or a fiber. Drawing must be done above the glass transition temperature (Tg) of the material.

Extensive modelling of the draw process of microstructured fibers has identified the role of various process parameters and material properties, such as draw rates, viscosity and surface tension. As a result, a large range of behaviors, such as hole expansion or hole collapse, can be achieved solely by varying the draw conditions and without the use of pressure [117, 117, 118, 119, 120].

7.3.1 Drawing tower for PMMA fiber

In figure 7.1, we show a picture of the drawing tower in Bilbao, Spain. Where I passed my predoctoral practices. This is a drawing tower, fabricated in Finland. On the top the preform feeder, it is possible to see a mechanism that slowly feeds the preform, the PMMA rods or tubes into the furnace. This drawing tower has a possibility of rotation of the preform feeder, a very useful tool for fabrication of twisted fibers.

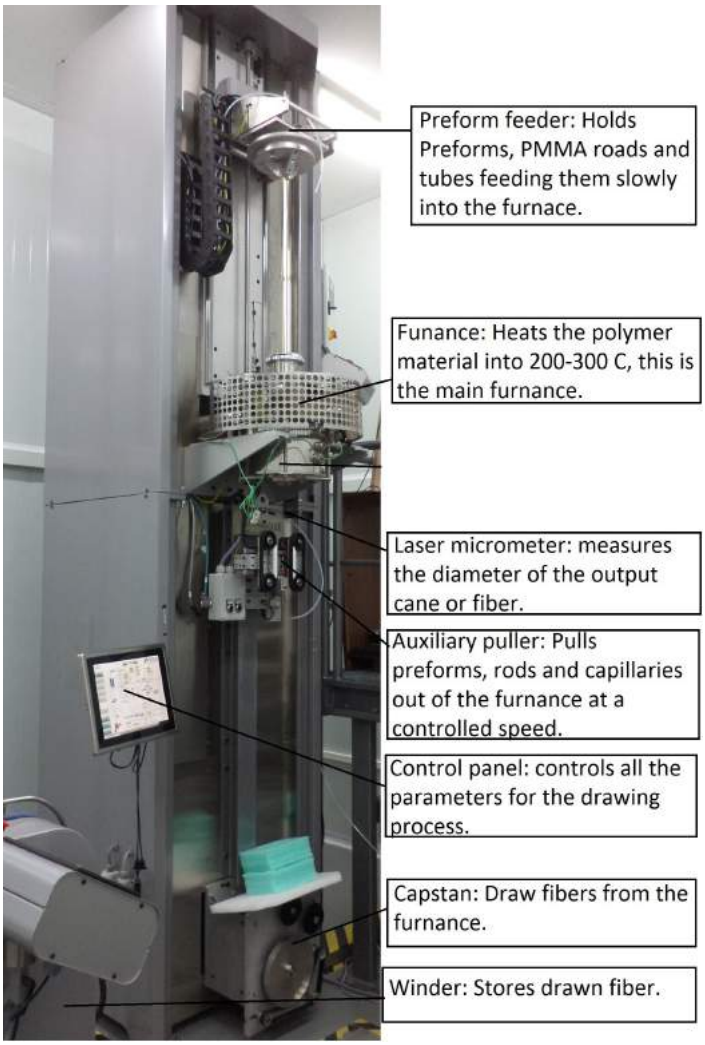

Figure 7.1: Drawing tower at the Basque University, campus Leioa, Bilbao, Spain. Parts and assignations.

There is a special furnace where a preform is heated. The melting of the PMMA preforms hapens at a temperature of about 230-250 °C, and we worked in this range of temperatures.

Immediately after the furnace, the laser micrometer is placed, which makes the diameter measurement of the fiber in two perpendicular axis, and shows these parameters in the control panel. The capstan draws the fibers from the furnace, but it is impossible to use this part of the equipment for canes or tubes with large diameters; this mechanism is only for the fiber drawing process.

The last part of this tower is the winder, which stores the drawn fiber.

This design of a drawing tower has a very modern control system, through a touch screen where it is possible to control all the process. This control panel is shown in the figure 7.2.

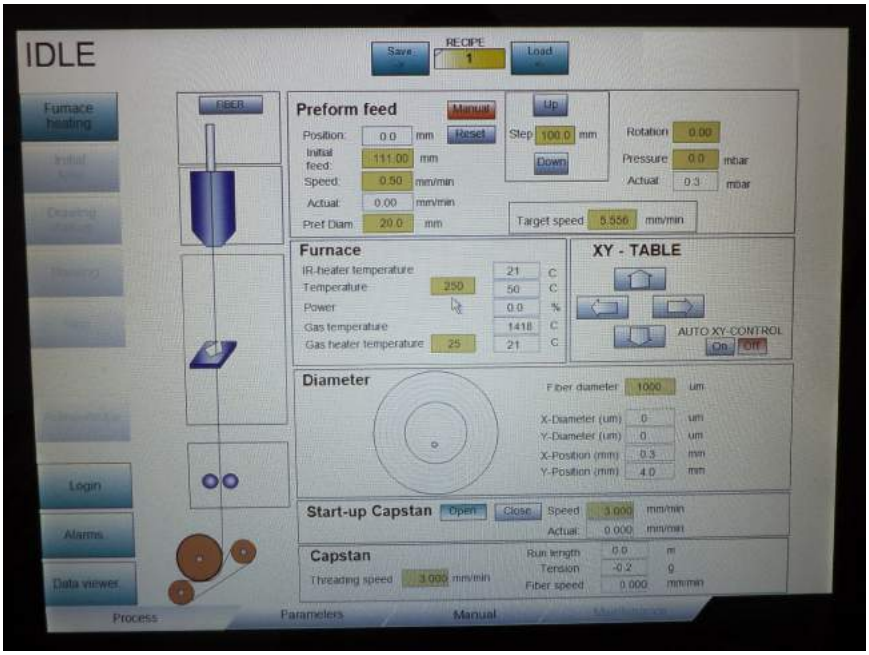

Figure 7.2: Control panel of drawing tower in Leioa, Vasque Country, Spain.

7.3.2 Fabrication of mPOF by extrusion

A very easy way to fabricate the preform in order to obtain a microstructured Polymer Optical Fiber is by fabricating the holes in a relatively large diameter rod (in our case, about 50 mm of outer diameter). Due to the physical characteristics of the PMMA, this material is friendly enough for air-hole fabrication, obtaining a sufficiently acceptable surface roughness.

Let see the advantages of this method:

- For this method, intercapillary spaces do not exist, and due to this fact, it is possible to obtain more regular structures.
- It is not necessary to put each capillary into a special hexagonal shape.
- It is not necessary to put filling rods at the edge, between the capillaries and the external tube.
- It is possible to obtain a very different shapes and number of holes around the core, and also it is possible to fabricate different diameters of air-hole in the same preform.

In figure 7.3a, it is possible to see an extrusion preform ready to be drawn into a mPOF; as we can see at the top, the holes are visible, but the length of the preform is not too large. In figure 7.3b, it is possible to see the transversal cut image of the fiber obtained from this preform. In this picture, it is seen that the roughness of the surface is very visible, and because of that, we did some reseach about end termination methods for polymer optical fibers in this chapter [8]. In the figure 7.3c, it is possible to see the mPOF obtained from the 3 ring preform that is shown in the figure 7.3a. In the figure 7.3d, we can see a fiber fabricated with very high pressure; it is a deformed fibers, in which the external part is not circular as it should be.

Also, about the losses in this fiber, it is important to say that they are very high, about 1000 dB/km at a wavelength of 650 nm.

7.3.3 Fabrication of mPOF by stacking

In this process, we did the capillary stacking as we had done before for glass fibers, but here we used larger diameters for capillaries, about 8 mm of outer diameter, and the outer/inner diameter ratio was 0,5. In figure 7.4 we show different stages of the stacking process: a) hexagonal structure, b) circular

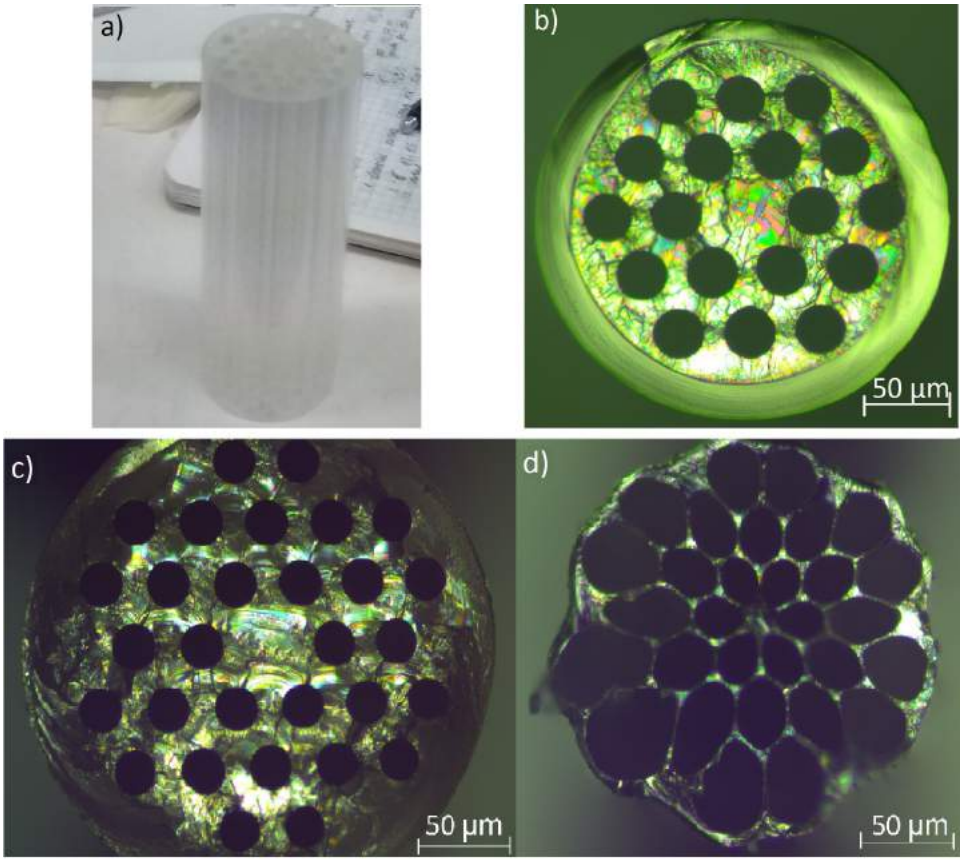

Figure 7.3: a) 3 ring Preform fabricated by extrusion, b) 2-ring mPOF obtained from the extrusion preform, c) 3-ring mPOF from the extrusion preform, d) 3-ring mPOF obtained with very high pressure applied into the structure.

structure, ready to be put into the large tube, c) and d) a preform ready to be drawn.

7.4 End termination methods to cut polymer optical fibers [8]

Attenuation in POFs is one of most important parameters, and usually measured through the use of the cut-back method [121]. In this case, the fiber end face preparation is of great importance. The following conventional methods for preparing POF end faces have been developed [106]:

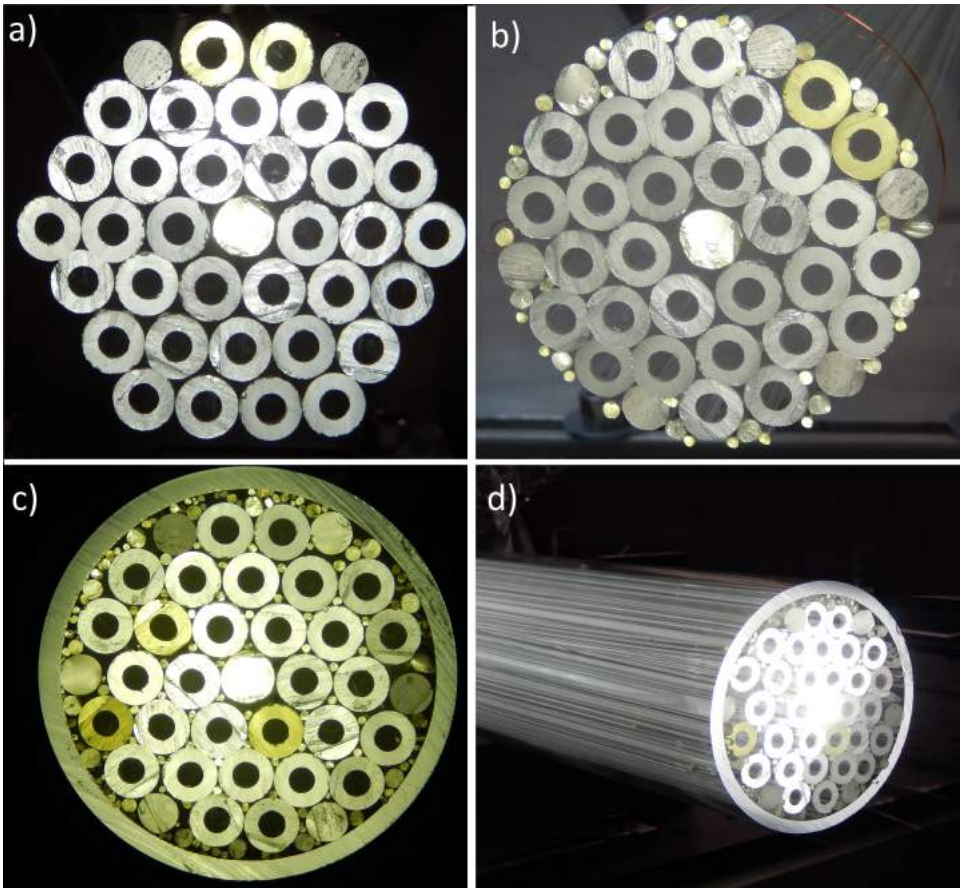

Figure 7.4: a) hexagonal structure, b) circular structure ready to put into the large tube, c) and d) a preform ready to be drawn.

1. Cutting at a perpendicular angle and polishing with a sand paper;
2. Simple cutting with a thin blade (usually once for a single cut);
3. Hot-plate POF end face preparation, when, after cutting, the fiber is additionally pressed against a hot mirror;
4. Laser cutting;
5. Microtome cut;
6. Press and cut, when a suitable radial pressure is applied to the fiber before cutting.

The existing conventional methods of POF end face preparation yield an insertion loss for one POF end surface of about 0.24-0.68 dB. The problem is that some of these techniques are time-consuming and costly, depend on the skills of the operator, and do not give POF end faces that are sufficiently identical. It is necessary to point out that it is likely that excellent results at preparing POF end faces via hot razor-blade/hot-fiber cleaving techniques have been obtained lately for multimode graded-index microstructured POFs with outside diameters of 400 μm [122, 123], as well as for single-mode microstructured POFs with outside diameters of 125 μm and 280 μm [124]. Unfortunately, any information about attenuation in used fibers and also information about insertion losses for fabricated POF end faces is absent in these articles. Figure 7.5 shows a fault end termination of a conventional POF.

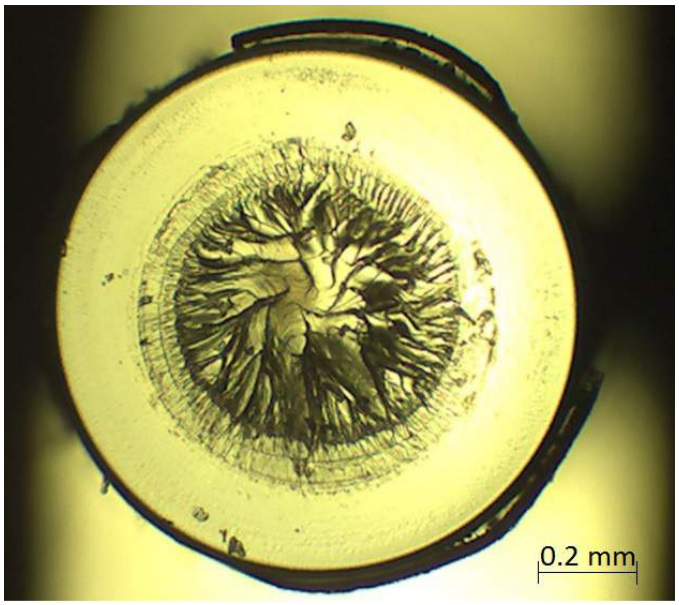

Figure 7.5: Fault end termination of a conventional POF.

7.5 Polymer optical fiber end termination with use of liquid nitrogen

The main idea here is to prove that we can obtain low insertion loss with a new technique that produces practically identical POF end faces. For preparing POF end faces, we propose the use of the score-and-break or the scribe-and-break methods, which are the basic methods for preparing identical enough end faces in glass optical fibers [125, 126]. We think that if we briefly cool POFs with liquid nitrogen or liquid nitrogen vapor at temperatures lower than -50°C, we can suppress elastic POF properties. Then it will be possible to use the above-mentioned scribe-and-break method for preparing POF end faces. The step index POFs employed in our experiments were fabricated in our laboratories, and consist of a polymethyl methacrylate (PMMA) core with a diameter of 0.96 mm and a single cladding from fluoro-acrylate with an outside diameter of 1.0 mm. The refractive index of the PMMA core is 1.49, the refractive index of the cladding is about 1.4 at 650 nm. Figure 7.6 shows measurement results of attenuation in our fiber and in a Mitsubishi commercial fiber CK for a wavelength range of 450-700 nm; we used the cut-back method in our measurements. POFs with a length of about 130 m were the ones employed. POF end faces were prepared by using the hot-plate method.

In figure 7.6, we can see that our fiber has less attenuation than the Mitsubishi fiber CK40. To compare the proposed scribe-and-break method of preparing POF end faces with the existing conventional methods for POF end termination, we also fabricated conventional POF end faces with RPsingle-cut guillotines [112], using a cutting instrument from Rennsteig Werkzeuge GmbH Co. [112], and also with a hot-plate. A schematic view of the proposed scribe-and-break method for preparing POF end faces is presented in figure 7.7

We prepared POF end faces with this method in the following way. Initially, a scratch was circumferentially made around the fiber at laboratory temperature of about 25°C using a RPsingle-cut guillotine. Then, the fiber was fixed at two edges of a thermos containing liquid nitrogen, and was allowed to cool for about 15 seconds in the liquid nitrogen or in a liquid nitrogen vapor. Using a curved form with a 2.7-cm radius, perpendicular POF fractures with no visible defects were produced by moving the curved form down, see figure 7.7; for reference, we also broke the fiber without using liquid nitrogen. Of course, it is not possible to break non-refrigerated POF

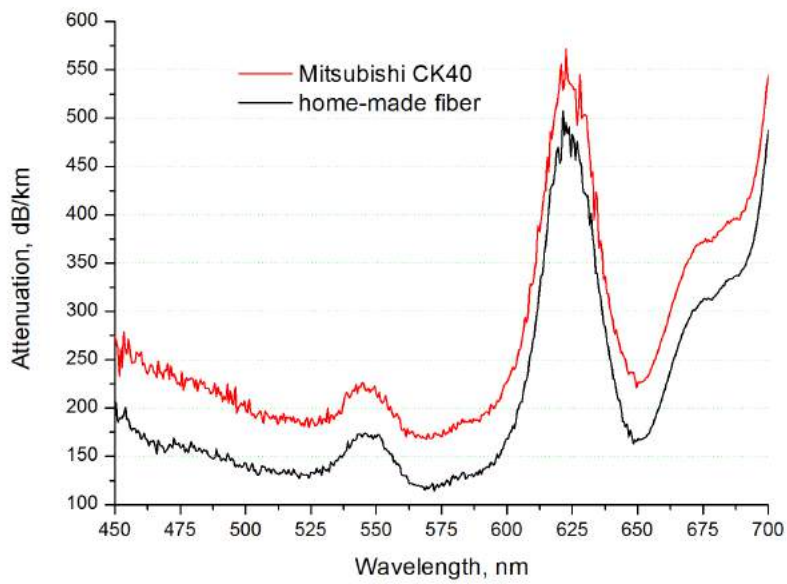

Figure 7.6: Comparison of attenuation of out home-made fiber with Mitsubishi CK40.

using the 2.7-cm radius curved form, so we broke it by decreasing the fiber bending radius until the fiber broke.

Measurement of insertion loss was carried out according to standard IEC 61300-3-4. A measurement setup in accordance with this method consists of a light source, a mode filter, an investigated POF and a power meter. We used an AQ4335 white light source to launch light into the mode filter. A piece of the aforementioned POF, with polished end faces and with a length of about 60 m, wound on a spool with a diameter of 154 mm, was used as the mode filter. Investigated POFs with lengths of 0.5 m and an AQ-6315A optical spectrum analyzer as a power meter were used in our measurements; preliminary, end faces of the investigated fibers were also prepared by polishing. The measurement was performed in two steps: the first step consisted in obtaining a reference spectrum at the mode filter output, and the second step consisted in obtaining the spectra at the investigated fibers outputs. Before carrying out the every second step, we connected the output end face of the filter with an input end face of every investigated fiber into a joint by using connectors having special elements to fix the fiber in needed position inside the connectors. A drop of a Cargille oil with a refractive

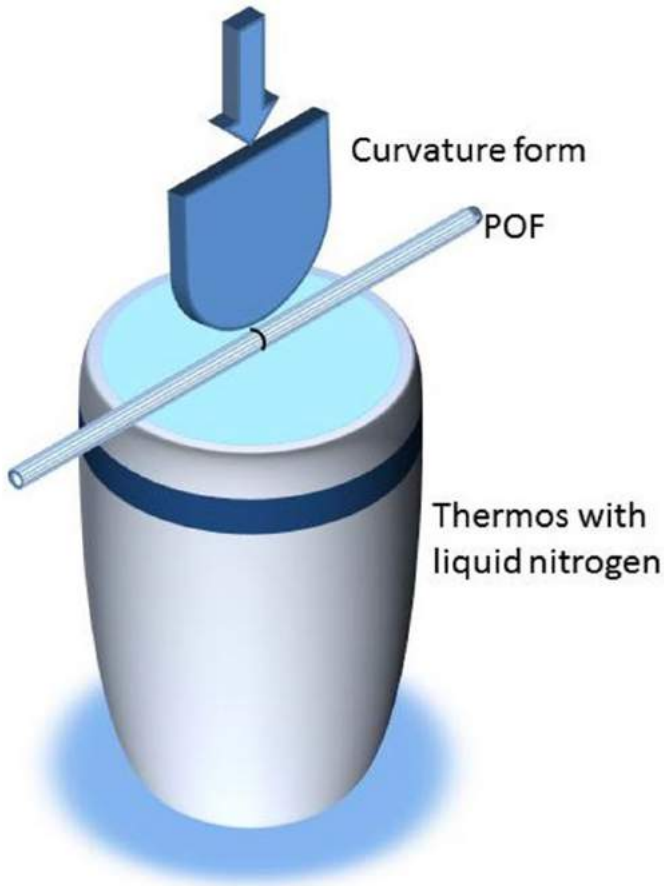

Figure 7.7: Scheme of the proposed POF end face preparation by the scribe-and-break method

index of 1.49 was then added between the end faces of the connected fibers. We assumed that we had a very small loss in the joint when we had an additional loss of 0.31 dB (at 650 nm) at the output of the investigated fiber (the output POF end surface yielded an insertion loss of about 0.25 dB for a polished end face, plus a loss of 0.06 dB within an investigated piece of the POF with the length of 0.5 m). After the calibration of the setup we measured insertion losses for different prepared POF end faces. Figure 7.8 shows insertion loss in a wavelength range of 450-700 nm for POF end faces prepared using different termination methods.

We can see in figure 7.8 that the insertion loss for faces prepared with conventional RPsingle-cut guillotines is 0.55 dB at 650 nm. For faces obtained

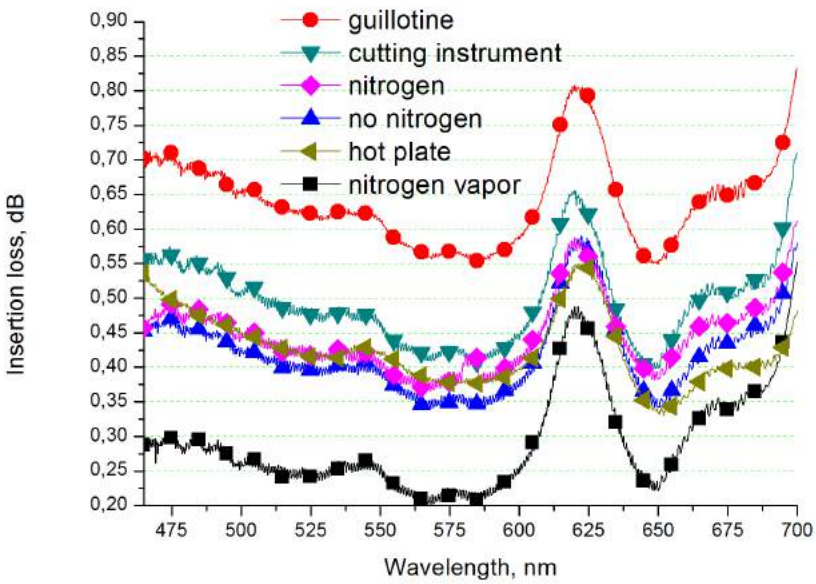

Figure 7.8: Insertion loss for POF end faces prepared with different methods.

by POF breaking without using liquid nitrogen, the loss is 0.53 dB. For faces prepared with a hot-plate, the loss is 0.33 dB. We also obtained an insertion loss of 0.4 dB for POF faces fabricated with the conventional Reinnsteig Werkzeuge GmbH Co. cutting instrument, of 0.38 dB for faces fabricated in liquid nitrogen, and of about 0.22 dB for faces fabricated in liquid nitrogen vapor. It is possible to conclude from these data that the proposed method of POF face preparation yield lower insertion loss than the conventionally used methods of POF preparation. We also looked into the quality and perpendicularity of the fracture surfaces obtained using liquid nitrogen and without using it. A National DC-163 digital optical microscope and an atomic force microscope (AFM) with a resolution of 50 nm for 30x30 μm images were used in this research effort. Figure 7.9 shows the image of a POF fracture surface obtained in liquid nitrogen [figure 7.9(a)] and the image of the best POF fracture surface obtained under normal environmental conditions [figure 7.9(b)]. The images were prepared by means of the aforementioned optical microscope.

It is seen in figure 7.9 that it is difficult to evaluate the quality of these

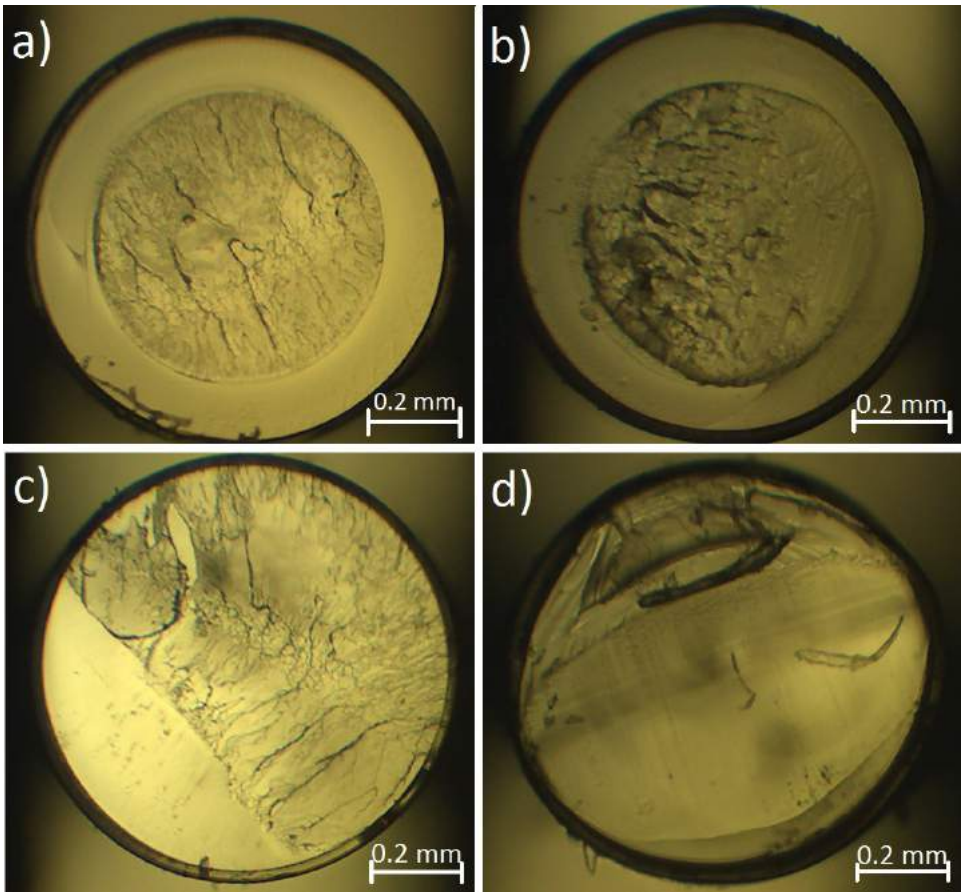

Figure 7.9: POF fracture surfaces obtained: a) in normal environmental conditions (surface 2), b) in liquid nitrogen (surface 1), c) simple cutting with a thin blade and d) with the conventional Reinnsteig Werkzeuge GmbH Co. cutting instrument.

fracture surfaces visually. That is why we analyzed the surfaces with the atomic force microscope (AFM). Figures 7.10 and 7.11 show relief of the POF fracture surfaces shown in figure 7.9(a) and in figure 7.9(b), respectively.

These figures present the relief in the centers of the POF fracture surfaces. We also analyzed relief of the surfaces in intermediate zones, and in a zone near the edge of the fiber. Results of our measurements are presented in Table 7.1. We can see in Table 7.1 that the surface relief of the POF face fabricated with use of liquid nitrogen is 2 or 3 times smaller than the relief of the face fabricated under normal environmental conditions.

Of course, the relief in the zone near the edge of the POF fibers is almost

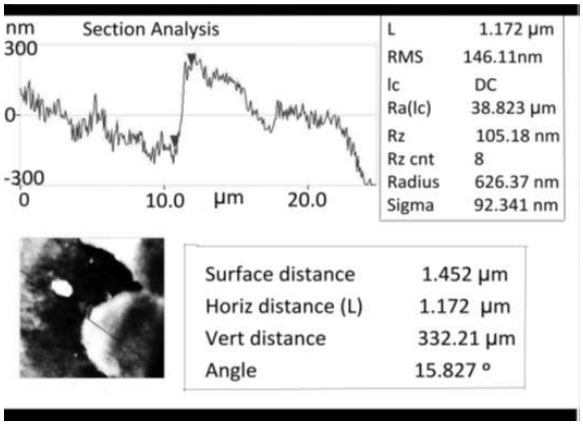

Figure 7.10: Relief of POF fracture fabricated in liquid nitrogen.

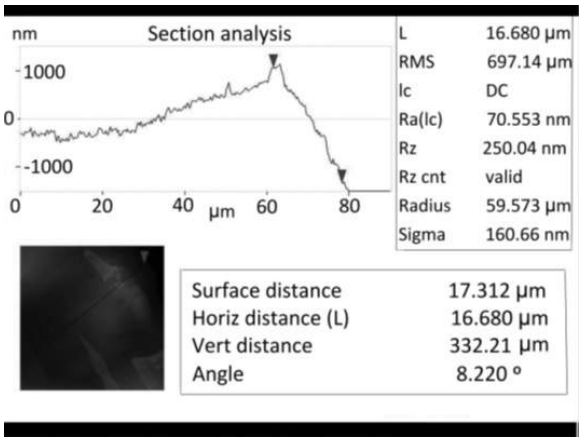

Figure 7.11: Relief of POF fracture fabricated in normal environmental conditions.

the same, due to the fact that the same guillotine was used to make circumferential scratches. We also decided, upon preparing POF faces with the scribe-and-break method, not to put the fibers into liquid nitrogen, but only to expose them to a liquid nitrogen vapor. The experiment was performed with the POFs positioned at 5-10 mm above the liquid nitrogen level in a thermos; we kept the fibers in the liquid nitrogen vapor for periods of 10, 15, 20 and 30 seconds, and the time of exposure determines the temperature of the fibers at breaking. We then broke the POFs using the same 2.7 cm radius curved form. Figure 7.12 shows results of insertion loss measurements for the fabricated POF end faces. We can see in figure 7.12 that the insertion loss is lower when the fibers are exposed to the liquid nitrogen

Surface No.	Center	Intermediate zone	Zone near edge
Surface 1	0.33-1.16 μm	1.85 μm	0.65 μm
Surface 2	2.41 μm	2.49-3.49 μm	0.68 μm

Table 7.1: Relief of the investigated fracture surfaces obtained with AFM.

vapor for about 10-15 seconds. It seems that in this case, the POF breaking temperatures are the optimal ones for POFs on a base of PMMA.

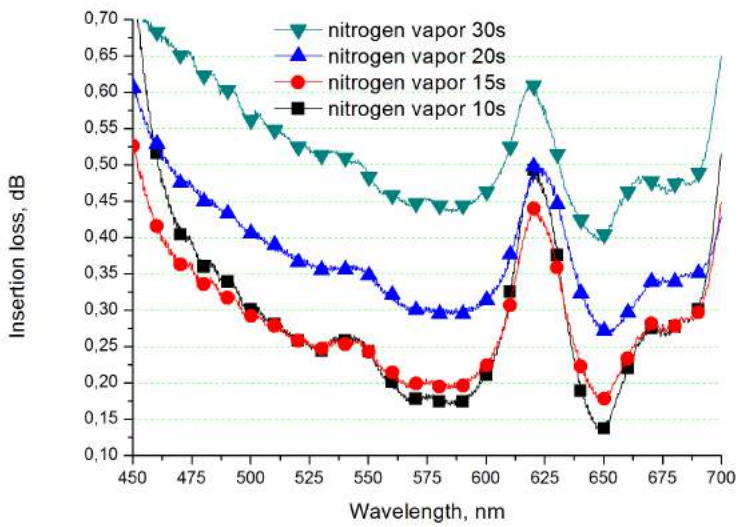

Figure 7.12: Insertion loss for POF faces fabricated at different times of exposure to liquid nitrogen vapor.

Figure 7.13 shows images obtained with the digital optical microscope of POF fracture surfaces that were fabricated in liquid nitrogen vapor after an exposure time of 15 sec [figure 7.13(a)], and of POF fracture surfaces fabricated with a conventional hotplate method [figure 7.13(b)].

In this case, we have found that the insertion loss for POF faces fabricated in liquid nitrogen vapor is smaller than for POF faces fabricated with the hot-plate method and is comparable to the loss of polished faces. Also, using the POF scribe-and-break method proposed here, we found the insertion loss to be mainly less than of 0.2 dB, in the 20 breaks we prepared. So, using this POF end face preparation method we obtained a high repetition of insertion loss.

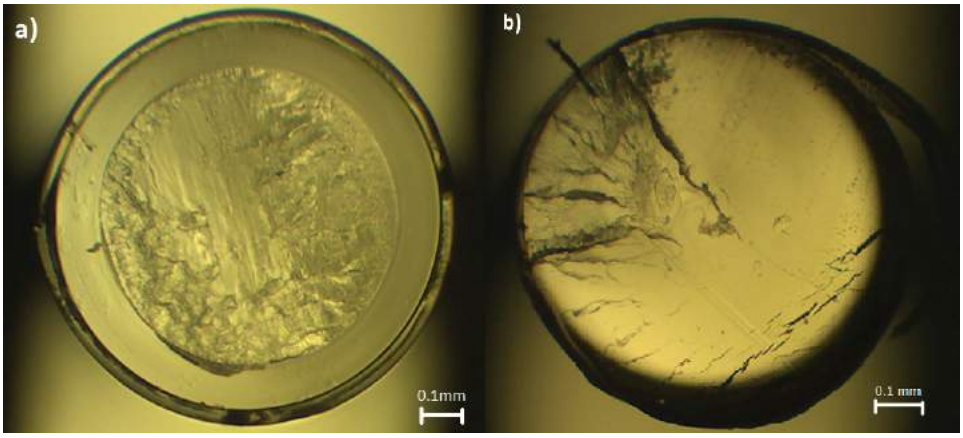

Figure 7.13: POF fracture surfaces fabricated (a) in liquid nitrogen vapor after being exposed to the vapor for 15 seconds, (b) with a hot-plate method.

7.6 Conclusion

In conclusion, we have demonstrated a new method of POF end face preparation. It includes preparing a scratch circumferentially made around the fiber at temperature of about 25°C, cooling the fiber for a short time in liquid nitrogen or liquid nitrogen vapor, and breaking the fiber using a special curved form. Perpendicular fractures for a home-made step index POF, which consists of a PMMA core with a diameter of 0.96 mm, and a single cladding from fluoro-acrylate with an outside diameter of 1.0 mm, were prepared with the 2.7-cm radius curved form. The insertion loss for the fabricated POF end faces was measured, and for comparison, we also measured the insertion loss for the POF end faces fabricated using conventional methods for POF end face preparation. We have found that by using the proposed method of POF end face preparation, it is possible to fabricate the POF end faces with an insertion loss of about 0.2 dB, which is less than the loss when using the now existing methods for POF end face preparation. We have also obtained a high reproducibility in insertion loss for POF end faces fabricated using the newly proposed method. We also believe that the proposed method will find a wide application for preparing end faces of POFs with a thinner core than what we used, and also for preparing end faces of microstructured POFs.

Bibliography

[1] John A Buck. *Fundamentals of optical fibers*. John Wiley & Sons, 2004.

[2] Stamatios V Kartalopoulos. *DWDM: networks, devices, and technology*. Wiley-IEEE Press, 2003.

[3] Jeff Hecht. *Understanding fiber optics*. Jeff Hecht, 2015.

[4] Eric Udd. Fiber optic sensors based on the sagnac interferometer and passive ring resonator. In *Fiber Optic Sensors: An Introduction for Engineers and Scientists*. John Wiley & Sons, 1991.

[5] M Vaca-Pereira, VP Minkovich, and S Calixto. Fabrication and investigation of large-mode-area photonic crystal fibers. *Revista mexicana de física*, 59(4):317–321, 2013.

[6] Marcelo Vaca Pereira, Vladimir P Minkovich, R Espinosa-Luna, Yuri O Barmenkov, S Calixto, et al. Polarimetric parameters associated to special microstructured fibers. *Applied Optics*, 55(18):4865–4870, 2016.

[7] VP Minkovich, AB Sotsky, M Vaca Pereira, IS Dzen, and LI Sotskaya. Supercontinuum generation in a microstructured fiber with an irregular cladding. *Journal of Applied Spectroscopy*, 83(2):198–203, 2016.

[8] Marcelo Vaca Pereira Ghirghi, Vladimir P Minkovich, and Armando Garcia Villegas. Polymer optical fiber termination with use of liquid nitrogen. *Photonics Technology Letters, IEEE*, 26(5):516–519, 2014.

[9] Julia Skibina. Micro-and nanocapillary glass technology for optical biosensing.

[10] Kunimasa Saitoh and Masanori Koshiba. Empirical relations for simple design of photonic crystal fibers. *Optics express*, 13(1):267–274, 2005.

[11] Kunimasa Saitoh and Masanori Koshiba. Numerical modeling of photonic crystal fibers. *Lightwave Technology, Journal of*, 23(11):3580–3590, 2005.

[12] Eric Udd et al. *Fiber optic sensors*. Wiley Online Library, 1993.

[13] L Cognolato. Chemical vapour deposition for optical fibre technology. *Le Journal de Physique IV*, 5(C5):C5–975, 1995.

[14] Jeff Hecht. A short history of fiber optics. *Reproduction of" Fiber Optics Technician's Handbook" by J Hayes, Delmar Publishers, Albany, New York. Also excerpted from" City of Light: The Story of Fiber Optics", Oxford University Press, New York*, 1999.

[15] and others. Picture transmission, March 25 1930. US Patent 1,751,584.

[16] E Ralph and WL McCabe. Memorial tributes: National academy of engineering, 1984.

[17] Allan W Snyder and D John. Love, optical waveguide theory. *Chapman and Hall Ltd*, 13:592, 1983.

[18] D Gloge. Weakly guiding fibers. *Applied Optics*, 10(10):2252–2258, 1971.

[19] JC Knight, TA Birks, P St J Russell, and DM Atkin. All-silica single-mode optical fiber with photonic crystal cladding. *Optics letters*, 21(19):1547–1549, 1996.

[20] Brian J Mangan, Alistair C Muir, and Jonathan C Knight. Photonic bandgap fiber with multiple hollow cores. *Journal of Lightwave Technology*, 28(9):1287–1290, 2010.

[21] Sophie Brustlein, Pascal Berto, Richard Hostein, Patrick Ferrand, Cyrille Billaudeau, Didier Marguet, Alistair Muir, Jonathan Knight, and Hervé Rigneault. Double-clad hollow core photonic crystal fiber for coherent raman endoscope. *Optics express*, 19(13):12562–12568, 2011.

[22] Cristiano M Cordeiro, Eliane M dos Santos, C H Brito Cruz, and Christiano J de Matos. Side access to the holes of photonic crystal fibers-new sensing possibilities. In *Optical Fiber Sensors*, page ThE68. Optical Society of America, 2006.

[23] John C Travers, Wonkeun Chang, Johannes Nold, Nicolas Y Joly, and Philip St J Russell. Ultrafast nonlinear optics in gas-filled hollow-core photonic crystal fibers [invited]. *JOSA B*, 28(12):A11–A26, 2011.

[24] Alexandre Bozolan, Christiano JS de Matos, Cristiano MB Cordeiro, Eliane M Dos Santos, and John Travers. Supercontinuum generation in a water-core photonic crystal fiber. *Optics express*, 16(13):9671–9676, 2008.

[25] Fetah Benabid, J Knight, and PSTJ Russell. Particle levitation and guidance in hollow-core photonic crystal fiber. *Optics express*, 10(21):1195–1203, 2002.

[26] MK Garbos, TG Euser, and P St J Russell. Optofluidic immobility of particles trapped in liquid-filled hollow-core photonic crystal fiber. *Optics express*, 19(20):19643–19652, 2011.

[27] Boris T Kuhlmey, Ross C McPhedran, and C Martijn de Sterke. Modal cutoff in microstructured optical fibers. *Optics letters*, 27(19):1684–1686, 2002.

[28] Tim A Birks, Jonathan C Knight, and P St J Russell. Endlessly single-mode photonic crystal fiber. *Optics letters*, 22(13):961–963, 1997.

[29] JC Knight, TA Birks, RF Cregan, P St J Russell, and JP De Sandro. Large mode area photonic crystal fibre. *Electronics Letters*, 34(13):1347–1348, 1998.

[30] John M Dudley, Goëry Genty, and Stéphane Coen. Supercontinuum generation in photonic crystal fiber. *Reviews of modern physics*, 78(4):1135, 2006.

[31] Brian Mangan, Lance Farr, Allen Langford, P John Roberts, David P Williams, Francois Couny, Matthew Lawman, Matthew Mason, Sam Coupland, Randolf Flea, et al. Low loss (1.7 db/km) hollow core photonic bandgap fiber. In *Optical Fiber Communication Conference*, page PD24. Optical Society of America, 2004.

[32] F Couny, Fetah Benabid, and PS Light. Large-pitch kagome-structured hollow-core photonic crystal fiber. *Optics Letters*, 31(24):3574–3576, 2006.

[33] Francois Couny, Peter J Roberts, TA Birks, and F Benabid. Square-lattice large-pitch hollow-core photonic crystal fiber. *Optics express*, 16(25):20626–20636, 2008.

[34] Gordon A Thomas, Boris I Shraiman, Paul F Glodis, and Michael J Stephen. Towards the clarity limit in optical fibre. *Nature*, 404(6775):262–264, 2000.

[35] T Srensen, Jes Broeng, A Bjarklev, Erik Knudsen, and SE Barkou Libori. Macro-bending loss properties of photonic crystal fibre. *Electronics letters*, 37(5):1, 2001.

[36] SC Rashleigh and R Ulrich. Polarization mode dispersion in single-mode fibers. *Optics Letters*, 3(2):60–62, 1978.

[37] Govind P Agrawal. *Nonlinear fiber optics*. Academic press, 2007.

[38] LG Cohen, Chinlon Lin, and WG French. Tailoring zero chromatic dispersion into the 1.5–1.6 μm low-loss spectral region of single-mode fibres. *Electronics Letters*, 15(12):334–335, 1979.

[39] Jinendra K Ranka, Robert S Windeler, and Andrew J Stentz. Visible continuum generation in air–silica microstructure optical fibers with anomalous dispersion at 800 nm. *Optics letters*, 25(1):25–27, 2000.

[40] William Reeves, J Knight, P Russell, and P Roberts. Demonstration of ultra-flattened dispersion in photonic crystal fibers. *Optics express*, 10(14):609–613, 2002.

[41] William Wadsworth, Jonathan Knight, and Tim Birks. State-of-the-art photonic crystal fiber. *Optics and Photonics News*, 23(3):24–31, 2012.

[42] D Pysz, I Kujawa, R Stępień, M Klimczak, A Filipkowski, M Franczyk, L Kociszewski, J Buźniak, K Haraśny, and R Buczyński. Stack and draw fabrication of soft glass microstructured fiber optics. *Bulletin of the Polish Academy of Sciences Technical Sciences*, 62(4):667–682, 2014.

[43] Heike Ebendorff-Heidepriem and Tanya M Monro. Extrusion of complex preforms for microstructured optical fibers. *Optics Express*, 15(23):15086–15092, 2007.

[44] P. Russell. Photonic crystal fibers. *Science*, 299(5605):358–362, 2003.

[45] S.G. Johnson and J.D. Joannopoulos. Block–iterative frequency–domain methods for Maxwell's equations in a planewave basis. *Optics Express*, 8(3):173–190, 2001.

[46] T.P. White, B.T. Kuhlmey, R.C. McPhedran, D. Maystre, G. Renversez, C.M. De Sterke, and L.C. Botten. Multipole method for microstructured optical fibers. I. Formulation. *Journal of the Optical Society of America B*, 19(10):2322–2330, 2002.

[47] M. Koshiba. Full–vector analysis of photonic crystal fibers using the finite element method. *IEICE Trans. Electron.*, E85-C(4):881–888, 2002.

[48] K. Saitoh and M. Koshiba. Full–vectorial imaginary–distance beam propagation method based on a finite element scheme: Application to photonic crystal fibers. *IEEE Journal of Quantum Electronics*, 38(7):927–933, 2002.

[49] M. Koshiba and K. Saitoh. Applicability of classical optical fiber theories to holey fibers. *Optics Letters*, 29(15):1739–1741, 2004.

[50] M. Nielsen and N. Mortensen. Photonic crystal fiber design based on the V–parameter. *Optics Express*, 11(21):2762–2768, 2003.

[51] N.A. Mortensen, M.D. Nielsen, J.R. Folkenberg, A. Petersson, and H.R. Simonsen. Improved large–mode–area endlessly single–mode photonic crystal fibers. *Optics Letters*, 28(6):393–395, 2003.

[52] Boris Kuhlmey, Ross McPhedran, C de Sterke, Peter Robinson, Gilles Renversez, and Daniel Maystre. Microstructured optical fibers: where ?? s the edge? *Optics Express*, 10(22):1285–1290, 2002.

[53] Niels Asger Mortensen, Jacob Riis Folkenberg, Martin D Nielsen, and Kim P Hansen. Modal cutoff and the v parameter in photonic crystal fibers. *Optics letters*, 28(20):1879–1881, 2003.

[54] Kim P Hansen René E. Kristiansen. Microstructured fibers and their applications. *Óptica pura y aplicada*, 38(3):37–49, 2005.

[55] Takashi Matsui, Jian Zhou, Kazuhide Nakajima, and Izumi Sankawa. Dispersion-flattened photonic crystal fiber with large effective area and low confinement loss. *Lightwave Technology, Journal of*, 23(12):4178–4183, 2005.

[56] Nikolaos Florous, Kunimasa Saitoh, and Masanori Koshiba. The role of artificial defects for engineering large effective mode area, flat chromatic dispersion, and low leakage losses in photonic crystal fibers: Towards high speed reconfigurable transmission platforms. *Optics express*, 14(2):901–913, 2006.

[57] Kunimasa Saitoh, M Koshiba, T Hasegawa, and E Sasaoka. Chromatic dispersion control in photonic crystal fibers: application to ultra-flattened dispersion. *Optics Express*, 11(8):843–852, 2003.

[58] Joel Villatoro, Vladimir P Minkovich, and Joseba Zubia. Locally pressed photonic crystal fiber interferometer for multiparameter sensing. *Optics letters*, 39(9):2580–2583, 2014.

[59] NKTPhotonics lma-20. http://www.nktphotonics.com/wp-content/uploads/2015/01/LMA-20.pdf. Accessed: 2016-04-26.

[60] F Poli, A Cucinotta, S Selleri, and AH Bouk. Tailoring of flattened dispersion in highly nonlinear photonic crystal fibers. *Photonics Technology Letters, IEEE*, 16(4):1065–1067, 2004.

[61] A Barrientos-García, JA Andrade-Lucio, Igor A Sukhoivanov, Igor Guryev, J Ruiz-Pinales, and R Rojas-Laguna. Numerical study of photonic crystal fiber with ultra-flattened chromatic dispersion in anomalous and normal dispersion regimes. *Optik*, 126:1307–1311, 2015.

[62] Dalia D El-Mosalmy, MFO Hameed, Nihal FF Areed, and SSA Obayya. Novel neural network based optimization approach for photonic devices. *Optical and Quantum Electronics*, 46(3):439–453, 2014.

[63] Mohamed Farhat O Hameed, KR Mahmoud, and SSA Obayya. Metaheuristic algorithms for dispersion optimization of photonic crystal fibers. *Optical and Quantum Electronics*, 48(2):1–11, 2016.

[64] NKTPhotonics sc-5.0-1040. http://www.nktphotonics.com/wp-content/uploads/2015/03/SC-5.0-1040.pdf. Accessed: 2016-04-23.

[65] NKTPhotonics nl-1050-neg-1. http://www.nktphotonics.com/wp-content/uploads/2015/03/NL-1050-NEG-1.pdf. Accessed: 2016-04-23.

[66] Vladimir P Minkovich, Alexander V Kir'yanov, Alexander B Sotsky, and Ludmila I Sotskaya. Large-mode-area holey fibers with a few air channels in cladding: modeling and experimental investigation of the modal properties. *JOSA B*, 21(6):1161–1169, 2004.

[67] TP White, RC McPhedran, C Martijn de Sterke, LC Botten, and MJ Steel. Confinement losses in microstructured optical fibers. *Optics Letters*, 26(21):1660–1662, 2001.

[68] Govind P Agrawal. Nonlinear fiber optics. *the Institute of Optics, University of Rochester, Optics and Photonics, Acadcmic Press, ISBN: 012045143-3*, 1995.

[69] Anders Bjarklev, Jes Broeng, and Araceli Sanchez Bjarklev. *Photonic crystal fibres*. Springer Science & Business Media, 2012.

[70] J Limpert, O Schmidt, J Rothhardt, F Röser, T Schreiber, A Tünnermann, S Ermeneux, P Yvernault, and F Salin. Extended single-mode photonic crystal fiber lasers. *Optics Express*, 14(7):2715–2720, 2006.

[71] John M Dudley and James Roy Taylor. *Supercontinuum generation in optical fibers*. Cambridge University Press, 2010.

[72] Federica Poli, Annamaria Cucinotta, and Stefano Selleri. *Photonic crystal fibers: properties and applications*, volume 102. Springer Science & Business Media, 2007.

[73] Osamu Tohyama and Syun-Ichiro Yamaguchi. Photonic crystal fibers and their applications. *IEEJ Transactions on Electrical and Electronic Engineering*, 4(6):704–709, 2009.

[74] Edward Collett. Polarized light. fundamentals and applications. *Optical Engineering, New York: Dekker,/ c1992*, 1, 1992.

[75] P Olivard, PY Gerligand, B Le Jeune, J Cariou, and J Lotrian. Measurement of optical fibre parameters using an optical polarimeter and stokes-mueller formalism. *Journal of Physics D: Applied Physics*, 32(14):1618, 1999.

[76] Tinko A Eftimov, Wojtek J Bock, Predrag Mikulic, and Jiahua Chen. Müller–stokes analysis of long period gratings part ii: Randomly birefringent lpgs. *Lightwave Technology, Journal of*, 27(17):3759–3764, 2009.

[77] Karla M Salas-Alcántara, R Espinosa-Luna, I Torres-Gómez, and Yuri O Barmenkov. Determination of the mueller matrix of uv-inscribed long-period fiber grating. *Applied optics*, 53(2):269–277, 2014.

[78] José Jorge Gil and Eusebio Bernabeu. A depolarization criterion in mueller matrices. *Journal of Modern Optics*, 32(3):259–261, 1985.

[79] José Jorge Gil and Eusebio Bernabeu. Depolarization and polarization indices of an optical system. *Journal of Modern Optics*, 33(2):185–189, 1986.

[80] Russell A Chipman. Depolarization index and the average degree of polarization. *Applied optics*, 44(13):2490–2495, 2005.

[81] Rafael Espinosa-Luna and Eusebio Bernabeu. On the q (m) depolarization metric. *Optics communications*, 277(2):256–258, 2007.

[82] Christian Brosseau. *Fundamentals of polarized light: a statistical optics approach*. Wiley-Interscience, 1998.

[83] Shih-Yau Lu and Russell A Chipman. Mueller matrices and the degree of polarization. *Optics communications*, 146(1):11–14, 1998.

[84] P Roberts, F Couny, H Sabert, B Mangan, T Birks, J Knight, and P Russell. Loss in solid-core photonic crystal fibers due to interface roughness scattering. *Optics express*, 13(20):7779–7793, 2005.

[85] Michael R Hutsel, Reeve Ingle, and Thomas K Gaylord. Accurate cross-sectional stress profiling of optical fibers. *Applied optics*, 48(26):4985–4995, 2009.

[86] Philip St J Russell. Photonic-crystal fibers. *Journal of lightwave technology*, 24(12):4729–4749, 2006.

[87] MJ Gander, R McBride, JDC Jones, D Mogilevtsev, TA Birks, JC Knight, and P St J Russell. Experimental measurement of group velocity dispersion in photonic crystal fibre. *Electronics Letters*, 35(1):63–64, 1999.

[88] JC Knight, J Arriaga, TA Birks, A Ortigosa-Blanch, WJ Wadsworth, and P St J Russell. Anomalous dispersion in photonic crystal fiber. *Photonics Technology Letters, IEEE*, 12(7):807–809, 2000.

[89] Zbyszek Holdynski, Marek Napierala, Pawel Mergo, and Tomasz Nasilowski. Experimental investigation of supercontinuum generation in photonic crystal fibers pumped with sub-ns pulses. *Journal of Lightwave Technology*, 33(10):2106–2110, 2015.

[90] Karen Marie Hilligsøe, Thomas Andersen, Henrik Paulsen, Carsten Nielsen, Klaus Mølmer, Søren Keiding, Rene Kristiansen, Kim Hansen, and Jakob Larsen. Supercontinuum generation in a photonic

crystal fiber with two zero dispersion wavelengths. *Optics Express*, 12(6):1045–1054, 2004.

[91] A Kudlinski, SF Wang, A Mussot, and M Conforti. Soliton annihilation into a polychromatic dispersive wave. *Optics letters*, 40(9):2142–2145, 2015.

[92] MLV Tse, P Horak, JHV Price, F Poletti, F He, and DJ Richardson. Pulse compression at 1.06 μm in dispersion-decreasing holey fibers. *Optics letters*, 31(23):3504–3506, 2006.

[93] JC Travers, James M Stone, AB Rulkov, BA Cumberland, AK George, SV Popov, JC Knight, and JR Taylor. Optical pulse compression in dispersion decreasing photonic crystal fiber. *Optics express*, 15(20):13203–13211, 2007.

[94] K Hansen. Dispersion flattened hybrid-core nonlinear photonic crystal fiber. *Optics Express*, 11(13):1503–1509, 2003.

[95] Ming-Leung V Tse, Peter Horak, Francesco Poletti, Neil GR Broderick, Jonathan HV Price, John R Hayes, and David J Richardson. Supercontinuum generation at 1.06 μm in holey fibers with dispersion flattened profiles. *Optics Express*, 14(10):4445–4451, 2006.

[96] A Ferrando, E Silvestre, JJ Miret, and P Andres. Nearly zero ultraflattened dispersion in photonic crystal fibers. *Optics Letters*, 25(11):790–792, 2000.

[97] Kunimasa Saitoh, Nikolaos Florous, and Masanori Koshiba. Ultraflattened chromatic dispersion controllability using a defected-core photonic crystal fiber with low confinement losses. *Optics Express*, 13(21):8365–8371, 2005.

[98] Alexander Hartung, Alexander M Heidt, and Hartmut Bartelt. Design of all-normal dispersion microstructured optical fibers for pulse-preserving supercontinuum generation. *Optics express*, 19(8):7742–7749, 2011.

[99] Sotskiĭ. Leaky modes in optical fibers with transverse anisotropy.

[100] Boris T Kuhlmey, Thomas P White, Gilles Renversez, Daniel Maystre, Lindsay C Botten, C Martijn de Sterke, and Ross C McPhedran. Multipole method for microstructured optical fibers. ii. implementation and results. *JOSA B*, 19(10):2331–2340, 2002.

[101] JC Knight and WJ Wadsworth. Silica fibres for supercontinuum generation. *Supercontinuum Generation in Optical Fibers*, page 62, 2010.

[102] P Petropoulos, TM Monro, W Belardi, K Furusawa, JH Lee, and DJ Richardson. 2r-regenerative all-optical switch based on a highly nonlinear holey fiber. *Optics Letters*, 26(16):1233–1235, 2001.

[103] AB Sotsky, OA Belskaya, and LI Sotskaya. Higher-order modes of photonic-crystal fibers. *Optics and Spectroscopy*, 110(3):432–437, 2011.

[104] AV Husakou and J Herrmann. Supercontinuum generation of higher-order solitons by fission in photonic crystal fibers. *Physical Review Letters*, 87(20):203901, 2001.

[105] Jennifer H Lee, James Van Howe, Chris Xu, Siddharth Ramachandran, Samir Ghalmi, and Man F Yan. Generation of femtosecond pulses at 1350 nm by čerenkov radiation in higher-order-mode fiber. *Optics letters*, 32(9):1053–1055, 2007.

[106] Olaf Ziemann, J"urgen Krauser, Peter E Zamzow, and Werner Daum. Passive components for optical fibers. *POF Handbook: Optical Short Range Transmission Systems*, pages 233–293, 2008.

[107] Mark G Kuzyk. *Polymer Fiber Optics: materials, physics, and applications*. CRC press, 2006.

[108] Markus Rothmaier, Bńrbel Selm, Sonja Spichtig, Daniel Haensse, and Martin Wolf. Photonic textiles for pulse oximetry. *Optics express*, 16(17):12973–12986, 2008.

[109] Xiao Lin, Liyong Ren, and Jian Liang. Nondestructive scheme for measuring the attenuation coefficient of polymer optical fiber. *Optics letters*, 38(4):528–530, 2013.

[110] Geoff Barton, Martijn A van Eijkelenborg, Geoffrey Henry, Maryanne CJ Large, and Joseph Zagari. Fabrication of microstructured polymer optical fibres. *Optical Fiber Technology*, 10(4):325–335, 2004.

[111] Martijn A van Eijkelenborg, Maryanne CJ Large, Alexander Argyros, Joseph Zagari, Steven Manos, Nader A Issa, Ian Bassett, Simon Fleming, Ross C McPhedran, C Martijn de Sterke, et al. Microstructured polymer optical fibre. *Optics express*, 9(7):319–327, 2001.

[112] Alexander Argyros, Ian Bassett, Martijn van Eijkelenborg, Maryanne Large, Joseph Zagari, Nicolae A Nicorovici, Ross McPhedran, and C Martijn de Sterke. Ring structures in microstructured polymer optical fibres. *Optics Express*, 9(13):813–820, 2001.

[113] JH Park, BG Shin, and JJ Kim. Fabrication of plastic holey fibers. In *Proceedings of the International Plastic Optical Fibres conference*, volume 11, pages 9–11, 2002.

[114] Yani Zhang, Kang Li, Lili Wang, Liyong Ren, Wei Zhao, Runcai Miao, Maryanne CJ Large, and Martijn A Van Eijkelenborg. Casting preforms for microstructured polymer optical fibre fabrication. *Optics express*, 14(12):5541–5547, 2006.

[115] Heike Ebendorff-Heidepriem, Tanya M Monro, Martijn A van Eijkelenborg, and Maryanne CJ Large. Extruded high-na microstructured polymer optical fibre. *Optics communications*, 273(1):133–137, 2007.

[116] Yan Gao, Ning Guo, Bertrand Gauvreau, Mahmoud Rajabian, Olga Skorobogata, Elio Pone, Oleg Zabeida, Ludvik Martinu, Charles Dubois, and Maksim Skorobogatiy. Consecutive solvent evaporation and co-rolling techniques for polymer multilayer hollow fiber preform fabrication. *Journal of materials research*, 21(09):2246–2254, 2006.

[117] SC Xue, RI Tanner, GW Barton, R Lwin, MCJ Large, and L Poladian. Fabrication of microstructured optical fibers-part i: Problem formulation and numerical modeling of transient draw process. *Journal of Lightwave Technology*, 23(7):2245, 2005.

[118] SC Xue, MCJ Large, GW Barton, RI Tanner, L Poladian, and R Lwin. Role of material properties and drawing conditions in the fabrication of microstructured optical fibers. *Journal of lightwave technology*, 24(2):853, 2006.

[119] S-C Xue, L Poladian, GW Barton, and MCJ Large. Radiative heat transfer in preforms for microstructured optical fibres. *International Journal of Heat and Mass Transfer*, 50(7):1569–1576, 2007.

[120] S-C Xue, R Lwin, GW Barton, L Poladian, and MCJ Large. Transient heating of pmma preforms for microstructured optical fibers. *Lightwave Technology, Journal of*, 25(5):1177–1183, 2007.

[121] Ajoy Ghatak and K Thyagarajan. *An introduction to fiber optics*. Cambridge university press, 1998.

[122] SH Law, JD Harvey, RJ Kruhlak, M Song, E Wu, GW Barton, MA Van Eijkelenborg, and MCJ Large. Cleaving of microstructured polymer optical fibres. *Optics Communications*, 258(2):193–202, 2006.

[123] Susan H Law, Martijn A van Eijkelenborg, Geoffrey W Barton, Cheng Yan, Richard Lwin, and J Gan. Cleaved end-face quality of microstructured polymer optical fibres. *Optics communications*, 265(2):513–520, 2006.

[124] Alessio Stefani, Kristian Nielsen, Henrik K Rasmussen, and Ole Bang. Cleaving of topas and pmma microstructured polymer optical fibers: Core-shift and statistical quality optimization. *Optics Communications*, 285(7):1825–1833, 2012.

[125] D Gloge, Peter W Smith, DL Bisbee, and Edwin L Chinnock. Optical fiber end preparation for low-loss splices. *Bell System Technical Journal*, 52(9):1579–1588, 1973.

[126] Giok-Djan Khoe, G Kuyt, and JA Luijendijk. Optical fiber end preparation: a new method for producing perpendicular fractures in glass fibers, coated-glass fibers, and plastic-clad fibers. *Applied optics*, 20(4):707–714, 1981.

Publications

1. M. Vaca-Pereira, Vladimir P. Minkovich, S. Calixto. "Fabrication and investigation of large-mode area photonic crystal fibers" Revista Mexicana de Fisica 07/2013, 59(4): 317-321. Impact factor: 0.35
2. M.V.P.Ghirghi, V.P. Minkovich, A.G. Villegas. "Polymer Optical Fiber Termination With Use of Liquid Nitrogen", IEEE Photonics Technology Letters 01/2014, 26(5): 516-519. Impact factor 2.04.
3. Marcelo Vaca Pereira G., Vladimir P. Minkovich, R. Espinosa-Luna, Yuri O. Barmenkov, and S. Calixto. "Polarimetric parameters associated to special microstructured fibers", Accepted for Applied Optics, 2016. Impact factor: 1.784.
4. V.P. Minkovich, A.B. Sotsky, M. Vaca Pereira G., I.S. Dzen and L.I. Sotskaya. "Supercontinuum generation in the microstructured fiber with an irregular cladding", Journal of Applied Spectroscopy, 03/2016, 83(2):295-15. Impact factor: 0.476.
5. Vladimir P. Minkovich, Marcelo Vaca Pereira G., Joel Villatoro, Evgeny Myslivets, Alexander B. Sotsky, Ivan S. Dzen, María Asunción Illarramendi, Joseba Zubia."Supercontinuum Generation in Special Microstructured Fibers With Irregular and Regular Claddings Using Pumping Wavelengths in a Broad Range", accepted in IEEE Journal of Lightwave Technology, 2016. Impact factor: 2.965.

Congress Participation

1. Marcelo Vaca Pereira Ghirghi, Vladimir P. Minkovich. IONS NA-6 Ensenada (Baja California), Mexico 2013. September 2-4, 2013. Design and Fabrication of Photonic Crystal Fibers,
2. Marcelo Vaca Pereira Ghirghi, Vladimir P. Minkovich. Mexican Optics and Photonics Meeting, Ensenada, B.C., September 4-6, 2013. Design and Fabrication of Photonic Crystal Fibers,
3. Marcelo Vaca Pereira Ghirghi, Vladimir Petrovich Minkovich. IONS NA-8 Montreal, Canada, May 25-27, 2014. Polymer Optical Fiber End Preparation with Use of Liquid Nitrogen,
4. Marcelo Vaca Pereira Ghirghi, Vladimir Petrovich Minkovich. Photonic North, Montreal, Canada. Palacio de los congresos, May 28-30, 2014. Polymer Optical Fiber End Preparation with Use of Liquid Nitrogen.

Groups of collaboration

1. Centro de Investigacion y desarrollo CARSO (CIDEC), Querétaro (México)
2. Escuela Tecnica Superior de Ingenieria de Bilbao, Universidad del Pais Vasco (UPV), campus San Mames y Leioa, Bilbao (Spain)
3. Mogilev State University, Physics Departments, Mogilev (Belarus)
4. Photonics System Group, University of California, San Diego (USA)

Vita

I, Marcelo Vaca Pereira Ghirghi, was born in Santa Cruz de la Sierra, Bolivia, in 1983. In 1989, my family and I moved to Brazil, to live there for 3 years. After that, we went back to Santa Cruz, where I finished primary and middle school. In 2000, I was admitted to the Gabriel René Moreno University in Santa Cruz de la Sierra, and began to study electromechanical engineering, but in 2003, I got a chance to go to study in Russia; I did a preparation course on Russian for 1 year in the city of Belgorod (within the Russian Federation), and after that, I went to Moscow to study at the Moscow State University of Geodesy and Cartography, where I earned an Engineering Degree in Optics and optical electronic devices and systems in 2009; I defended my thesis in 2010, on the topic of LIDAR measurement of air velocity in an airport. In 2010, I joined the Centro de Investigaciones en Óptica (CIO) as a graduate student, earning my Masters Degree in August 2012; under the counselling of Dr. Uladzímir Petrovich Minkovich, I wrote a thesis on the topic of design and fabrication of large mode area photonic crystal fibers.

Since September 2012, I have been working towards earning my Ph. D. at CIO, continuing my work with Dr. Uladzímir Minkovich in the field of design and fabrication of photonic crystal fibers. This thesis represents the culmination of my work towards the Doctoral Degree.